DISS. ETH NO. 29000

HVDC Overhead Line Corona Characteristics: A Modern Toolbox and Geographic Specificities

A thesis submitted to attain the degree of

Doctor of Sciences
(Dr. sc. ETH Zürich)

presented by

Pascal Toma BLEULER

MSc (ing. él. dipl.), EPFL
born on 20 December 1991
citizen of Zollikon, ZH

accepted on the recommendation of

Prof. Dr. Christian Michael FRANCK	examiner
Prof. Dr. Tiebing LU	co-examiner

2023

Set in Robert Slimbach's 10 pt Adobe Utopia Regular
Typeset using LaTeX 2ε and related tools based on Donald Knuth's TeX

Acknowledgements

First and foremost, I would like to express my deepest gratitude to Prof. Christian Franck for his academic supervision, personal mentoring and the working environment he is nurturing at ETH Zürich's High Voltage Laboratory. He made me truly appreciate the German word *Doktorvater* / *Doktormutter*, and I am proud to be able to call him that.

This work was supported by the German TSO TransnetBW, not only financially, but especially through our collaboration with Wolfgang Tausend, Christian Eberhardt, Anna Lusiewicz, Markus Jäckle and all of their team. Many thanks to them for sharing their valuable expertise with us, and for being such a supportive industry partner.

I am grateful to Prof. Tiebing Lu from the North China Electric Power University for accepting to be the co-examiner of this thesis and for his insightful feedback. I would also like to thank Ass. Prof. Oliver Pischler from the TU Graz for being the second advisor of my doctoral studies, for all the technical discussions, the work we have achieved together and even more so for the friendship we have developed over the years.

None of this work would have happened had Prof. Philipp Rudolf von Rohr, Christos Stamatopoulos and Martin Pfeiffer not been looking for someone to work with them on their "levitating water droplets" project. I thank for this opportunity.

I would like to thank my most direct “overhead line colleagues” and friends, Sören Hedtke and Hannah Kirchner for the hours spent together as a team. This core crew of course extends to a broader “overhead line group and office” that includes Pengfei Xu, Pascal Devaud, Bo Chen, Tommaso Polonelli, Yang Lu and Yu Xiao.

Many thanks in fact to the entire High Voltage Laboratory for the supportive, open and comradely work environment. For teaching me so much and for their kindness I would especially like to mention Hans-Jürg Weber and Fabian Mächler, along with his apprentices, Kamil Halvdan Dwinger, Simon Hauri, Simon Ramchandani, and Damian Sonderegger. Also particularly valuable were the administrative and technical support of Karin Sonderegger Zaky, Philipp Simka, Edoardo Talotti and Marina Eisenstat.

I am indebted to the excellent students who helped along with this work, Johanna Vorwerk, Isabelle Schlatter, Fabian Ulmer, Jaime Lopez Raichs, Sergio Meyer, Benjamin Stadler, and Lorenz Gallina.

The outdoor setup in Däniken only existed thanks to the patronage of the FKH. I am grateful to Reinhold Bräunlich, Michael Walter, Mario Gobeli, Toni von Deschwanden, Markus von Arx, Simon Mutter, Tobias Felber and the whole team for their interest, engagement and understanding.

I had the chance to repeatedly meet great minds of the field and very much enjoyed working with Saskia Möllenbeck and Benjamin Schröder from Amprion, Joshu Jullier from Swissgrid, Prof. Uwe Schichler and Lukas Schwalt from the TU Graz and many others.

Among my best memories at ETH Zürich will certainly be the time I spent representing the scientific staff as part of AVETH within the University Assembly. Being in the committee with such people as Prof. Werner Wegscheider, Prof. Dagmar Iber, Adrian Gilli, Viktoria Gerken, Tobias Neef, Corentin Pfister, Luca Dahle, Nils Jensen, Emir İşman, Stefan Karlen, Christopher Sauder Engeler, or Kristin Becker van Slooten was truly an honor. I also wish to salute the fruitful exchanges we have had with our school President Prof. Joël Mesot,

our Rectors Prof. Sarah Springman and Prof. Günther Dissertori, and the entire school board as well as with Prof. Michael Hengartner and the entire ETH Board.

I of course want to thank all the friends who have been by my side throughout my entire academic life and who made it so much more enjoyable than it otherwise would have been. Finally, with all the love there is in the world, I thank my family. My parents, thanks to whom so much felt so evident and effortless, my dear sister for being such a badass and Aurélie for being everything to me.

Contents

Abstract

The energy transition that needs to happen in the face of the climate crisis requires electric transmission grids to have a higher capacity to absorb power flows. An important technical limitation in this regard are corona effects around overhead lines.

This thesis presents tools and methods to assess the long-term corona characteristics of HVDC overhead line corona.

Advances in material sciences allow to study the fundamental interactions of water droplets in electric fields on different surfaces. These interactions and the way they can lead to partial discharges are explained using experimental results as well as predictive simulations models and metrics are given to characterize the corona performance of surfaces.

Based on modern IoT technologies, a unified sensor platform is presented that can measure different heterogeneous corona quantities while being efficient in terms of both energy and cost. The platform's capabilities and usefulness are demonstrated with experiments on test lines. Novel visualization techniques for partial discharge measurements are introduced as well. These methods are all required to enable meaningful long-term measurement of overhead line corona.

Long-term results of an outdoor HVDC test line in the Swiss urban environment are presented. On their basis, trends are identified while still showing the variability in long-term corona data.

It is discussed to what extent corona effects are specific to climates and environments and what the important metrics are in this respect. The unified IoT sensor platform is specifically introduced to make it easier to deploy a large quantity of corona measurement devices and thus monitor corona performance of overhead lines over entire territories traversed by transmission lines.

Kurzfassung

Die Energiewende, die angesichts der Klimakrise vollzogen werden muss, erfordert, dass die Stromübertragungsnetze eine höhere Kapazität zur Aufnahme von Energieflüssen haben. Eine wichtige technische Einschränkung in diesem Zusammenhang sind Koronaeffekte um Freileitungen.

In dieser Arbeit werden Instrumente und Methoden zur Bewertung der langfristigen Koronaeigenschaften von HGÜ-Freileitungskorona vorgestellt.

Fortschritte in den Materialwissenschaften ermöglichen es, die grundlegenden Interaktionen von Wassertropfen in elektrischen Feldern auf verschiedenen Oberflächen zu untersuchen. Diese Interaktionen und die Art und Weise, wie sie zu Teilentladungen führen können, werden anhand von experimentellen Ergebnissen sowie prädiktiven Simulationsmodellen erläutert und Metriken zur Charakterisierung der Korona Performance von Oberflächen angegeben.

Basierend auf modernen IoT-Technologien wird eine einheitliche Sensorplattform vorgestellt, die verschiedene heterogene Koronagrössen messen kann und dabei sowohl energie- als auch kosteneffizient ist. Die Fähigkeiten und die Nützlichkeit der Plattform werden mit Experimenten an Testleitungen demonstriert. Ausserdem werden neuartige Visualisierungsmethoden für Teilentladungsmessungen vorgestellt. All diese Ergebnisse sind erforderlich, um aussagekräftige

Langzeitmessungen von Korona bei Freileitungen zu ermöglichen.

Es werden Langzeitergebnisse einer HGÜ-Freileitung im Schweizerischen städtischen Umfeld vorgestellt. Darauf aufbauend werden Trends erkennt und gleichzeitig die Variabilität von Langzeit-Koronadaten gezeigt.

Es wird diskutiert, inwieweit Koronaeffekte klima- und umgebungsspezifisch sind und welches die wichtigen Metriken in diesem Zusammenhang sind. Die einheitliche IoT-Sensorplattform wird speziell eingeführt, um den Einsatz einer grossen Anzahl von Koronamessgeräten zu erleichtern und so die Korona Performance von Freileitungen in ganzen Gebieten, die von Übertragungsleitungen durchquert werden, zu überwachen.

Author's Publications and Contributions

First author journal publications

C. Stamatopoulos, P. Bleuler, M. Pfeiffer, S. Hedtke, P. R. von Rohr, and C. M. Franck (Apr. 2019). "Influence of Surface Wettability on Discharges from Water Drops in Electric Fields". In: *Langmuir* 35 (14), pp. 4876–4885. DOI: 10.1021/acs.langmuir.9b00374

> C.S., P.B., and M.P. contributed equally to this work ("first authorship with equal contribution"). C.S. and M.P. conceived the idea to perform this research. C.M.F., P.RvR., C.S., M.P., and S.H. guided the research scientifically and technically. P.B., C.S., and M.P. executed experiments and analysed data. M.P. and P.B. performed simulations. C.S. fabricated test surfaces. C.S., P.B., M.P., C.M.F., and P.RvR. wrote the paper.
> Content from this publication serves as a basis for section 6.1 and chapter 9.

P. Bleuler, Y. Xiao, T. Polonelli, B. Stadler, L. Gallina, H. Kirchner, M. Magno, and C. M. Franck (submitted). "A Unified Sensor Platform for Investigating Corona Effects on Overhead Lines". In: *IEEE Transactions on Instrumentation and Measurement*

P.B., T.P., M.M. and C.M.F. guided the research scientifically and technically. P.B. Conceived the idea of the project, designed the experiments. P.B., T.P., B.S. and L.G. Designed the sensor circuitry. P.B., X.Y., T.P., B.S. and L.G. designed and implemented the software solutions. P.B., X.Y., T.P., B.S., L.G. and H.K. performed measurements and analysed results. All authors wrote the paper.
Content from this publication serves as a basis for part III and chapters 11 and 12.

P. Bleuler and C. M. Franck (in preparation). "Rain Event and Metric Dependency of Wet Weather Corona in HVDC Overhead Lines". In: *IEEE Transactions on Power Delivery*

P.B. designed and conducted the experiment and analysed the result. C.M.F. guided the research. All authors wrote the paper.
Content from this publication serves as a basis for part V.

First author conference publications

P. Bleuler, S. Hedtke, and C. M. Franck (2020). "Corona Performance of DC Overhead Lines in Outdoor Experiments During Wet Weather Transitions and under Varying Humidity". In: *CIGRE Session, Paris*

P.B. conducted the experiment and analysed the result. C.M.F. and S.H. guided the research. All authors wrote the paper.
Content from this publication serves as a basis for chapter 10.

Other co-authored publications on related topics

For these publications, P.B. has contributed in various forms, but none of the results presented in them are directly part of this thesis.

S. Hedtke, P. Bleuler, and C. M. Franck (Dec. 2021). "Outdoor Investigation of the Corona Characteristics and Audible Noise of a Hybrid AC/DC Overhead Line". In: *IEEE Transactions on Power Delivery* 36 (6), pp. 3309–3317. DOI: 10.1109/TPWRD.2020.3038414

S. Hedtke, M. Pfeiffer, M. Gobeli, P. Bleuler, R. Bräunlich, and C. M. Franck (2018). "Setup of an Outdoor Hybrid AC / DC Test Line for Corona Measurements". In: *VDE-Hochspannungstechnik, ETG-Fachberichte*

O. Pischler, S. Hedtke, P. Bleuler, U. Schichler, and C. M. Franck (2019). "Corona Effects of Overhead Lines under Mixed AC/DC Stresses". In: *CIGRE Symposium Chengdu*

C. M. Franck, C.-C. Hsu, Y. Xiao, P. Bleuler, G. Frusque, M. Muratovic, and T. Polonelli (2023). "Intelligent Maintenance of T&D Equipment". In: *IEEE Power & Energy Magazine* 21.2, pp. 18–29. DOI: 10.1109/MPE.2022.3230968

Y. Xiao, P. Bleuler, and C. M. Franck (in preparation). "An IoT-based Digital Osciloscope for MCCB Predictive Maintenance". In: *IEEE Transactions on Instrumentation and Measurement*

B. Chen, P. Bleuler, H. Kirchner, C. M. Franck, and T. Lu (in preparation). "The Influence of Dielectric Film with Different Resistivities on the Ion Flow Field Under HVDC Overhead Lines". In: *IEEE Transactions on Dielectrics and Electrical Insulation*

Relevant student theses

Many students collaborated with the author on various aspects of this project in the context of student theses. While not all of them are directly cited in the text that follows, their contributions were nonetheless important.

J. Vorwerk (2018). "Effect of Electric Field on Droplets Impacting Surfaces with Different Wettabilities". Master's Thesis. ETH Zürich

I. Schlatter (2020). "Artificial Corona Sources for a 400 kV Outdoor Test Line". Semester Project. ETH Zürich

F. Ulmer (2021). "Smart Sensors for Monitoring the Electric Power Network". Semester Project. ETH Zürich

J. Lopez Raichs (2021). “Measurement Campaign on a 400 kV Outdoor Hybrid AC/DC Test Line”. Semester Project. ETH Zürich

S. Meyer (2021). “Smart Sensors for Monitoring the Electric Power Network”. Bachelor’s Thesis. ETH Zürich

B. Stadler (2021). “Ground Level Ion Current Density Smart Sensor for use under HVDC Test Lines”. Bachelor’s Thesis. ETH Zürich

L. Gallina (2022a). “A Practical Smart Sensor Used for the Long-Term Monitoring of Corona Currents on Overhead Lines”. Master’s Thesis. ETH Zürich

L. Gallina (2022b). “Optimizations and Applications of an IoT Smart Sensor to Monitor Corona Currents on Overhead Lines”. Semester Project. ETH Zürich

Part I

Introduction

I want you to panic. I want you to feel the fear I feel every day. And then I want you to act. I want you to act as you would in a crisis. I want you to act as if our house is on fire. Because it is.

— Greta Thunberg
During the World Economic Forum, Davos, 2019

Chapter 1

Motivations for Corona Research

1.1 A world in crisis

The latest report from the Intergovernmental Panel on Climate Change (IPCC) clearly demonstrates how climate change is already destroying entire ecosystems, reducing food and water security, adversely affecting physical and mental health of people, and contributing to humanitarian crises (IPCC 2022). The scenarios outlined for the future of planet Earth are extremely bleak (IPCC 2021). Based on that, it can be said without exaggeration that the energy transition encapsulates many of the massive and immediate changes needed to quite literally save the world.

Two important components of the energy transition are an increased electrification of energy intensive human activity as well as an increased share of renewable electricity sources powering the world's energy grids. These two unavoidable evolutions bring with them the need for more capacity in electricity transmission grids.

1.2 A need for increased grid capacity

Two of the most important renewable energy sources are wind and solar and their capital (Egli, Steffen, and Schmidt 2018) and operating (Steffen et al. 2020) costs are decreasing dramatically. Research has highlighted how going from a radial scheme where large power plants produce a predictable amount of energy to one where distributed power plants produce intermittent renewable power requires more flexibility in the grid (Allard et al. 2020). By taking advantage of climatic diversity across large regions, such as the European continent (Grams et al. 2017), the variability in intermittent power output can be somewhat compensated at the cost of increased power exchanges.

The technical and economic consequences (Schlecht and Weigt 2015) of lacking capacity on transmission grids are even being recognized by global management consulting firms (Christakou et al. 2022).

1.3 Corona effects as a limiting factor

Increasing grid capacity implies either the construction of new transmission lines or the uprating of existing ones. In both cases, when those lines are overhead lines and not underground cables, a major design parameter will be a series of phenomena known as overhead line corona (CIGRE SC B2 2017; Maruvada 2000).

Moreover, to ensure public acceptance (Hedtke, Pfeiffer, Franck, Dermont, et al. 2018) and comply to local regulations (Engelen et al. 2012), audible noise emissions caused by corona discharges have become a topic of increasing interest in recent years.

I boarded the king's ship; now on the beak,
Now in the waist, the deck, in every cabin,
I flamed amazement: sometime I'ld divide,
And burn in many places; on the topmast,
The yards and bowsprit, would I flame distinctly,
Then meet and join.

— Shakespeare
The Tempest, Act I, Scene II
Ariel, an airy Spirit, appearing to sailors as St Elmo's fire

Chapter 2

Background

2.1 Corona discharges

From the point of view of the high voltage engineer, everything is fundamentally either an electrode or an insulator, and it is their task to ensure that the insulation between electrodes is sufficient for the correct operation of a given system. More specifically, the electric strength of insulating materials shall be enough to withstand the electric field stresses between electrodes in order to avoid unwanted electric discharges.

When an electric discharge does not bridge the full gap between two electrodes, it is called a partial discharge. Corona or corona discharges are partial discharges that occur between electrodes forming a strongly non-uniform electric field within a gas (IEC 2000; Meek and Craggs 1978).

The term *corona*, which means *crown* in Latin, is often thought to have originated from sailors observing a phenomena better known as *St Elmo's fire* in which the tip of a sailing ship's mast glows due to discharges caused by the atmospheric electric field during thunderstorms and can appear like a crown (Chang, Lawless, and Yamamoto

1991; Law and Dowling 2021).

Discharge phenomena are the result of complex processes of which two broad kinds are particularly relevant here, ionization by electron impact, and electron attachment.

If a free electron e^- accelerated in an electric field $\vec{E}$ collides with a neutral atom A with enough energy to knock out one of the atom's outer electrons, ionization occurs and results in a positive ion A^+ and an additional electron:

$$A + e^- \longrightarrow A^+ + 2e^-$$

A succession of such collision events will result in an exponentially growing number of free electrons called a Townsend avalanche (Townsend 1915).

The ionization coefficient α quantifies how probable it is for such a collision to happen for one electron travelling over a given distance along an electric field line.

On the other hand, some neutral atoms or molecules, for instance those that constitute a so-called electron-attaching gas, such as oxygen in atmospheric air, can also capture free electrons and form a negative ion through electron attachment:

$$A + e^- \longrightarrow A^-$$

The probability for free electrons to be lost to form negative ions in this way, over a given distance along an electric field line, is quantified by the attachment coefficient η.

The coefficients α and η are both characteristics of a gas, and are dependent on the number density of neutral particles (related to pressure and temperature through the ideal gas law $\frac{n}{V} = \frac{P}{RT}$) and the elec-

tric field strength $E = \|\vec{E}\|$. Both coefficients have the dimension of length^{-1}.

The difference $\alpha_{\text{eff}} = \alpha - \eta$ is called the effective ionization coefficient. Only in regions where $\alpha_{\text{eff}} > 0$, would an electron avalanche grow yielding a number of free electrons N_{e} over a distance x from an initial number of free electrons N_0 according to:

$$N_{\text{e}} = N_0 e^{\alpha_{\text{eff}} x} \tag{2.1}$$

Meanwhile, where $\alpha_{\text{eff}} \leq 0$, the number of electron either decreases or remains constant.

This in turn, allows to define the critical electric field strength E_{crit} as the field strength in specific gas conditions such that $\alpha_{\text{eff}}(E_{\text{crit}}) \stackrel{!}{=} 0$. For dry atmospheric air at standard temperature and pressure $E_{\text{crit, air}}$ is generally accepted to be around 24 kV/cm.

The large difference in mass between ions and free electrons generated in the processes just described means that discharge phenomena will be different depending on the polarity of the electrode around which they originate.

2.2 Electric field and non-uniformities around overhead line conductors

An idealized overhead line can be seen as two electrodes — a cylinder to which a high voltage is applied above a grounded plane — with some gas, namely air, between them. Since the cylinder radius is small compared to its height above the plane, around the cylinder surface, field lines will be purely radial as illustrated in figure 2.1. On any of those field lines the field strength is highest at the cylinder surface and decays rapidly.

If the electric field strength at the conductor surface is high enough, there will be a small region around the line where $\alpha_{\text{eff}} > 0$. How-

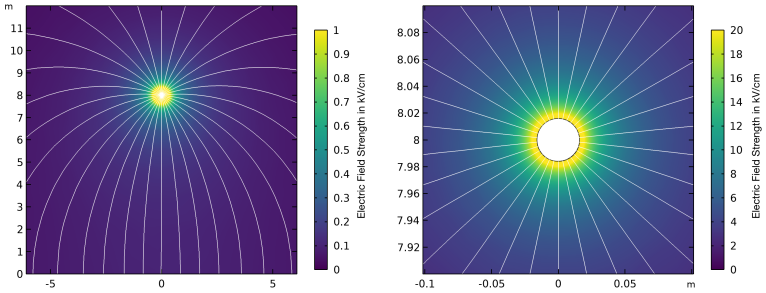

Figure 2.1: Illustrative example of a cylindrical conductor above ground seen from afar (left) and closer to the line (right). The cylinder has a diameter of 31.9 mm, is at a height of 8 m and is energized at 273 kV to match a line discussed in part II. Note the different colour scales left and right.

ever, overhead lines are commonly operated at voltages such that this would not happen on a smooth conductor. The problem of corona generally arises when the conductor surface is no longer smooth.

Streamer criterion

Indeed, the surface electric field can be greatly enhanced if the cylinder has a small protrusion as displayed in figure 2.2. The conditions (geometry and voltage) are identical to those of figure 2.1 except for the small half ellipsis at the bottom of the otherwise smooth conductor (carefully note the different colour scales). It is typically in this form of electrode arrangements that corona discharges are observed.

From the left-hand side plot in figure 2.2, a quantity called the streamer integral K can be derived such that:

$$K = \int_0^{x_1} \alpha_{\text{eff}} \cdot x \, \mathrm{d}x \tag{2.2}$$

where x_1 is such that for all $x \in [0, x_1]$, $\alpha_{\text{eff}} > 0$; α_{eff} itself being a function of the position dependent field. Different methods for obtaining α_{eff} are briefly discussed in section 5.3. Combining equations (2.1) and (2.2) it appears that K is the natural logarithm of the number of free electrons $K = \ln N_{\text{e}}$ due to particle collisions in the supercritical region of the electric field along the integration path.

When the streamer integral reaches or exceeds a certain threshold value $K \geq K_{\text{S}}$, that some authors call streamer criterion or streamer constant, and which is generally accepted to be around 18, a necessary and sufficient condition is fulfilled for partial discharges to occur in the kinds of non-uniform electric fields encountered around overhead lines. Indeed, at that point the discharge process is self-sustained. That being said, the general validity of the streamer criterion has been discussed and questioned recently by authors such as Färber et al. (in preparation) and Rabie and Franck (2016).

Coronating protrusions or corona sources

The most important kind of protrusions causing field non-uniformities relevant to corona on overhead lines are water droplets forming on the conductor surface, generally on a line wetted through rain, but also possibly via other weather conditions. It has been observed, that while the distribution and size of water droplets on an overhead line depends on many aspects, those droplets that do coronate tend to have a conical shape referred to as the *Taylor cone* (Schultz, Pfeiffer, and Franck 2015; Taylor 1964). As will be discussed in detail in chapter 9, this shape facilitates the field enhancement required to fulfil the streamer criterion.

Corona on overhead lines can also occur on a completely dry line. This is usually called fair weather or dry corona, as opposed to foul

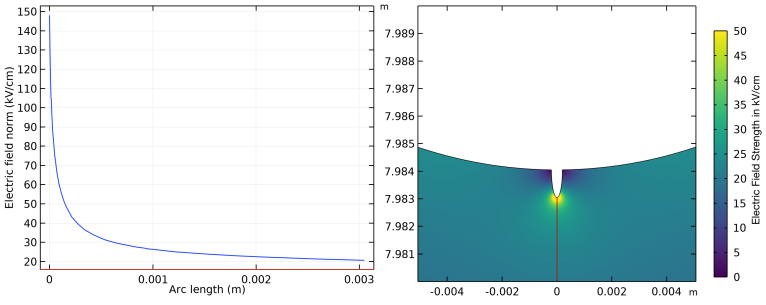

Figure 2.2: Illustrative example of the cylindrical conductor from figure 2.1 with a protruding particle at the bottom. The left plot represents the field strength along the red line on the right figure from top to bottom. Note the different colour scale compared to figure 2.1.

weather or wet corona. Newell and Warburton (1956) have shown, on AC overhead lines, that airborne particles such as insects, pollens and other kinds of pollution are mainly responsible for dry corona, rather than dents on the metallic surface of the conductor or other such defects. As a matter of fact, those airborne particles as coronating protrusions are reported to be considerably more of an issue in DC overhead lines since electrostatic effects can cause them to better stick to conductor surfaces than for AC lines (EPRI 1993).

Surface field calculation

The paragraphs above delineate why a sufficiently high electric field strength at the conductor surface is a *conditio sine qua non* for corona to occur on overhead lines. This surface field strength or surface potential gradient, often times and somewhat abusively, referred to as “surface gradient” or even “field gradient”, is thus the most important factor determining the corona performance of an overhead line.

Several methods, analytic and numerical, exist to determine this surface field strength, good overviews of which are given for instance in (Maruvada, Bacha, et al. 1979) or (Maruvada 2000, Ch. 2). In this thesis, an analytical method is used only for single cylindrical conductors above a ground plane:

$$E_{\text{surface}} = \frac{U}{r \ln \frac{2h}{r}} \tag{2.3}$$

where h is the line's height above ground, r the conductor radius and U the line voltage.

Numerical methods used are the charge simulation method (CSM) and the finite element method (FEM) (Zhou 1993).

2.3 Discharge modes

The polarity effects mentioned at the end of section 2.1 along with other factors such as the degree of non-uniformity of the electric field and the space charge environment around electrodes determines different modes for corona discharges. Trichel (1938, 1939) was the first to categorize such discharge modes.

Nowadays, corona discharges are generally classified by the polarity of the electrode and in order of increasing voltage as such: 1. burst corona, 2. onset streamer discharge (pulse), 3. positive glow discharge, 4. positive prebreakdown streamer discharge for positive electrodes and 1. Trichel streamer discharge (pulse), 2. negative pulseless glow discharge, 3. negative prebreakdown streamer discharge for negative electrodes. These are conveniently summarized in (EPRI 1993, Ch. 3) or (Maruvada 2000).

Some of those modes result in relatively continuous discharge currents while others express themselves as pulses of varying amplitudes and repetition rate. Experimentally, such characteristics are generally assessed using partial discharge (PD) measurement techniques

(IEC 2000). However, traditional partial discharge measurement involves large coupling capacitors and other kinds of equipment that can be expensive and/or impractical for measurements on overhead lines. Fortunately, the corona related overhead line design criteria are generally dictated by easier to measure secondary effects caused by the discharges, but not directly the discharges themselves. These secondary phenomena all fall under the umbrella term of *corona effects* and are described below.

2.4 Corona effects around HVDC overhead lines

Historically, high voltage alternating current (HVAC) technologies have dominated the energy transmission landscape mostly due to the transformer; required for the high voltages that diminish ohmic losses but, that only works with alternating currents. The advent of thyristors valves in the 1970s and later insulated-gate bipolar transistor (IGBT) valves in the 1980s led the way to more high voltage direct current (HVDC) connections, which have many advantages over HVAC links (Alassi et al. 2019).

In these circumstances, the full or partial conversion of an HVAC line to a fully HVDC (CIGRE Working Group B2.41 2014) or hybrid HVAC/HVDC line where multiple systems share the same right of way or towers (Neumann et al. 2013; Prommetta et al. 2019) are considered or even under construction (Übertragungsnetzbetreiber 2021).

This trend towards HVDC transmission lines is one of the driving forces behind new research efforts in corona effects around overhead lines and one of the reasons for the focus of this thesis on HVDC corona.

Secondary effects caused by corona include (EPRI 1993; Maruvada 2000) acoustic noise emissions, radio interferences, corona losses, UV light emission, ozone formation etc...

While the list above is valid for both AC and DC systems, there is one important macroscopic effect that occurs around HVDC or hybrid

AC/DC lines and not around exclusively HVAC lines. Indeed, DC components of the electric field will cause charge carriers generated through corona to travel either to ground or to adjacent conductors or structures.

Therefore, around a coronating HVDC overhead line, the space charge free Laplace field determined by the line geometry and voltage is modified by the space charge carriers caused by corona and becomes a Poisson field. Simulation methods for such ion flow fields around overhead lines have been discussed by authors such as Guillod, Pfeiffer, and Franck (2014), Zhang et al. (2013), and Zhou et al. (2012).

This ion flow is a secondary corona effect by itself, and the ion flow's effect on the electric field can also be seen as one.

Quantities of interest

In this thesis the corona quantities of interest are either traditional partial discharge measurements or one of the following corona effects: the corona loss current along the line, the ion current density at ground level, and the electric field strength at ground level.

The corona loss current is the current caused by the energy that is dissipated through the occurrence of corona along that line. Those losses include:

- the heating of the surrounding air, also responsible for acoustic noise emission via the sudden expansion caused by pulses,
- all forms of electromagnetic radiation, whether as radio interference or emitted light,
- the electrochemical energy required to change the chemical composition of the gas for instance through the creation of ozone in air.

In purely AC systems, these losses occur in a small region around the conductors. For systems with DC field components, a net space charge current will flow from the line towards ground or to other electrodes.

The ion current density at ground level, and the electric field strength at ground level directly relate to the electromagnetic environment around HVDC overhead lines. This environment is defined by the electric field strength, the ion current density and the space charge density (IEEE 1990).

Over a certain defined area on ground, the ion flow can be measured as an ion current density per unit of surface at ground level. The electric field affected by the changing space charge environment is particularly relevant at or closely above ground, since this is where it will generally be limited by regulations. It is also where placing sensors is easiest.

2.5 Test lines

In figure 2.3, a high voltage source U_{HV} is connected to an overhead test line conductor that has a parasitic capacitance towards ground due to its geometry C_{geom}. Indeed, in high voltage engineering, test objects and equipment tend to be so physically large that their parasitic capacitance becomes an important parameter. For a simple cylinder above perfect ground (Paul 2006) it is given by:

$$C_{\mathrm{geom}} = l \cdot \frac{2\pi\epsilon}{\cosh^{-1}(h/r)} \tag{2.4}$$

where l is the line length, h its height above ground r the conductor radius, and ϵ the permittivity of the surrounding material, in this case air.

Additionally, high voltage sources, especially large ones, generally have a non-negligible parasitic capacitance of their own, along with associated equipment such as voltage dividers and coupling capacitors for partial discharge measurements. Those are not represented in the schematic of figure 2.3.

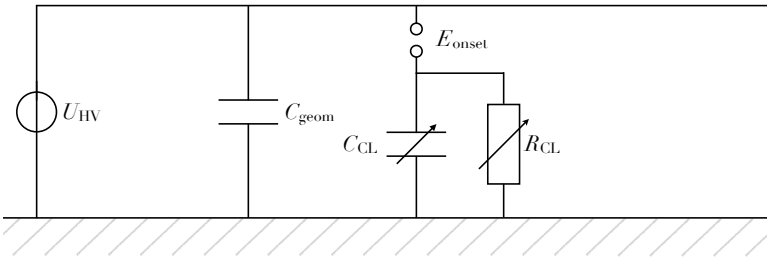

Figure 2.3: Simplified lumped elements model of a overhead test line that can be subjected to corona effects based on descriptions in (Kudyan and H-Shih 1981; Liu, Zhang, et al. 2011). With no corona discharge, the overhead line is a simple capacitance towards ground C_{geom} dependent on its geometry and connected to a high voltage source U_{HV}. The spark gap marked E_{onset} remains open. When the electric field E somewhere around the line is sufficient for corona to occur, $E > E_{\text{onset}}$ and space charges flow through C_{CL} and R_{CL}.

In normal operation of a test line, nothing else is connected to the high voltage source. The line is unloaded and the leakage currents through the insulators holding the line mechanically are neglected (i.e. the resistance of the insulators towards ground is considered infinite). The voltage source is only energizing the conductor by maintaining it at a certain electric potential but doesn't have to supply any current as long as there is no corona.

Corona onset

Corona discharges can occur anywhere on the line where the electric field E is subjected to non-uniformities such that E exceeds the so-called corona onset value E_{onset}. In the simplified schematic of figure 2.3, those discharges are modelled by the spark gap marked E_{onset} that is open as long as $E < E_{\text{onset}}$ and closes when $E \geq E_{\text{onset}}$. The generated space charge will modify the parasitic capacitance of the line as modelled by C_{CL} and the corona losses are modelled by a current flow towards ground counted as ohmic losses through R_{CL}.

There exists an empirical formula used to determine the corona onset E_{onset}. Named after Peek (1920), corona onset gradient in kV/cm is given as a function of the conductor diameter and surface condition, and the relative air density.

$$E_{\text{onset}} = E_0 m \delta \left(1 + \frac{K}{\sqrt{\delta r}}\right) \tag{2.5}$$

where E_0 and K are empirical constants (respectively 33.7 kV/cm and 0.24 $\text{cm}^{1/2}$ for positive and 29.8 kV/cm and 0.31 $\text{cm}^{1/2}$ for negative HVDC lines), m quantifies the irregularity of the surface (from 1 for perfectly cylindrical conductors to as low as 0.2 for very irregular conductors), $\delta = \frac{273+T_0}{273+T}\frac{p}{p_0}$ is the relative air density as a function of temperature and pressure, and r is the conductor radius (EPRI 2005; Maruvada 2000).

In dry conditions, a stranded conductor might typically have an irregularity factor of $m = 0.75$ which would result in an onset value of $E_{\text{onset}} \approx 27\,\text{kV/cm}$, slightly above the around 24 kV/cm that a 400 kV HVDC overhead line is realistically operated at (Pfeiffer and Franck 2015).

Other kinds of test setups

Some researchers also commonly use so-called *corona cages* in place test lines (Comber and Zaffanella 1974; Lekganyane, Ijumba, and Britten 2006; Nakano and Sunaga 1989). In a corona cage, the high voltage conductor is placed inside a co-axial hollow enclosure, generally cylindrical, the cage, that is grounded. Such setups can prove be more convenient and economical compared to test lines (Comber and Zaffanella 1974).

Chapter 3

Research Context for HVDC Corona

Rather than a traditional or comprehensive literature review, this chapter aims to demonstrate the many diverse perspectives one can have on overhead line corona research. Indeed, the diversity in approaches is manifold, and in the paragraphs that follow the idea is not to list closed categories but rather show overlapping areas of focus researchers, past and present, have had. The intention is to highlight transversal themes to which the present thesis can make contributions as described later in chapter 4.

Relevant literature is also provided in other chapters of this work, directly within the context of particular results presented.

3.1 Time and place

Motivations for investigating corona effects can vary a lot depending on time and place.

Historically an important focus of research on HVDC overhead line corona has been the radio interferences they can cause (Hirsch and

Schafer 1969; Knudsen and Iliceto 1974; LaForest et al. 1963; Mather and Bailey 1961; Morris, Morse, et al. 1979; Sawada et al. 1977). With the advent of digital communication during the last half a century, which are more resilient to interference, these have become less of an issue, exemplifying how the context of a given time era can dictate what angle of a phenomenon is studied.

Similarly, the study of altitude dependence of corona effects is most fitting in regions of the world where transmission lines have to cross large topographical hurdles. Authors such as Zhao et al. (2017) have reported about four 100 m long test HVDC lines being built at 50 m, 1700 m, 3400 m and 4300 m respectively, between Beijing and Tibet. Others have used a 6×6 m mobile corona cage at five altitudes between 0 m and 4300 m (He et al. 2017) for AC tests. In South Africa, Parus et al. (2017) have a mobile setup on a car trailer that allows them to present results ranging from 135 m to 1900 m in altitude. Of course altitude can also be simulated in laboratories using artificial environments such as reported by Li, Cui, et al. (2014).

Some issues can also be tied to the built environment in a specific territory. For instance in China, agricultural greenhouses in proximity of HVDC overhead lines is of concern. Indeed, the ion flow field around the conductors can cause significant field enhancements in the presence of dielectric films above ground such as those used in greenhouses (Chen, Lu, and Wang 2020).

Meanwhile, in Europe, audible noise emissions caused by corona is currently a major driver of research on overhead line corona, as mentioned in chapter 1. But naturally, corona audible noise is not a problem unique to Europe in the 2020s.

3.2 Audible noise prediction formulas

The issue of audible noise has been studied for many years and there exists a number of widely used and available empirical formulas that for a given conductor bundle geometry and calculated surface field

value predict noise emissions for both AC and DC lines (CIGRE WG 36.01 1974; Task Force of the Corona and Field Effects Subcommittee 1982). A number of the more often used of those formulas have in fact been implemented in an open source project of ETH Zurich's High Voltage Laboratory (*HVLBuzz* 2017), which even includes a proposed extension of existing formulas for hybrid AC/DC overhead lines (Hedtke, Bleuler, and Franck 2021; Hedtke, Pfeiffer, Franck, Zaffanella, et al. 2015).

Some formulas can be adjusted to account for parameters such as altitude (Chartier, Lee, et al. 1987) or rain rate (Comber and Nigbor 1976) in the hope of increasing their predictive power. However, as noted by their authors themselves, those formulas should preferably be used in conjunction with actual long-term measurements of lines similar in design (bundle geometry and conductor materials) located in "similar climatic conditions" (Chartier and Stearns 1981). Regarding rain rate, attempts have been made to infer long-term results from short-term measurements, but they can come with limitations such as the need for the conductor to be completely wet for them to be valid (Lundquist 1984).

Many other factors on the other hand, are generally not directly accounted for in noise prediction formulas. Those include conductor surface geometry (Pfeiffer, Schultz, et al. 2016), treatments (Kirchner and Franck 2022; Pischler and Schichler 2018) and condition (Yi, Chen, and Wang 2017) or, pollution of the surroundings (Ma, Zhao, et al. 2007).

Among those formulas, the ones for DC that are well documented enough to be widely used are those by EPRI (EPRI 1993), BPA (Chartier and Stearns 1981) and CRIEPI (Fukushima, Tanabe, and Nakano 1987). EPRI measurements were performed in Lenox (Massachusetts, USA) at the Project UHV facility (Comber and Humphreys 1979). BPA relies on measurements by the IREQ in Varennes (Quebec, Canada) (Hylten-Cavallius and Train 1974; Maruvada, Trinh, et al. 1977) as well as at BPA's own Lyons test site in The Dalles, Oregon, which has been

especially developed to "evaluate corona performance of [a specific] design in typical Pacific Northwest conditions" (Perry, Chartier, and Reiner 1979). BPA also used results recorded along the Square Butte HVDC link between North Dakota and Minnesota. CRIEPI's measurements were made on its test line in Shiobara (Tochigi Prefecture, Japan).

For AC, a few European test sites are frequently cited in addition to those listed above. The Anneberg EHV test station on the western coast of Sweden (Lundquist 1990), ENEL's in Suvereto (Tuscany, Italy)(Cortina et al. 1980) and EdF's Les Renardières research centre in Écuelles (Seine-et-Marne, France) (Gary and Moreau 1976).

As noted repeatedly by their authors at the time when the DC formulas were first introduced, the datasets upon which they are based are small. Moreover, they do not quantify the variability to be expected around the average noise emission value they provide.

In recent years there has been a renewed interest for similar measurement campaigns in regions previously ignored such as South Korea (Shin et al. 2019) and Switzerland (Hedtke, Pfeiffer, Gobeli, et al. 2018).

3.3 Experiment scale and duration

As the different altitude related experiments referred to in section 3.1 show, setups to test corona effects can have very different scales. Maruvada (2000) differentiates (from physically small to large) between laboratory test cages, outdoor test cages, outdoor test lines and operating lines. This list obviously omits many kinds of setups, for instance indoor test lines, such as the one presented in section 6.2, or smaller setups meant to isolate specific processes in order to better study them.

Different scales can also be found in the duration of experiments. In contrast to AC, in DC, fair weather corona activity is of at least as much interest as foul weather corona. Indeed, airborne particles such as insects, pollens or other sorts of contaminants may have a tendency to

stick to the line and form corona sources due to electrostatic forces. These sources could be washed away when exposed to rain and introduce cyclic trends in corona activity, highlighting the importance of long-term outdoor setups to study such phenomena (EPRI 1993) with time scales of at least rain events to compare the situation before and after rain, but also entire seasons since the type and amount of airborne particles will depend on them.

Following, among others, the pioneering long-term experimental results obtained by Bailey (1967), Gehrig et al. (1967) or by Maruvada, Trinh, et al. in (Maruvada, Dallaire, and Rivest 1984; Maruvada, Trinh, et al. 1977; Maruvada, Trinh, et al. 1981), it is established that on HVDC overhead lines, rain generally causes radio interference and audible noise levels to decrease while increasing corona losses compared to fair weather.

Humidity is also often cited as an important influencing factor for HVDC corona losses. Hirsch and Schafer (1969) give linear factors for the increase of corona losses per g/kg of absolute water content in air based on outdoor test line measurements. Xu, Zhang, Chen, et al. (2016) and Xu, Zhang, He, et al. (2015) have studied the effect of humidity in a 1 m long laboratory corona cage. Gallo, Germanos, and Courtney (1969) used environmental chambers with wire plate electrodes and focused on the corona discharge phenomena specifically. Contrary to Hirsch and Schafer, they found that relative humidity was a more important factor than absolute humidity.

Wind considerations are also an important difference between AC and DC corona. This is especially true in fair weather conditions, when the impact of wind on water droplets at the conductor surface is not relevant. Without wind, the space charges created by DC corona will travel along field lines exclusively. Wind is an additional component to the velocity vector of those space charges and will impact corona behaviour by changing the field conditions around conductors.

3.4 Technological advances

Although transmission lines are long-term investments in which the adoption of new technologies is rather slow, as time goes by, new technologies do become available. In terms of overhead line corona, one could mention for instance advances in material sciences or new sensing methods.

Indeed, new materials or surface treatments might help improve conductor surfaces to get performance closer to that of aged conductors (Straumann and Weber 2010).

Moreover, many measurement campaigns mentioned in this chapter have been restricted by the technology of their time and would be at least significantly easier or more practical to perform nowadays. For instance, while Morris, Staniforth, and Morse (1971) present a setup capable of measuring both the corona loss current and the radio interference caused by corona simultaneously, it shows the huge complexity involved in such an endeavour, including frequency modulation (FM) transmitters, fibre optics connections carrying analogue signals, magnetic tape recorders etc... In fact, similar FM transmitters are quoted to have a battery life of maximum 3 to 4 days in (Maruvada, Dallaire, and Rivest 1984) which is extremely limiting in the context of long-term measurements. In (Mather and Bailey 1961), it is explicitly mentioned that charts for a year's worth of half-hourly data is entered by hand to punched cards. Modern methods would of course allow to automate this process but also to set much shorter sampling periods more in line with time constants of weather changes.

Chapter 4

Aims and Scope of this Work

4.1 Main objectives

The previous chapters make clear that environmental parameters and conductor surfaces are two areas where corona research is very active and where significant progress is still to be made. On the one hand, they highlight the need for more long-term monitoring of corona effects in a wider range of specific climates and environments; because corona is so dependent on external parameters to which the line is exposed. On the other hand, the conductor surface itself is also a major influencing factor, but the fundamental interactions by which it impacts corona are not fully understood and not well modelled.

Ideally, corona should be characterized over several years at different locations along entire transmission lines. Measurement campaigns of the past have, however, been limited to very few localities and were often huge undertakings that are too resource and workforce intensive to be realistically deployed at the scale of entire grids. Even today, this limits available data. Especially so in regions of the world that have established grids. Indeed, in those regions the funds allocated to better understand corona effects are often lesser than in regions where the construction of new overhead lines is in full swing, despite the urgent

need for more grid capacity.

The scope of this thesis is relatively broad, but every topic it contains has the same aim. That is, to present measurement methods and instrumentation, visualization and evaluation techniques, or, specific metrics of influencing parameters; all in order to better understand and quantify the long-term corona performance of overhead lines given the local conditions they find themselves in; and this, by leveraging modern technologies to reduce the efforts required to obtain meaningful results.

To achieve that, prior work from literature is reviewed in light of today's techniques and possibilities in terms of surface engineering, sensor technologies, data processing etc... Using newly introduced tools, it is highlighted that large endeavours of the past become imaginable for smaller teams and wider deployment.

Ultimately, the ambition is to create a modern and practical toolbox for corona research.

This toolbox contains novel measurement instruments in the form of corona sensors based on a unified IoT platform. The sensors developed are key enablers for uninterrupted long-term outdoor measurements of overhead lines and their low cost allows for deployments covering large territories. Some methods are also introduced to make conventional measurement techniques more useful, especially in the context of long-term HVDC corona.

The toolbox also includes data analysis and visualizations intended to help interpret long-term data in more meaningful ways. Statistical approaches reveal trends in large datasets without hiding their inherent variability.

Metrics are defined or introduced, ranging from characterization of conductor surfaces to the classification of weather phenomena that enable a better understanding of the fundamental influencing factors of corona performance.

In the process, long-term outdoor measurements are performed and

conclusions about specificities of corona behaviour in the Swiss urban environment can be made and compared to earlier studies often performed on other continents.

The intention is that the results presented in this work is to further demonstrate the need for more long-term measurements spread in more geographic locations but, also more importantly, give tools and indications as to how to perform and process them to obtain relevant outcomes.

While a greater emphasis is put on HVDC phenomena, the tools, methods and conclusions from this work are not limited to HVDC overhead lines and can also be applied to HVAC or hybrid AC/DC overhead lines to some extent.

4.2 Structure of this thesis

Part I introduced the motivations and the context for this thesis. This identified research gaps this thesis intends to fill.

In **Part II** the different setups used for the results reported in this work are presented.

Part III introduces a unified IoT sensor platform to measure corona effects. **Chapter 7** shows how IoT technologies are useful for corona research and puts them in context with methods used in literature. **Chapter 8** presents the implementation of those technologies within a specifically developed sensor platform.

Part IV shows results for several short-term experiments. First, **Chapter 9** investigates the macroscopic behaviour of single water droplets subjected to an electric field and how they deform to produce partial discharge depending on the surface properties of the substrates on which they sit. Metrics for surface wettability are introduced (contact angle measurements, stickiness of droplets) and predictive formulas for the conditions needed for a discharge to occur are given. In **chapter 10** novel data visualizations are presented. 2D histograms

are employed for partial discharge data from traditional PD measuring systems in ways that are better suited for HVDC overhead line measurements. Then, plots based on quantiles are shown to convey the highly dynamic nature of ground level ion current signals in **chapter 11**. **Chapter 12** presents results from three sensors based on the IoT platform mentioned above working concurrently to measure different physical quantities from the same coronating overhead line. The platform's ability to discriminate different conductors based on their corona performance is demonstrated and the complementarity of different corona measurements methods is discussed.

In **Part V**, long-term measurements of corona loss current data from an outdoor HVDC test line are presented. Comparisons are made with data reported in literature. **Chapter 13** introduces the results and elaborates on their acquisition and analysis. **Chapter 14** takes an overall look at the measurement results, discusses fair weather corona and examines the effect of humidity. Finally, **chapter 15** focuses on what metrics allow to best characterize foul weather corona behaviour.

Part VI concludes this thesis and gives an outlook on possible future works.

Part II

Available Test Setups

Chapter 5

Long-Term Outdoor HVDC Overhead Test Line

5.1 Why this setup?

On the rooftop terrace of the building that houses ETH Zurich's High Voltage Laboratory a reduced-scale outdoor HVDC test line has been installed. This test line is thus referred to as the *rooftop* test line. It serves many purposes that can broadly be categorized in the bullet points below:

- To find out how specificities of the experiment's environment and climate affect corona performance. Do results previously reported in literature for other geographic locations adequately describe behaviour in a Swiss urban context? What variability in corona behaviour can be observed for a given set of real conditions.
- To serve as a test bed for sensor technologies. Using this test line, sensors in development can be tested while measuring real corona effects albeit at absolute values that may vary from full-scale geometries. But all the influencing parameters one would find on a full-scale transmission line are present here as well.

Moreover, the sensors are exposed to outdoor conditions and their weatherproof qualities, ruggedness and reliability can be evaluated in real operating conditions.

- To help determine metrics for long-term corona performance. This is not limited to the selection of quantities that should be measured. It also includes how they should be measured, in what form the data should be saved, and how it should be visualized and evaluated as discussed further in parts IV and V.
- To gather general experience in long-term outdoor measurement campaigns. This spans a whole range of problems from long-term data management to general difficulties associated with conducting science experiments in a partially publicly accessible outdoor environment.

Of course, a full-scale setup would offer operating conditions even closer to those of an actual transmission line, but this reduced-scale setup also presents practical advantages. First of all, its geographic location directly at ETH Zurich's High Voltage Laboratory is key to enable short iteration loops of everything developed in the context of this work.

A smaller setup also allows to have more auxiliary components housed indoors compared to a full-scale outdoor experiment. This critically includes the voltage source. Not requiring the voltage source to be outdoor rated offers much wider options from which it can be selected including ones with performance ratings allowing a continuous long-term operation.

In section 6.3, a full-scale outdoor setup is presented that due to limitations of its voltage sources can not be operated continuously over days. Moreover, its remote location makes it less viable to work on. The setup described in this chapter does not suffer from these disadvantages.

5.2 Hardware description

This setup consists of a 10 m unloaded overhead line mounted on a frame allowing the line to be set at variable heights above ground. The line is energized using a rack mountable HVDC voltage source capable of delivering up to 60 kV and 3 mA.

The line is on the rooftop of the H-Floor of the ETL offices of ETH Zurich's High Voltage Laboratory (an official ETH Zurich test site) and is enclosed in a safety cage, monitored through a BaseCube safety controller. The BaseCube and the voltage source are inside the office building and connected to the outdoor setup through a cable duct running underground to an electrical cabinet outside.

Electrical quantities measured can include the source voltage and current, the line current, the electric field at ground level, the ion current at ground level and partial discharges on the line via a coupling capacitor.

Mechanical

The overhead conductor itself is from Lumpi Berndorf with type designation 34-AL3 (non ST1A). Listed in table 5.1 are the most important specifications of the line.

The frame is constructed using 40 mm Item profiles. The railing system for setting the height is made out of TEN Cam Roller Guides. The entire frame assembly is generously over dimensioned for the weight and tension it shall indulge as illustrated in the sag calculations of figure 5.1.

The high voltage armatures (clamps and guard rings) as well as the insulators are provided by EA Elektroarmaturen AG. The insulators have the specifications found in table 5.2

Conductor diameter	7.5 mm
Number of wires	7
Wire diameter	2.5 mm
Weight per unit length excl. grease	95 kg/km
Material (for all wires)	AlMgSi (Al-Alloy)
Rated tensile strength	10.14 kN
DC resistance	0,9572 Ohm/km
Final modulus of elasticity	60000 N/mm2
Coefficient of linear expansion	2.30E-5 1/K
Current carrying capacity	169 A

Table 5.1: Specifications of Lumpi Berndorf' 34-AL3 (non ST1A) overhead conductor.

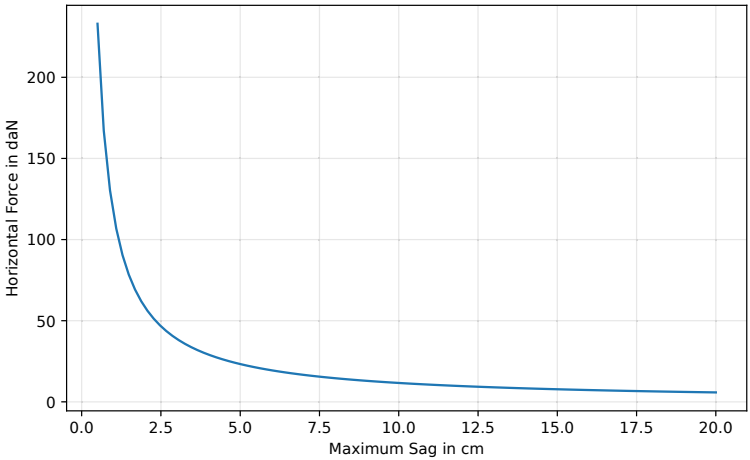

Figure 5.1: Horizontal force in decanewton required to achieve a certain sag on the considered line.

Dry lightning impulse withstand voltage	390 kV
Wet lightning impulse withstand voltage	200 kV
Creepage distance	1990 mm
Arcing distance	635 mm
Specified mechanical load	210 kN

Table 5.2: Specifications of the insulators.

Electrical

The voltage source is from Heinzinger's PNC series of *Precision High Voltage Power Supplies*. It is of type *PNChp 60000 - 3 ump.* with the options 02 / 04 / 22 / 60 / 76USB / M and serial number 3547 11625. It can output a maximum of 60 kV and 3 mA with either positive or negative polarity.

This voltage allows to attain the field gradients presented in figure 5.2 at the surface of the conductor depending on height (assuming the conductor to be a perfect cylinder without sag).

The high voltage cable connecting the power supply to the line is also from Heinzinger, type HVC65 with a length of 30 m. It is an insulated coaxial cable with an isolation voltage of 120 kV DC and a capacity of 141 pF/m which results in a total capacity of 4230 pF over its entire length. The line itself forms a parasitic capacitance with ground as illustrated in figure 5.3. This again is a function of line height. Note that the armatures or the safety cage's fence are not considered in these computations.

Additionally, the capacitive elements within the HVDC source itself have to be accounted for. Their values were communicated via email correspondence with the manufacturer.

In parallel to the line, there is also a 1200 pF coupling capacitor for partial discharge measurements. The capacitor is enclosed within an insulator tube recognizable with its silicone rubber sheds. At the base of the insulator, a large weatherproof case contains the coupling de-

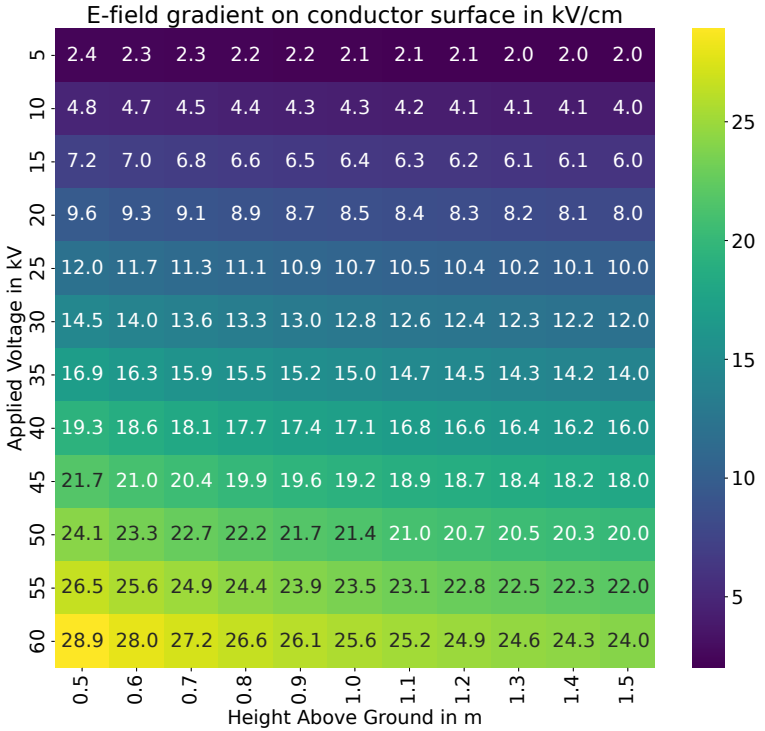

Figure 5.2: Maximum surface gradient of a cylindrical conductor with a diameter of 7.5 mm at various heights above ground for different applied voltages.

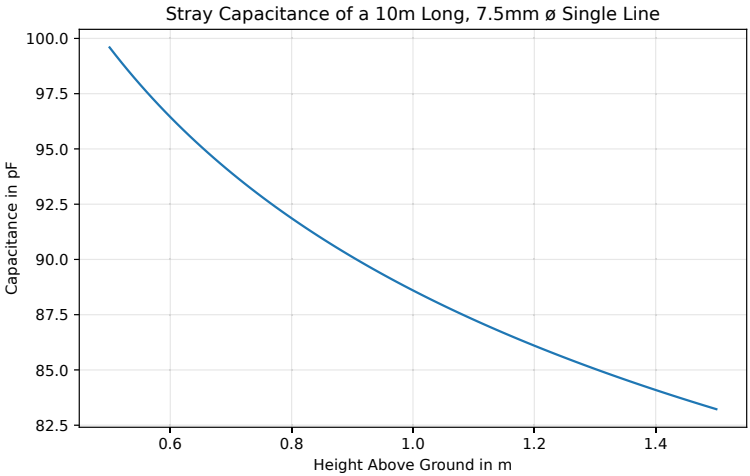

Figure 5.3: Stray capacitance of a 10 m long cylinder with a diameter of 7.5 mm at various heights above ground.

Element	Capacitance in nF
Boost Stack	1.175
Rectifier	1.175
Measuring Capacitor	2
Filter Capacitor	1.35
Source Total	3.9

Table 5.3: Capacitive elements within the Heinzinger *PNChp 60000 - 3 ump.* high voltage source.

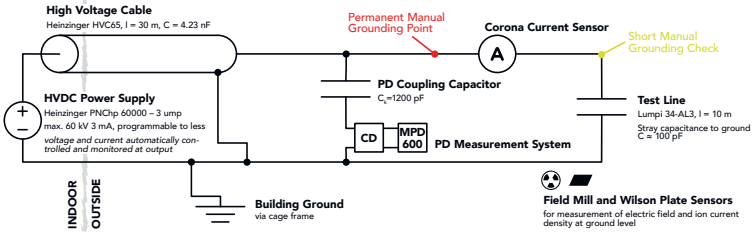

Figure 5.4: Schematic diagram of the test circuit.

vice and Omicron MPD600 unit.

This results schematically in the configuration of figure 5.4.

To connect the high voltage cable to the overhead line, while avoiding discharges at the coaxial cable's end or along the junction to the overhead line, a custom bushing installation has been implemented.

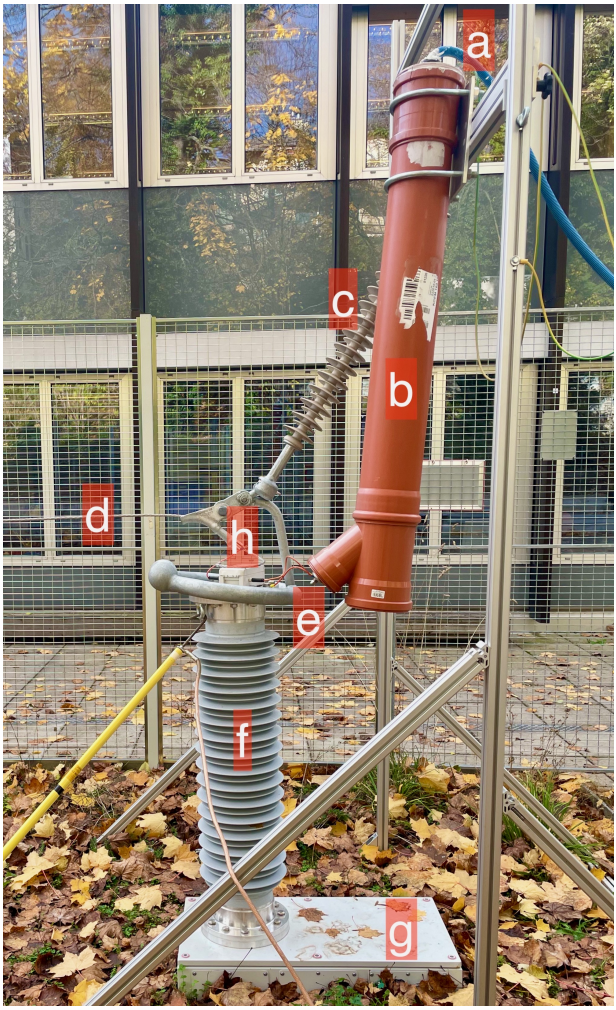

Figure 5.5: Photo of the setup showing:(a) the main cable coming from the source to (b) the custom bushing. (c) The insulator holding the corona guard ring and clamp (e) and the line (d). (f) The coupling capacitor and (g) weather sealed box housing the Omicron system. Around (e) the high voltage red connection cable at the output of the bushing (b) is visible. It first goes through an on-potential corona loss current sensor (h) placed on the coupling capacitor (f) before connecting to the line behind the clamp.

5.3 Field considerations for small diameter conductors

Of course, this setup does not reflect full-scale operating conditions, in particular due to its geometry. In this section some considerations are made about what this entails, and the line is compared to that of the full-scale setup located in Däniken and presented in section 6.3.

Conductor manufacturers generally give diameters for the individual strands d as well as an overall conductor diameter D. When all strands have the same diameter, as is the case for most commercially available AAAC conductors, the relationship between the diameter of individual strands and that of the overall conductor should be given by the well known mathematical problem of circle packing, specifically that of 2D circle packing in a circle. A lot of (if not all for the case of AAAC) commercially available conductors have $3k(k+1)+1$ strands (with k being the number of layers around the central strand) which happens to be a class of mathematical problems of its own (Lubachevsky and Graham 1995). Such overhead conductors were already studied by Peek (1920) over a century ago when he introduced his irregularity factor, (the parameter m seen in equation (2.5)).

However, for the 61 strands 600-AL3 conductor used in the Däniken line, the outer diameter given by the manufacturer is larger than what mathematics would suggest. Indeed, according to data sheets, the ratio is $\frac{D}{d} = \frac{31.9\,\text{mm}}{3.54\,\text{mm}} = 9.01$, while an optimal ratio would be 8.66 (Lubachevsky and Graham 1995).

For simulation reasons, the diameter of the individual strands is set to be that of the data sheet while the overall diameter is such that the outer layer of strands forms a full circle using the optimal ratio.

The stranded nature of conductors means that the actual maximum field gradient observed at the conductor surface is significantly larger than that given by the cylindrical approximation usually used when designing overhead lines. While these discrepancies are generally not an issue, when comparing a full-scale geometry such as that from

Conductor angle	0°	5°	10°	15°	20°	25°
Surface gradient	34.58	34.62	34.61	34.57	34.61	34.60

Conductor angle	30°	35°	40°	45°	50°	55°
Surface gradient	34.60	34.57	34.58	34.62	34.57	34.58

Table 5.4: Dependency of the 7 strands conductor's maximal surface gradient in kV/cm on the conductor's angle around its own axis. Due to the symmetry of the conductor, only angles between 0° to 55° are studied.

Däniken to the somewhat extreme geometry of this thin rooftop test conductor so close to ground, this should be verified.

With the rooftop setup energized at 60 kV, the cylindrical surface gradient is 24.76 kV/cm using the analytical formula and 24.89 kV/cm using the charge simulation method. To reach this cylindrical surface gradient in the Däniken geometry, one would need to apply a voltage of 273 kV to the line. Simulating those two geometries at these voltages in Comsol accounting for the strands, it is found that the stranded maximal surface gradient reaches 34.58 kV/cm for the smaller conductor and 35.02 kV/cm for the larger one. Those results are consistent with what has been reported in literature (Yamazaki and Olsen 2004). Moreover, the smaller conductor has a maximal surface gradient that is mostly invariant to rotation around its own axis as shown in table 5.4.

Of course, it should be noted that the considerations above are made for a pure Laplace field without regard for any space charge effects. Lu et al. (2011) have shown that while space charges do have an effect on the corona onset field of stranded overhead line conductors, it remains relatively small.

Number of strands	7	61
Parabolic (Beyer et al. 1986, equation 7.119)	10.5	18.1
Bolsig+ (Hagelaar and Pitchford 2005)	6.5	11.2
Li, Li, et al. (2018) with 0 % relative humidity	3.8	5.9
Li, Li, et al. (2018) with 100 % relative humidity	4	6.3

Table 5.5: Streamer criterion from a small protrusion sticking from either a small or a large conductor and using different formulations of α_{eff}.

Streamer considerations

As discussed in chapter 9, the streamer criterion which conditions corona onset is greatly dependent on local field conditions around the protrusion. Despite very similar maximal values for the surface gradients, the different geometries could mean that the field falloff from the tip of a protrusion are different enough to impact the streamer criterion.

An ellipse shaped protrusion is thus added to both lines modelled with their strands. The ellipse has a semi-major and semi-minor axes of 1 mm and 0.2 mm respectively and its centre is on the bottom most point of the stranded conductor free of protrusion. This protrusion is intended to loosely resemble a coronating insect sticking to the conductor, at least in its dimensions. Figures 2.1 and 2.2 illustrate the effect an analogous geometry has on the local electric field around a purely cylindrical conductor.

The streamer criterion following a field line starting at the tip of such a protrusion is given in table 5.5 for both conductors. The streamer criterion is calculated using field values from an FEM simulation, different references for the effective ionization coefficient α_{eff} and a simple numeric integration. At the tip of the protrusion, the local electric field can exceed 160 kV/cm which is much larger than the 60 kV/cm up to which the parabolic approximation for α_{eff} is generally accepted to be valid (Beyer et al. 1986). Nevertheless, looking at the first line of

table 5.5, indicates that it could be easier for the same insect to start coronating in the Däniken setup rather than this rooftop setup.

Humidity and other atmospheric parameters

Humidity has been shown to have an impact on corona losses on HVDC lines.

Recently Li, Li, et al. (2018) have calculated α_{eff} for different humidities. Streamer criteria using their effective ionization coefficient are also presented in table 5.5.

Other atmospheric parameters such as air pressure or temperature are generally reported to affect corona performance principally via the ease of onset as well. The main mechanism being their action on gas density as expressed for instance in the δ of Peek's formula (equation (2.5)).

5.4 Weather data acquisition

An automated weather station from the Swiss Federal Office of Meteorology and Climatology (MeteoSwiss) is located at exactly 1 km from the test site. Its data is freely available for registered researchers.

Directly at the test site, a Davis Instruments Vantage Pro2 prosumer weather station has been installed. It stores its data to the cloud using Davis Instruments' WeatherLink service.

The two weather data sources are compared in figure 5.6 in terms of precipitation. The plots show relatively good agreement between both weather stations. A notable trade-off is that the WeatherLink data comes with a better time resolution compared to the MeteoSwiss precipitation data (a datapoint every 5 minutes rather than every 10 minutes), but the smallest amount of rain it can detect within one of those time periods is 0.2 mm rather than 0.1 mm for the MeteoSwiss station.

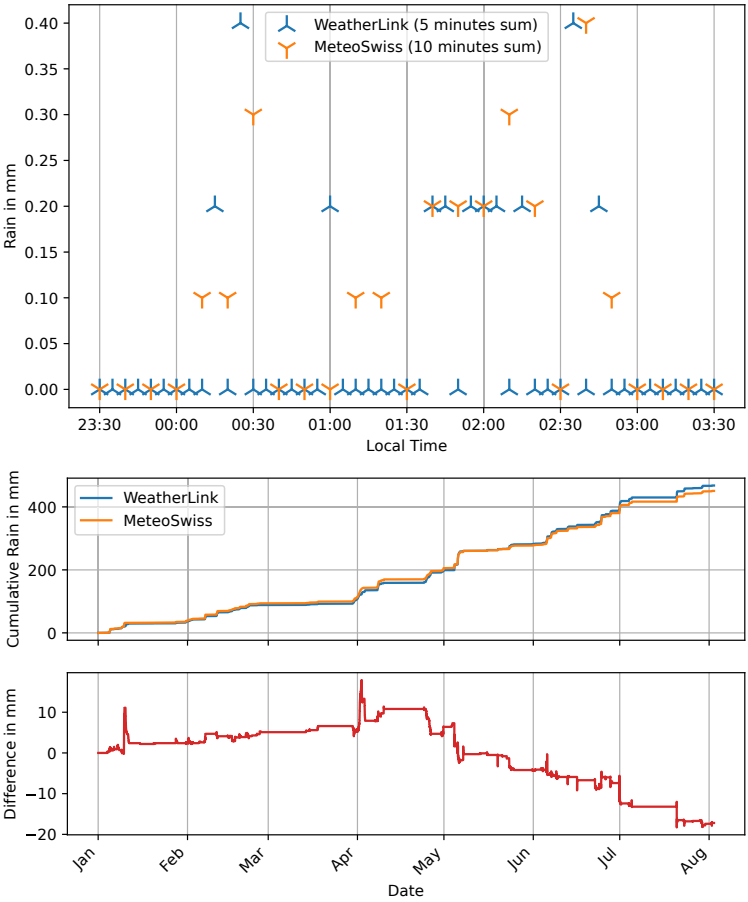

Figure 5.6: Comparing precipitation data from the MeteoSwiss station located 1 km away from the rooftop setup to the data sent to WeatherLink by a local Davis Instruments Vantage Pro2 station. Individual samples over a few hours (top) and cumulative rain over 8 months (bottom).

Chapter 6

Setups for Short-Term Studies

The setup described in chapter 5 does not allow to cover the entire range of open questions this work aims to tackle. As discussed in chapter 2, corona effects on overhead lines are very multifaceted phenomena with a plethora of influencing parameters. Specialized experiments can make it easier to isolate and control specific impacting factors.

Sometimes more precise setups, such as that described in section 6.1 are needed to study smaller scale interactions compared to what can be observed along an entire test line. Section 6.2 presents an indoor test line that can be subjected to controllable artificial rain. Finally, in section 6.3 an outdoor test setup for shorter measurement campaigns but benefiting from a full-scale geometry is introduced.

Unlike the setup described in chapter 5, the setups introduced in this chapter had all existed in a more or less similar form before the author of the present work started using them. Nevertheless, some amount of upgrades or the use of specific measurement instruments were made in the context of this thesis.

6.1 Single droplet setup

Rain is one of the most important influencing effects on overhead line corona since water droplets deposited on the conductor surface through rain form the protrusions that locally enhance the field above onset. This setup aims to better understand what mechanisms lead single water droplets to coronate in electric fields depending on properties of the conductor surface.

As a first step, the problem is reduced to that of droplets sitting on surfaces with specific features subjected to a uniform DC electric field. In surface engineering, droplets sitting on a surface are referred to as sessile droplets.

Modern surface engineering techniques allow the manufacturing of surface samples with specific wettabilities. Using processes described in (Stamatopoulos, Bleuler, et al. 2019) small copper discs with more or less hydrophilic or hydrophobic surfaces are produced.

In the setup depicted in figure 6.1, a vertical uniform electric field is created by two electrodes that have a maximum diameter of 160 mm, a planar circular surface with a diameter of 110 mm and are separated by 50 mm. The lower electrode has a cylindrical slot with a diameter of 50 mm and a depth of 1 mm to accommodate the insertion of the copper samples. This allows a sample to be placed in the lower electrode while its surface remains flush, and the field not significantly disturbed (as confirmed by numerical simulations).

The upper electrode is on ground potential while high voltage can be applied to the lower electrode. Partial discharge (PD) activity is measured by an Omicron MPD 600 measuring system according to norm (IEC 60270). The apparent charge noise floor is around 0.3 pC.

The inter-electrode space is backlit by an inexpensive LED video light panel covered by a LEE Filters 216 White Diffusion sheet. A video camera is placed outside the safety cage. Either a Nikon D5300 DSLR camera (filming at 59.94 fps in Full HD resolution) or a Photron FASTCAM Mini UX100 high speed camera (filming at 10 kfps to 20 kfps at reso-

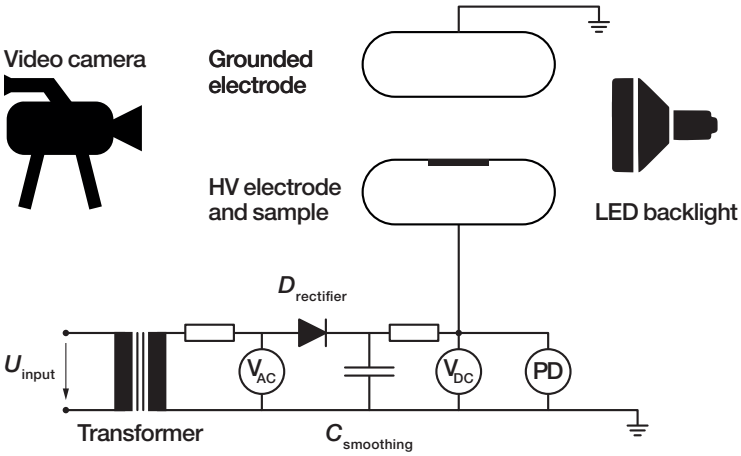

Figure 6.1: Schematic illustrating the experimental setup.

lutions in the order of 152 × 1280 depending on settings) both with a Nikon 200 mm f/4 AF-D macro lens is used. Due to their different crop factors, recordings with both the DSLR and the high speed camera yield a spatial resolution of approximately 30 mm/pixel. The high speed camera is electronically synchronized with the Omicron MPD system allowing to accurately associate PD measurements to each video frame. This is achieved by sending the camera's TTL trigger signal to the PD input of a second MPD unit.

The setup was later modified and used for follow-up studies as discussed in section 9.9.

6.2 Indoor test line with rain simulator

The *E31* indoor installation at ETH Zurich's High Voltage Laboratory offers the possibility to hang a 6 m section of overhead line under a rain simulator providing the repeatability of controlled test conditions. The single conductor is placed between two large toroids (that can influence the absolute value of the electric field) at a height of 2.5 m with a minimal sag.

In chapter 12, the setup is used to compare different conductors and benchmark the newly developed sensor platform from part III. This setup is otherwise practically identical to that used by previous authors such as Hedtke, Xu, et al. (2020), and is thus not further described in this work.

6.3 Outdoor full-scale test line

For the study of single HVDC lines, the main limitation of the rooftop test line presented in chapter 5 is its reduced scale. In this section, a setup that not only enjoys a full-scale geometry much closer to that of real transmission lines but that in addition to a monopolar DC bundle has a parallel AC bundle allowing the study of AC, DC and hybrid AC/DC configurations is presented.

Unlike the hybrid setup used in (Pischler, Hedtke, et al. 2019) where a single line is energized with a hybrid AC/DC voltage, this setup distinct lines, one AC and one DC. In this thesis, only results using the DC line alone are presented which also defines the scope of the rest of this chapter. The setup in its entirety has been described in more detail in (Hedtke, Pfeiffer, Gobeli, et al. 2018). That said, within the context of the present thesis, it has considerably been upgraded in regard to remote automation and monitoring capabilities afforded by the Yokogawa GP20 industrial data logger as well as a new local network that is now based on a fully managed UniFi system.

It is located on the testing ground of the FKH (Fachkommission für

Hochspannungsfragen) in Däniken, Switzerland (the setup is therefore referred to as the *Däniken setup*). This allows for larger geometric dimensions (distance to ground and walls, span, more realistic sag, distance between conductors) than what would be possible at ETH Zurich. The test line is also obviously subjected to actual weather conditions (precipitation and wind) and other climatic parameters that can affect the corona performance associated with an outdoor environment, such as dew and humidity.

The test line is formed by a double bundle (AAAC, 600 mm^2, typical for Switzerland) of a total length of 35 m and a height above ground at maximum sag of 8 m. The voltage source is composed of an AC test transformer excited by a variable transformer that first connects to an AC high voltage divider, to a rectifier diode and a DC high voltage divider and then to the line itself. The DC divider simultaneously also acts as a smoothing capacitor as well as a coupling capacitor for partial discharge (PD) measurements. On the low voltage side, a commercial PD measuring system is connected through a standard coupling device. The device is set so as to comply with IEC 60270 with a symmetric integration frequency range of 100 kHz to 400 kHz.

Weather information is provided by data from the Swiss Federal Office of Meteorology and Climatology and collected at an automated weather station less than 400 m from the test site.

The biggest limitation of this setup, as highlighted by experience, are the actual performance ratings of the voltage sources that do not allow continuous operation for more than a few hours.

Part III

A Unified IoT Sensor Platform

Chapter 7

IoT Technologies for Long-Term Outdoor Measurements

The Internet of Things (IoT) refers to any kind of devices or "things" equipped with sensors, software, and connectivity that enables them to collect and exchange data over the internet or other networks. IoT devices have the capability to

- connect to computer networks to send and receive data to each other and to other machines
- gather data through sensors
- process the collected data on-device or in cloud-based systems to extract meaningful information, and perform analytics to derive insights
- act with an important degree of autonomy.

For corona research, technologies associated with the IoT provide several advantages over techniques traditionally used in high voltage engineering. In particular, three important features typically associated with IoT devices are put forward in this chapter.

7.1 Wireless transmission of sensor data

As the test object (the overhead line) is energized at a high electrical potential, sensors close to the line or directly connected to the line itself need to be galvanically insulated from ground. In the past such methods as frequency modulated analogue radio signals (LaForest et al. 1963), amplitude modulated analogue radio signals (Comber and Humphreys 1979), D'Arsonval movement ammeters read from ground using small telescopes (Gehrig et al. 1967), audio transmission (Chartier, Shankie, and Kolcio 1970) or optical fibre cables (Liu, Zhou, et al. 2016; Pfeiffer and Franck 2015; Wang and Zhang 2008) have been used for this purpose.

Digital wireless transmission technologies ubiquitous in the world of IoT devices, such as Wi-Fi, Bluetooth and Zigbee greatly simplify data transmission while ensuring a high reliability and scalability (Bansal et al. 2019). Moreover, low-power wide-area network (LPWAN), such as LoRaWAN, NB-IoT and Sigfox enable long range (kilometres) connectivity even on low power and resource constrained devices (Ballerini et al. 2019).

Those protocols automatically handle the concurrent transmissions of several connected devices by distributing the traffic among multiple channels, avoiding packet collisions at the physical and networking layers, they can also detect transmission errors generally by using Cyclic Redundancy Check (CRC) codes and potentially fix them (Cao, Liu, and Wu 2021; Tsimbalo, Fafoutis, and Piechocki 2015). This is relevant in corona related applications, as the discharges can cause radio interference that might disturb wireless communication around an overhead line.

Moreover, compared to data transmission methods used historically, these protocols, by definition allow creating network of devices making it significantly easier and more secure to manage and combine data from several sensors concurrently. Such an arrangement of measurement devices would form a so-called wireless sensor network (WSN).

7.2 Low energy consumption

A common property of IoT devices is their low power consumption. Owing to this, sensors that need to be galvanically insulated can be battery powered and still function autonomously over extended periods of time, typically months, without requiring to be connected to mains power (Singh, Kaur, and Singh 2021). Even for sensors on ground potential, low energy needs are desirable, especially for devices intended to run continuously over months or years in possibly geographically remote locations.

The IoT ecosystem also provides many energy harvesting solutions that are of interest in this context (Singh, Kaur, and Singh 2021). Photovoltaic solar panels for example, constitute a promising method, particularly for outdoor applications. Considering average sunlight, a cell covering a few cm^2 combined with a small battery would be enough to cover all the energy need of a simple sensor. And for scenarios without access to sufficient sunlight, there exist other sources for energy harvesting (Elahi et al. 2020) such as temperature differences (Tuoi, Van Toan, and Ono 2022), vibrations (Rodriguez, Nico, and Punch 2019) and electromagnetic fields (Mezzanotte et al. 2021). While not as powerful as solar, even the few µW they could provide are useful in the context of IoT devices. All of those solutions are again only practical if the power requirements remain low.

7.3 On-board processing

A smart IoT platform gives processing power and programming abilities that do not exist in traditional measuring equipment. While this can mean advanced machine learning algorithms running on-sensor, a challenge recently faced by TinyML (Doyu, Morabito, Höller, et al. 2020), it can also be useful to compute relatively simple statistics specifically tailored to corona applications. This again is especially relevant for long-term measurements, as it allows to decrease the data that needs to be transmitted by keeping only what is relevant in

a given context (Farhan et al. 2018); thus drastically decreasing the energy needs for wireless communication. Moreover, it can make important trends more obvious by enabling novel visualizations of the acquired signals as illustrated in chapter 11.

7.4 Discussion

Wireless communication, low energy needs, and on-board processing are all features that allow fulfilling particularly important requirements for large-scale deployment of long-term outdoor corona sensors. While these features are present in many realms of technology, they all fall under the same umbrella of the IoT. Additionally, IoT technologies have other fitting advantages, such as a lower cost relative to more traditional equipment, a wide availability of different parts and components, a rich and active ecosystem of development tools and documentation, as well as being a means to attract young talent who might otherwise not have discovered this field of study. Thus, the IoT enables a degree of monitoring and automation for corona experiments that would be difficult to reach otherwise, especially for smaller teams of researchers.

In a discipline of engineering such as high voltage engineering, measurement techniques are not merely an implementation detail and frequently constitute a significant part of the effort undertaken to make more fundamental scientific discoveries. IoT technologies can help make those efforts less laborious and as such are also being considered for other research topics such as the condition monitoring of switchgear as evidenced, for instance, by Franck et al. (2023).

Chapter 8

Implemented Corona Sensors

8.1 A unified sensor platform

The smart measurement system designed and implemented in this work needs to satisfy specific operating conditions. As discussed in chapter 7, IoT technologies allow on-potential measurements to be galvanically insulated from ground using wireless communication. Continuous long-term measurements benefit from low energy consumption and high reliability.

The many distinct corona related effects require heterogeneous sensors. Nevertheless, having a common modular platform increases the ease of use and facilitates development. The platform allows *sensor nodes* to be specifically tailored or extended for the quantity they will measure, while sharing a common communication stack to send the collected data to a central aggregator called the *gateway hub*.

The first three corona related quantities targeted by the platform are the corona loss current along the line, the ion current density at ground level, and the electric field strength at ground level.

8.2 Platform architecture

The proposed design is a modular device composed of a core system, a microcontroller supported by a Bluetooth Low Energy 4.2 module and a rich set of connected sensors. External circuitry targets the acquisition of specific physical parameters. Such an architecture enables to rapidly deploy a large number of different sensors. Having a single gateway hub recording data from multiple sensors that all use the same sensor nodes as a common platform is of huge benefit in the context of corona research. Corona on overhead lines manifests itself in different secondary quantities. Having the ability to simultaneously measure many of those corona effects over extended periods of time will help establish correlations that might not be visible when looking at single isolated effects.

The most important building blocks the platform are its so-called sensor nodes. Each node is based on STMicroelectronics' STWIN SensorTile development kit. The SensorTile uses an STMicroelectronics STM32L4R9, a 120 MHz ARM Cortex-M4 MCU with 2 MB of internal RAM. An STBC02 battery manager is included, together with a digital vibration sensor (IIS3DWB), 3D inertial measurement unit (ISM330DHCX), 3-axis magnetometer (IIS2MDC), digital absolute pressure sensor (LPS22HH), relative humidity and temperature sensor (HTS221) and two wideband MEMS microphones.

The sensing is either performed by these on-board sensors on the node itself, external PCBs called frontends, and/or more substantial pieces of external hardware depending on what is measured. Depending on the sensor, the signal is digitized either on the fronted PCB or using the MCU's internal ADCs. A 40-pin flex connector and a 12-pin female header on the SensorTile enable this modularity.

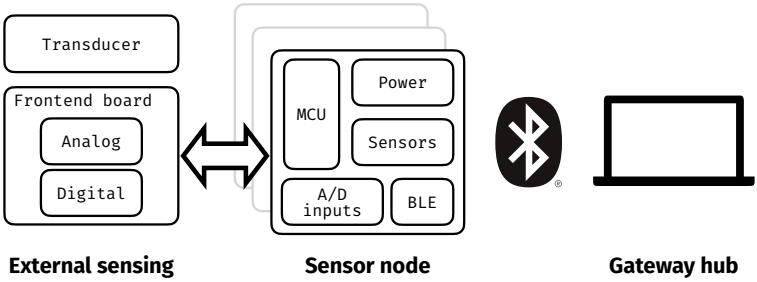

Figure 8.1: Schematic representation of the sensor platform architecture. Each node of the system is based on the STMicroelectronics' STWIN SensorTile. The nodes have internal sensors but can also be expanded by any combination of external sensing transducers and custom-made analogue and/or digital frontend PCBs. The physical link between nodes and external elements provides a programmable interface and auxiliary power. The node's MCU processes the data and sends it out wirelessly over BLE to the gateway hub that stores collected packets from one or several nodes in parallel.

8.3 Wireless data transmission

To monitor corona activity over extended periods of time, sensor nodes need to be low power but do not need a high data throughput. In corona experiments, the range over which data must be transmitted from the individual nodes to the gateway hub is dictated by the overhead line geometry and the width of the right of way and does not exceed a few tens of meters. These technical considerations combined with the availability, price and prior experience led to the choice of Bluetooth Low Energy to transfer data from nodes to the gateway hub.

On the node side, the SensorTile is equipped with a BlueNRG-M2 Bluetooth Low Energy 4.2 module. The firmware is based upon STMi-

croelectronics's example project `BLE_SampleApp` contained within the STSW-STWINKT01 firmware package. In the role of a peripheral the node advertises its characteristics and updates them with new data at predefined intervals.

The gateway hub is a standard workstation that uses Nordic Semiconductor's nRF52840 dongle as its Bluetooth Low Energy interface. The receiver software is written in Python and uses Thomas Gerstenberg's blatann and Nordic Semiconductor's pc-ble-driver-py libraries among others. One gateway hub can connect to several nodes, and subscribes to each node's Bluetooth characteristics.

The BLE connection was evaluated with multiple connected devices, up to 8, to check the real bandwidth supported by the gateway hub. The main parameter that affects the connection speed in a BLE star network is the connection interval, which should be scaled so that the nRF52840 can communicate with all devices once within a certain period. The default time window where the hub actively exchanges packets with a sensor node or peripheral in BLE parlance, corresponds to 7.5 ms. In that case, the optimal connection interval can be calculated for achieving the highest throughput. This corresponds to $(7.5\,\text{ms} \cdot n_{\text{peripherals}})$. To evaluate the BLE network throughput, the main focus is on the notification rate and the number of packets transmitted per connection event, considering packets with 20 B of payload. Results are reported in table 8.1, by varying the rate at which each peripheral is notifying the gateway, and the number of connected devices. In the worst case, with 8 connected peripherals, an average number of notifications per connection interval between 3 and 5 is measured, depending on the connection quality and peripheral-hub distance. Thus, in the worst case, the BLE network can support a throughput between 64 kbps and 106 kbps, while in the best scenario, with one device connected it reaches 150 kbps.

# Peripherals	Connection Interval	Notification Rate
1	7.5 ms	~ 1000 Hz
4	30 ms	200 Hz
8	60 ms	50 Hz

Table 8.1: Maximum notification rate supported vs. # peripherals

8.4 Corona loss current

As test lines are unloaded, the only current they carry is the so-called corona current, providing the energy for the discharges to happen. This current corresponds to the sum of all the losses caused by all the discharges happening along the line, and can be measured as the series current occurring between the high voltage source and the overhead line itself. In figure 2.3, this would be modelled by an ammeter placed on high potential right after the voltage source U_{HV} through which flows all the current the source provides to the line.

On a test line with the geometries in the order of those described in part II, corona currents are in the µA to mA range. Variations in HVDC corona levels during fair weather appear to be within a much smaller range than those observed during rain. This dictates the need for a sensor with a relatively large dynamic range or capable of dynamically switching input ranges. In hybrid setups, the DC corona current can sometimes not be distinguished from an AC component much larger than it. Here again, a high dynamic range is required to ensure that the signal is fully captured with a measurement accuracy such as to discriminate the corona current from the parasitic capacitive effects due to the electrode geometry (C_{geom}) discussed in section 2.4. This parasitic current can be filtered by analogue filters to some degree, but, especially for research purposes, it can be so high that it becomes infeasible to do so while capturing the variations in time of the signal of interest.

Recent research into corona current sensors have had an emphasis on

resolving individual discharge pulses and efforts where thus concentrated on reaching bandwidth ranging from MHz (Wang and Zhang 2008) to tenths of MHz (Yuan et al. 2012). Here on the other hand the sole interest is in the low frequency component of the corona current, which can be seen as the aggregation of all the discharges occurring along the entire overhead line. Since again all the current flowing through the conductor of a test line is due to corona, multiplying this current with the line voltage yields the corona loss power (Maruvada 2000).

For the reasons stated above, a specific front-end board with a differential current sense amplifier and a high resolution 24-bit ADC was designed. This corona current sensor is placed in series between the high voltage source and the line itself. The acquisition chain is composed of a fully differential analogue circuit designed to minimize noise, temperature dependencies, and component ageing. A cascade of two low-pass filters (LPF) is imposed before and after the differential amplifier. A passive first order and an active second order LPF respectively. The first amplification stage relies on the Texas Instruments INA186, a low power bidirectional, zero-drift, current-sense amplifier. It features a noise density of $75\,\mathrm{nV}/\sqrt{\mathrm{Hz}}$ and a rail-to-rail dynamic range. The signal is digitized by a 24-bit ADC (ADS122U04) and sent over UART to the STM32L4R9 via the 12-pin female header. The common ground of the fronted and the negative INA186 input are clamped through an ESD rated capacitor and a MΩ resistor. Moreover, all the input stages are protected up to 15 kV of ESD discharges.

The sensor is calibrated using a Keysight B2902A current source as a reference to supply a constant current. Three different configurations (table 8.2) are available depending on the required current range and precision. For the calibration of the three configurations a linear approximation is made to compensate for offset, gain, and temperature noise sources. Since each setting has a different current range due to the different shunt resistors, each combination was calibrated at different points for AC and DC.

Config	Shunt	Range	DC Precision	AC Precison
1	0.68 Ω	±24 mA	4.661 µA	16.54 µA
2	1.5 Ω	±10 mA	1.925 µA	7.940 µA
3	33 Ω	±0.5 mA	0.083 µA	1.310 µA

Table 8.2: Corona current sensor: configuration, range and precision for HVDC and HVAC

Every 4 seconds the sensor takes 100 measurements with a sampling frequency of 1000 S/s. Then, the sensor locally calculates the mean over 100 measurements. This mean value constitutes a single BLE packet sent every 4 seconds from the node to the gateway. The firmware flowchart given in figure 8.2 shows where low power states and error handling are supported. Each calibration was conducted for a time of 15 minutes, resulting in 225 received values, each representing the mean of over 100 current measurements. Moreover, the sensor was tested at different temperature points to quantify the temperature behaviour. With the Keysight B2902A the same current was generated as in the calibration process. The sensor was mounted inside a box and the same current was measured at three different temperatures. The battery stayed at room temperature. The front-end PCBs temperature sensor was used to track the sensor's temperature. The resulting curve was then normalized for calculating the correction factor.

As described in Table 8.2, the corona current sensor can measure within a range of ±24 mA with a precision down to 83 nA with a shunt resistor of 33 Ω (configuration 3). However, for HVAC measurements the maximum precision is decreased by a factor of 15×, reaching a value of 1.3 µA due to very crude methods used when detecting full AC cycles to compute RMS values.

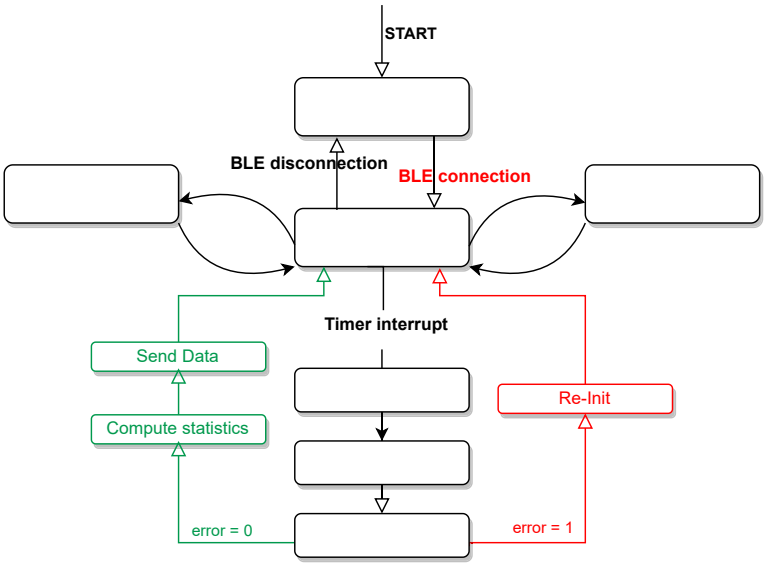

Figure 8.2: Firmware flowchart for the corona current sensor. *Stop0* indicates the lowest power consumption state, in which the node is completely off and not connected to the BLE. *Sleep* indicates a CPU inactivity, while the *Send Data* block includes the BLE transmission and the data serialization. The error handling includes the possibility to recover from software/hardware faults.

8.5 Ground level electric field

To measure the electric field at ground level below an HVDC overhead line, field meters using the field-induced charge principle of the "vibrating element" or "field mill" types are generally used (Comber, Kotter, and McKnight 1983; IEEE 1990; Maruvada, Dallaire, and Pedneault 1983). While other measurement principles such as MEMS sensors or optical sensors leveraging the Pockels effect are being investigated, they are not yet ideally suited for applications in a space charge rich environment or under hybrid AC/DC stresses, such as those of interest here (Cecelja, Bordovsky, and Balachandran 2002; Ma, Huang, et al. 2017; Yang et al. 2020).

Field mill devices developed by Prof. Yuan and his group at the Beihang University as described in (Cui et al. 2018) were used in this project. A feature of interest of those specific field mills is their claimed weather resistance. While a known technique to avoid water ingress into field mills during rain is to use them upside down (Comber and Johnson 1982), this is not always practical and might not be sufficient to operate non-weather sealed field mills outdoors for long periods of time. Additionally, it is ill-suited for measuring space charge altered electric fields since the path of moving space charges would be significantly altered at the point of measurement.

The output signal of the field mill is an analogue voltage that is directly measured by the node MCU's internal ADC. The signal is sampled at a relatively swift 10 kHz and 2000 points are acquired during each measurement. The mean, maximum and minimum values are processed on the MCU before being sent to the gateway every 2 seconds. The firmware is that of the ground level ion current with the management of the frontend omitted.

8.6 Ground level ion current

The ion current density at ground level is determined by measuring the current through a collecting plate electrode, slightly raised and

insulated from ground. Dividing this current by the plate surface yields the ion current density. This principle called the Wilson plate was originally developed for atmospheric currents (Chalmers 1962; Wilson 1908) and has since been widely used in corona research around HVDC overhead lines (Amano and Sunaga 1989; Bracken, Capon, and Montgomery 1978; Comber and Humphreys 1979; Fang et al. 2013; IEEE 1990). The currents are usually in the nA to low µA range and have historically been measured by electrometers (Amano and Sunaga 1989; Bracken, Capon, and Montgomery 1978; Comber and Humphreys 1979; IEEE 1990) due to the low voltage between the plate and ground. In recent years, current-to-voltage op amp techniques with low input burden voltage haven been used (Cui et al. 2018).

While Wilson plates have been used for several decades, in recent years, efforts have been made to acquire ion current data combining this principle with modern data transmission technologies such as Zigbee (Li, Yuan, et al. 2017).

The Wilson plates used here were previously developed by Heller (2016) and Pfeiffer (2017). They have a collecting surface area of $0.49\,\mathrm{m}^2$. A front-end sensor amplifies the small DC output current of the Wilson plate to a voltage which can be digitized by the internal ADC of the STM32L4R9. This is achieved by first dropping the output current over a shunt resistance R_{shunt}. Notably this resistance is adjustable by the user via on-board switches to account for different test line setups, allowing to read maximum input currents ranging from 3.5 nA to 0.5 mA. After being passively low-pass filtered the resulting voltage is amplified with the Maxim Integrated MAX4208, an ultra-low offset/drift, precision instrumentation amplifiers with REF buffer. By providing an offset voltage V_{offset} with the DAC of the STM32L4R9 the input range can be shifted to allow reading negative currents. To counter noise from the amplifier the signal is passed through a second passive low pass before outputted to the STWIN.

The firmware periodically starts a measurement sequence: First the

Config	R_{shunt}	V_{offset}	Current Range	Precision
C	4.59 kΩ	1.34 V	±1 µA	7.0 nA
D	232 Ω	1.34 V	±20 µA	69 nA
Y	2.560 kΩ	1.93 V	[-2.6, 1.0] µA	9.7 nA
Z	2.563 kΩ	0.375 V	[-0.50, 3.0] µA	10 nA

Table 8.3: Ground level ion current sensor: configuration, range and precision for HVDC

front-end sensor is powered on and then the ADC and DMA (direct memory access). After each DMA transfer statistics are computed from the just collected measurement block. Once the desired amount of measurement blocks is collected, the front-end sensor is turned off and the BLE characteristics are updated with the aggregated statistics. See figure 8.3 for the firmware flowchart.

Calibration is performed with the Keysight B2902A current source. For each configuration consisting of the tuple (R_{shunt}, V_{offset}) a linear approximation is made. Table 8.3 shows a selection of configurations. To account for changes on the STWIN side the ADC is calibrated at each power on of the front-end board and the analogue reference voltage is periodically measured.

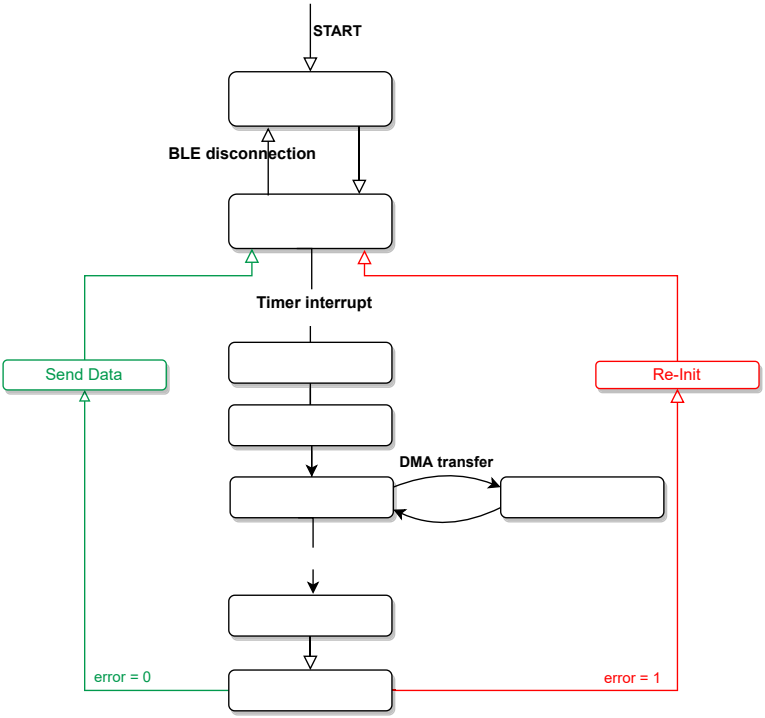

Figure 8.3: Firmware flowchart for the Wilson plate sensor. Error handling includes skipping of faulty measurement blocks or sequences, system reset after unrecoverable errors or too many faulty measurement blocks or sequences or warnings as well as logging to flash.

8.7 Power consumption characterization

A power consumption analysis of the platform is performed with a Keysight N6705C DC Power Analyser. The analysis is performed for the corona current sensor programmed with the firmware described in figure 8.2 and supplied with its nominal 3.3 V.

The general overview of the current consumption is presented in figure 8.4. In the *initial stage*, the platform is broadcasting and waiting for a BLE connection. In this part, the MCU runs in a normal running mode with BLE activated, which results in a relatively high power consumption of 133.5 mW on average. However, this mode is executed only at the first sensor node connection or after a hardware reset. Once the BLE connection is established, the sensor node transfers to the *idle stage*, where the MCU switches to the stop mode (deep low power state supported by the STM32L4 family) with all the sensors and the frontend powered off. In the *idle stage*, the power consumption of the MCU is 24.30 µW on average, in addition to the BLE module that needs 3 µW.

An internal low power timer wakes up the MCU from the stop mode every 4 seconds, which moves the STWIN from the *idle stage* to a *measuring stage*. As illustrated in Fig. 8.5, the *measuring stage* starts with powering on the frontend, followed by a 200 ms delay to fully activate the frontend, which consumes 29.11 mJ of power. Then a calibration of the external ADC and UART is performed, which consumes 25.83 mJ of energy in 141 ms. Another 100 ms delay is inserted for debugging, consuming 14.05 mJ of energy. Then, in the data acquisition stage, 100 data samples are acquired and processed at a sampling rate of 1000 Hz, costing 19.63 mJ of energy in 104 ms. After the acquisition is finished, the frontend and the UART communication are powered off. After that, the corona current data, as well as device information data of the platform including environmental information, battery status, etc, is transmitted via BLE. 5.92 mJ of energy is consumed in 36 ms. At last, the platform switches to the stop mode after a 200 ms delay.

Over 80 % of the energy in a working cycle is consumed in the calibration and acquisition stages. And a rather small part of the energy is used to transmit the data.

The valid duration of a working cycle is about 500 ms. Noted that the delay time for debugging purpose is not included. Assuming the duty cycle of the platform is D, then the energy consumption in one cycle 55.9 mJ can be had, and the power consumption in the idle stage is 27.3 µW.

In measurements, the duty cycle is 12.5 %. Then the energy consumption in one cycle is 55.9 mJ, which means 1270 hours of lifetime is expected from a 3.7 V / 4800 mAh battery. If the duty cycle is reduced to 1 %, which means one measurement in every 50 s, then the expected lifetime of the same battery increases to 15 500 hours. Thus, to maximize the lifespan of the platform, optimizing the duty cycle of the platform is a promising solution. Shortening the MCU running time (including data acquisition, processing, BLE event handling) is also an effective way to reduce the energy consumption in the valid working cycle.

As energy consumption and battery lifetime are critical issues for IoT sensor nodes, energy harvesting from the environment is an interesting option. Solar panels are the most common and established method, which particularly fit outdoor monitoring applications, for example in air-insulated substations. Taking the scenario of 1 % duty cycle as an example, the average power consumption of the platform is about 1 mW. Assuming the average daily sunlight time is 5 hours, then a solar panel with size 5 cm^2 combined with a battery storage system can fully provide the required energy consumption.

In any case, these performance metrics prove that this platform is well suited for long-term deployment. Additionally, its ease of use and low cost make it suitable to have large arrays of heterogeneous sensors working together without much overhead.

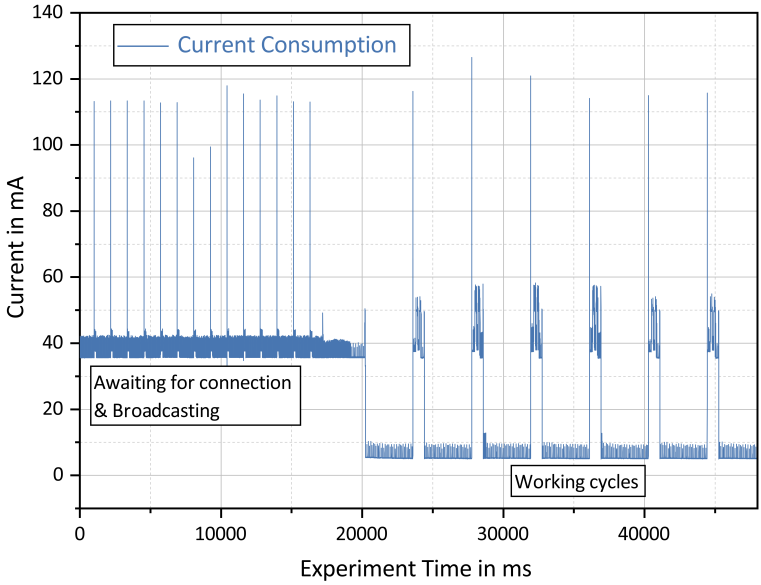

Figure 8.4: General view of the current consumption of the IoT platform.

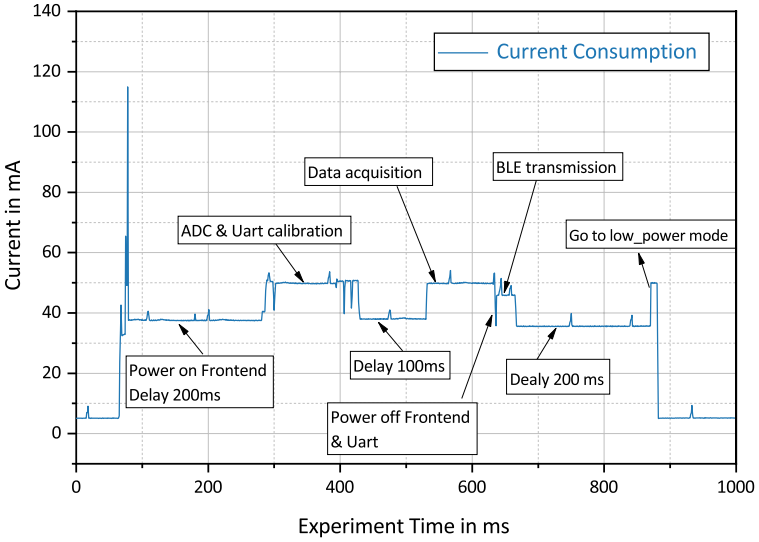

Figure 8.5: The current consumption of the IoT platform in one working cycle.

Part IV

Short-Term Experiments

Chapter 9

Single Droplets and Surface Wettability

9.1 Surface wettability

The wetting properties or wettability of a surface are a measure of how hydrophilic or hydrophobic a surface is. Wettability is quantified by the contact angle, which is the angle the droplet forms with the surface at the triple point with the surrounding gas, noted in purple in figure 9.1. The contact angle taken by a liquid droplet sitting on a flat surface (hereafter "a sessile droplet") at equilibrium is called the static contact angle and is denoted θ. The static contact angle is always between two values $\theta \in [\theta_r, \theta_a]$ which are the receding and advancing contact angles respectively. The receding and advancing contact angles manifest themselves for instance when the drop starts moving on a tilted surface or when it is grown or shrunk by a pipette. When the surface of an expanding droplet is "pushed out" it takes θ_a and contracting droplet takes θ_r. Similarly, as a surface is slowly tilted, a droplet will start moving when that surface reaches a certain angle. Of that moving droplet, the bottom angle is θ_a and the upper angle is θ_r. A fourth quantity is the contact angle hysteresis given as $\Delta\theta = \theta_a - \theta_r$.

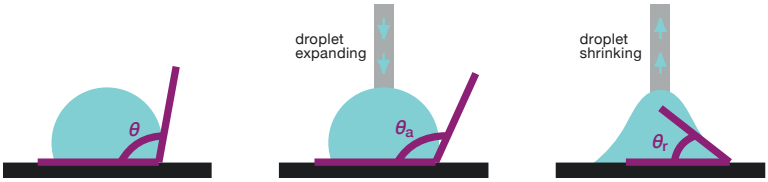

Figure 9.1: Illustration of the static, advancing and receding contact angles.The middle and right droplets are respectively expanding and shrinking due to water being injected in or sucked out of through a pipette. Adapted from (Vorwerk 2018).

This contact angle hysteresis can be seen as a measure of how slippery a surface is, as intuitively illustrated by the tilted surface mentioned above. The smaller the tilt required for a droplet to start moving, the more slippery it is and the smaller $\Delta\theta$ will be.

9.2 Droplets subjected to electric fields

The behaviour of liquids inside electric fields has been studied extensively in literature for a range of applications such as electrospinning of nanofibres (Li and Xia 2004), nano-printing (Galliker et al. 2012) and electro-hydro-dynamic spraying (Gañán-Calvo, Rebollo-Muñoz, and Montanero 2013; Jaworek and Krupa 1999). It has been shown experimentally and computationally that a droplet deposited on a surface deforms under the application of an electric field (Basaran and Scriven 1990; Glière, Roux, and Achard 2013). With increasing field strength the drop elongates and its surface eventually becomes unstable (Duft et al. 2003; Wang, Suo, and Zhao 2012; Zeleny 1917). Droplet deformation can locally enhance the electric field and lead to the onset of corona discharge (Higashiyama, Yanase, and Sugimoto 2002; Schultz, Pfeiffer, and Franck 2015; Xu, Zhang, Wang, et al. 2017). The shape droplets take when this instability is reached and a discharge is

initiated has been referred to as a Taylor cone in reference to Taylor (1964)'s pioneering work.

Even though a broad range of studies has focused on the deformation of droplets in electric fields before surface instability occurs (Basaran and Scriven 1990; Glière, Roux, and Achard 2013) only a limited number of works has investigated the correlation of water droplet deformation and discharge inception (Schultz, Pfeiffer, and Franck 2015; Xu, Zhang, Wang, et al. 2017). Furthermore, to the best of found knowledge, the effect of surface wettability on discharges from a droplet has not been explored both experimentally and computationally within the same study.

This chapter documents how surface wettability has a direct effect on the droplet deformation in an electric field as well as on the discharge inception. To validate experiments this dependence is theoretically predicted. In fact, the mechanism of discharge inception from a droplet strongly depends on its shape, formulated according to the wetting properties of the surface. Thus, by tailoring the surface wetting properties of a surface the inception of a discharge can be manipulated or controlled.

It has been observed that a droplet on a superhydrophobic surface, may lift-off when subjected to electrostatic forces. Those forces are smaller than those required for it to reach instability (Glière, Roux, and Achard 2013; Li, Li, et al. 2018; Traipattanakul, Tso, and Chao 2017). This chapter explains this phenomenon in more detail and investigates the conditions for it to occur without corona.

9.3 Effect of surface wetting behaviour on the inception of corona discharge

Using the setup described in section 6.1, three different surfaces are studied. The three copper-based surfaces are fabricated (more detail about their fabrication are given in (Stamatopoulos, Bleuler, et al. 2019) and its associated Supporting Information) with different wet-

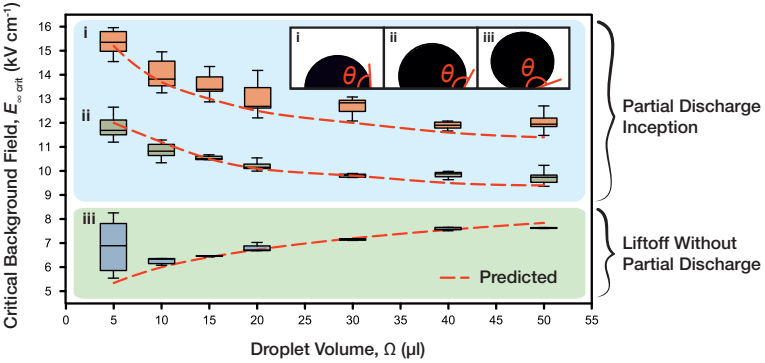

Figure 9.2: Box plot (central mark indicates median, rectangle between the 25th and 75th percentiles, and whiskers extend to the most extreme data points) showing the experimental critical field strength versus drop volume for either partial discharge inception or lift-off, for the (i) hydrophilic, (ii) hydrophobic and (iii) superhydrophobic surfaces. The red dashed lines are predictions computed using numerical models.

tabilities i.e. a hydrophilic, a hydrophobic and a superhydrophobic surface. Samples are tested in a vertical homogeneous electric field E_∞ created by two parallel horizontal electrodes. Drops of deionized water are deposited on a test sample placed at the lower electrode. The drops are thus sitting on the engineered surface samples. The upper electrode is grounded whereas a positive DC voltage is applied to the lower electrode. The present study's scope are sessile droplets in homogeneous electric fields.

After deposition, for $E_\infty = 0\,\mathrm{kVcm^{-1}}$ the droplets show an static contact angle $\theta \in [\theta_r, \theta_a]$ where θ_r and θ_a are the receding and advancing contact angles respectively. E_∞ is increased at a rate of $0.02\,\mathrm{kVcm^{-1}s^{-1}}$ and therefore the field can be considered quasi

static. Observations of the droplets with increasing E_∞ are made with a camera and simultaneously discharge activity and applied field strength are measured.

The applied electric field E_∞ causes a total collinear electrostatic force on the deposited drops resulting in their elongation (Taylor 1964; Wang, Suo, and Zhao 2012). E_∞ is increased until a critical value $E_{\infty,\mathrm{cr}}$ is reached; at this point either a partial discharge initiated at the tip of the Taylor cone formed by the droplet (Schultz, Pfeiffer, and Franck 2015) or a droplet lift-off (Traipattanakul, Tso, and Chao 2017) is observed. It should be noted that due to the homogeneity of the applied electric field, a partial discharge immediately leads to an electric breakdown. Therefore, in the presented experiments, both partial discharge inception field strength and breakdown field strength have the same value $E_{\infty,\mathrm{cr}}$.

The hydrophilic and hydrophobic surfaces are evaluated for droplet sizes (volume) Ω ranging from 5 µL to 50 µL (figure 9.2, (i) and (ii)). For each drop size, $E_{\infty,\mathrm{cr}}$ is higher for hydrophilic surfaces than it is for hydrophobic ones indicating that the more wettable a surface (i.e. the higher the static contact angle at $E_\infty = 0\,\mathrm{kVcm^{-1}}$), the stronger the electric field required to induce partial discharge. Moreover, for both cases $E_{\infty,\mathrm{cr}}$ decreases with droplet size, implying that the larger the droplet the weaker the electric field required to cause a partial discharge. In the superhydrophobic case (figure 9.2, (iii)) a different phenomenon is observed. An increase of E_∞ to a critical value $E_{\infty,\mathrm{cr}}$ leads to a lift-off of the droplet without any measurable partial discharge. This is attributed to the low contact angle hysteresis $\Delta\theta = 2.8°$ indicative of its high slippery behaviour. This enables the deforming droplet's contact disc to shrink to zero at which point the droplet leaves the substrate (Li, Li, et al. 2018; Roux and Achard 2009; Traipattanakul, Tso, and Chao 2017). It should be noted that the background field strength at lift-off $E_{\infty,\mathrm{cr}}$, increases with droplet volume. All the observations above are in agreement with the theoretical predictions presented below.

9.4 Prediction of discharge inception

To compare the experimental results with simulation predictions (figure 9.2, red lines) a model proposed by Glière, Roux, and Achard (2013) is used. It can compute the shape of drops deformed by an electric field. This model is based on an augmented Young-Laplace equation (Basaran and Scriven 1989; Myshkis et al. 1987; Roux, Achard, and Fouillet 2008) which gives the equilibrium shape of the drop surface accounting for buoyant, gravitational and electrostatic forces:

$$\gamma \nabla \cdot \mathbf{n} = -(\rho_{\text{water}} - \rho_{\text{air}}) g z + \Delta p + \frac{\varepsilon}{2} (\mathbf{E} \cdot \mathbf{n})^2, \tag{9.1}$$

where γ is the surface tension of water and $\nabla \cdot \mathbf{n}$ is the local mean curvature of the droplet's water/air interface which is the divergence of the unit vector $\mathbf{n}$ normal to the corresponding position. The term $-(\rho_{\text{water}} - \rho_{\text{air}}) g z$ is related to the net force of the buoyant and gravitational forces where ρ_{water} and ρ_{air} are the volumetric mass density of water and air respectively, g is the gravitational acceleration and z is the vertical distance from the bottom of the droplet. $\Delta p = p_{\text{water}}(0) - p_{\text{air}}(0)$ is the pressure difference between the drop and the surrounding air at $z = 0$. Finally, $\frac{\varepsilon}{2}(\mathbf{E} \cdot \mathbf{n})^2$ is the electrostatic pressure and is related to the electrostatic force, where $\mathbf{E}$ is the local electric vector field at the droplet's water/air interface and ε is the dielectric permittivity of air. The drop is assumed axisymmetric, of constant volume and the radius of its contact disc does not change with increasing E_∞. This constant contact disc is the mathematical expression of the non-stickiness of the hydrophobic and hydrophilic surfaces used here.

The applied electric field E_∞ can increase until the equilibrium expressed by equation (9.1) can no longer be fulfilled at every point of the droplet's shape for a set of constant volume and contact disc. At this point the computed droplet becomes unstable and fails to describe a physically possible shape (Basaran and Scriven 1989). As

shown later, this corresponds to the electric field right before the actual droplets reach an infinitely large curvature at the apex which leads to the onset of a partial discharge (Pfeiffer, Schultz, et al. 2016; Schultz, Pfeiffer, and Franck 2015; Taylor 1964; Xu, Zhang, Wang, et al. 2017). Therefore, $E_{\infty,\mathrm{cr}}$ is considered to coincide with the value of the applied electric field E_∞ at which the model exhibits numerical instabilities. Results show that there is a good agreement between experiments and predictions (figure 9.2c) for the hydrophobic and hydrophilic case and explicitly demonstrate the diminishing trend of $E_{\infty,\mathrm{cr}}$ with droplet size and static contact angle. Furthermore, it is worth noting that mean experimental and predicted values deviate by maximum 6 % which supports the validity of this prediction method for $E_{\infty,\mathrm{cr}}$.

9.5 Lift-off

For the superhydrophobic case the critical field $E_{\infty,\mathrm{cr}}$ is the value of the background field at which a droplet lifts off from the surface.

Here, a different and simpler model is used to estimate $E_{\infty,\mathrm{cr}}$. It is based on a force balance where the electrostatic force F_{el} resulting from the applied electric field, the buoyant force F_b,the gravitational force F_g, the force F_c due to interfacial interactions between surface and droplet and the force F_p due to Δp are considered (Glière, Roux, and Achard 2013). The overall force balance at the droplet is described by the following equation:

$$\underbrace{\rho_{\mathrm{water}}\Omega g}_{F_g} + \underbrace{2\pi r_{\mathrm{disc}}\sin(\theta)}_{F_c} = \underbrace{\rho_{\mathrm{air}}\Omega g}_{F_b} + \underbrace{\Delta p \pi r_{\mathrm{disc}}^2}_{F_p} + F_{\mathrm{el}} \tag{9.2}$$

F_{c} and F_{p} are considered negligible at the instant of lift-off since the radius of the contact disc r_{disc} shrinks to marginally larger than zero (Lebedev and Skal'skaya 1962; Roux, Achard, and Fouillet 2008). From this it can be derived that $E_{\infty,\mathrm{cr}}$ scales with $\Omega^{1/6}$ as demonstrated in appendix A.

This dependency is verified experimentally as shown in figure 9.2c where a good agreement is found with a maximum deviation that reaches 6% for $\Omega > 5\mu L$. However, for $\Omega = 5\mu L$ a large deviation of approximately 20% is observed. This is attributed to possible impurities of the tested surface that enhance F_c and to the small size of the droplets that render them more comparable to the scale of the impurities (contrary to the rest of the sizes investigated). As a result, higher applied electric field is required for a droplet to lift-off.

9.6 Effect of contact angle hysteresis

As mentioned previously, both the static contact angle and the contact angle hysteresis influence the partial discharge inception of a water drop on a surface. In fact, a droplet with a large static contact angle i.e. $\theta > 150^\circ$ and large contact angle hysteresis of $\Delta\theta = 10^\circ$, i.e. a rather sticky droplet, can show partial discharge instead of lift-off. Furthermore, based on the previous analysis, the aforementioned surface is expected to show a partial discharge onset at lower $E_{\infty,\mathrm{cr}}$ compared to the hydrophilic and hydrophobic cases. Practically, a surface that could exhibit such properties is an originally superhydrophobic surface that shows degradation (possibly due to oxidation) of the hydrophobic coating and/or local damage to its surface roughness. This degradation results in local pinning sites i.e. specific regions on the surface, where it will be less slippery and while still having a large static contact angle.

Figure 9.3 highlights the effect of the increased contact angle hysteresis on the inception of a partial discharge. Droplets of 40 µL are deposited on the superhydrophobic surface (figure 9.3a upper panel) and the same superhydrophobic surface after degradation (figure 9.3a lower panel). Under the absence of electric field both droplets have an static contact angle $\theta \approx 166^\circ$ (figure 9.3a, upper and lower panels). When an electric field is applied, both droplets deform into a prolate spheroidal shape causing a gradual decrease of the static contact angle θ. When $\theta < \theta_\mathrm{r} = 159^\circ$ the contact disc recedes (figure 9.3a,

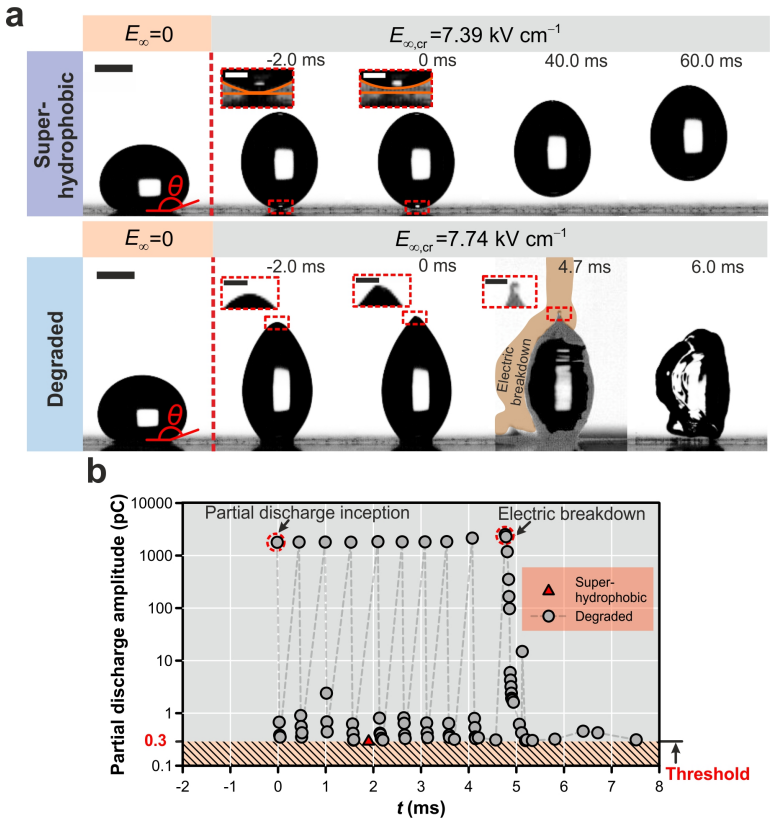

Figure 9.3: (a) High speed video frames of a 40 µL droplet on a originally superhydrophobic surface. For the top strip of images, the surface is intact and has its superhydrophobic properties. The droplet lifts-off at $t = 0$ and remains relatively round. On the bottom strip, the surface is degraded and stickier. The droplet does not lift-off and at a slightly higher background field than for the lift-off observed above, a discharge is initiated at the elongated droplet's tip. Scale bars correspond to 1 mm. (b) Partial discharge measurements for each of the two droplets shown above. The droplet lifting-off only has a single sample very slightly above the noise threshold of 0.3 pC that can still be considered noise. The coronating droplet on the other hand shows a train of pulses above 2000 pC starting as its shape becomes critical.

$t = -2$ ms, upper panel) until its area becomes marginally larger than zero (Korhonen et al. 2013). At this time instant (figure 9.3a, $t = 0$ ms, upper panel), given that the electrostatic force F_{el} is greater than the resultant of gravitational and buoyancy forces $F_g - F_b$, the droplet detaches from the surface (Glière, Roux, and Achard 2013; Roux and Achard 2009). After the droplet lifts off $F_{el} > F_g - F_b$ and the drop thus accelerates and reaches the top electrode (figure 9.3a, $t = 40$ ms, 60 ms, upper panel). It should be noted that prior to, during and after the droplet lift-off the partial discharge level (figure 9.3b) remains close to or below the background noise threshold of 0.3 pC. The drop thus lifts off without coronating.

However, after degradation the surface shows a different behaviour. While E_∞ increases to $E_{\infty,cr} = 7.74\,\mathrm{kV\,cm^{-1}}$, the droplet elongates and its contact line recedes until it reaches an area of higher wettability that prevents the contact disc from further shrinkage (figure 9.3a, $t = -2$ ms, lower panel). This is reflected to the static contact angle which at this instant is $\theta = 126°$, suggesting that $\theta_r < 126°$. Further deformation of the droplet gradually leads to a considerable increase of the apex's curvature (figure 9.3b, $t = -2$ ms, 0 ms, lower panel) resulting in the inception of a partial discharge with an amplitude of 1785 pC (figure 9.3b). After the inception of the discharge, a sequence of partial discharge pulses that coincide with oscillation of the droplet's apex is observed, finally leading to an electric breakdown that exhibits an amplitude of 2287 pC (figure 9.3b, $t = 4.7$ ms, lower panel).

This sequence of partial discharges is strongly correlated with the high curvature of the droplet's apex. During its oscillation, for each time that the apex reaches a maximum height accompanied by maximum increase of its curvature, a partial discharge pulse is observed. It is worth noting that the $E_{\infty,cr} = 7.74\,\mathrm{kV\,cm^{-1}}$ for the case of the degraded surface (on which a droplet is pinned), is even lower compared to that of the hydrophilic ($E_{\infty,cr} = 11.82\,\mathrm{kV\,cm^{-1}}$) and hydrophobic cases ($E_{\infty,cr} = 9.82\,\mathrm{kV\,cm^{-1}}$) for the same droplet size of 40 µL which is in agreement with the above analysis (i.e. increasing $E_{\infty,cr}$ with wettability).

9.7 Evolution of droplet shape with increasing electric field

To better understand the relationship between wettability and associated deviations of the partial discharge inception field strength $E_{\infty,\mathrm{cr}}$, the deformation of the droplet's shape is investigated for the entire range of subcritical applied electric field $E_\infty \leq E_{\infty,\mathrm{cr}}$ for the case of hydrophobic and hydrophilic surfaces. To this end, Gibbs free energy change $\Delta G = G - G_0$ of the droplet for a specific electric field E_∞ (where G and G_0 are the droplet's Gibbs free energy at E_∞ and for zero electric field, respectively) is used as an indicator of the droplet deformation (Michielsen et al. 2011; Schutzius et al. 2015; Yanashima et al. 2012). Since the contact disc of both surfaces remains unchanged, Gibbs free energy change of the droplet is expressed as

$$\Delta G = \gamma \Delta A \tag{9.3}$$

where $\Delta A = A - A_0$ is the difference between the droplet's lateral surface area for E_∞ and zero electric field.

Figure 9.4 shows the Gibbs free energy change of 10 µL droplets versus the applied electric field E_∞ for the hydrophilic and the hydrophobic surface. Up to $E_\infty \approx 6.5\,\mathrm{kVcm^{-1}}$ deposited droplets on both surfaces show negligible ΔG. However, for $E_\infty > 6.5\,\mathrm{kVcm^{-1}}$ the droplet on hydrophobic sample shows considerably higher ΔG than that on the hydrophilic surface. Alternatively, it means that for the same value of a droplet's ΔG, a stronger electric field is needed for the hydrophilic surface than the hydrophobic one suggesting that $E_{\infty,\mathrm{cr}}$ increases with wettability. In both cases whilst E_∞ reaches $E_{\infty,\mathrm{cr}}$, ΔG increases abruptly (Basaran and Scriven 1990; Reznik et al. 2004) indicating that deformation is accelerated at this phase. This abrupt increase is attributed to the mutual interaction between the deformed droplet and the applied electric field. The presence of the deformed droplet enhances the electric field around the apex which in return intensifies the electrostatic pressure at the droplet's interface. Further increase

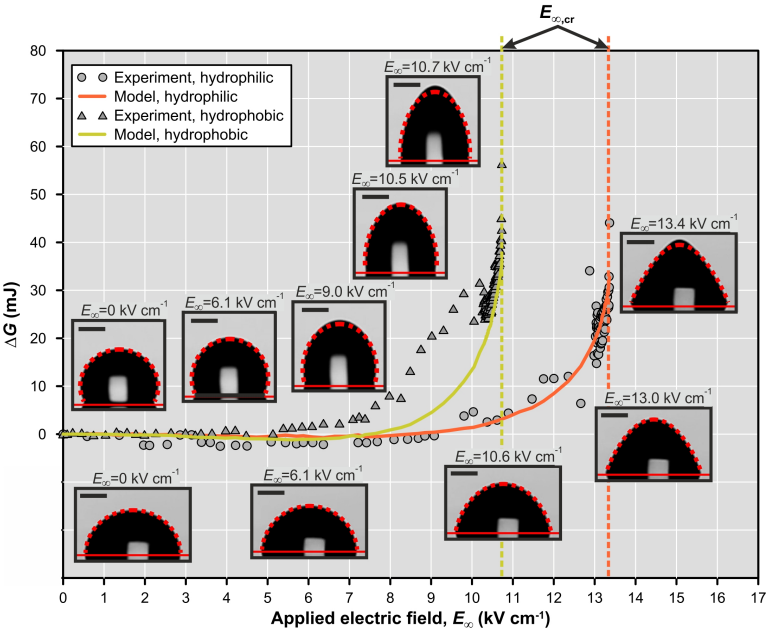

Figure 9.4: Evolution of drop shape with applied electric field for hydrophilic and hydrophobic surfaces. The Gibbs free energy change is used as a proxy measure for droplet deformation. Experimental data (circles, triangles and video frames) and results from the prediction model (orange and green plot lines, red contours on video frames) are compared. As field is increased and approaches the critical value $E_{\infty,\mathrm{cr}}$, the Gibbs free energy change grows asymptotically. Scale bars correspond to 1 mm.

of the droplet's electrostatic pressure results in further deformation of the droplet's shape and subsequently local enhancement of the electric field creating a positive feedback loop.

In addition, figure 9.4 shows experimental drop shapes with computed overlays obtained by the model described previously along with calculated Gibbs free energy change. For both surfaces, the predicted deformation is in relatively good agreement with that of the experiment. In the predicted ΔG versus E_∞ graphs, initially, the droplets show negligible deformation and shortly before $E_{\infty,\mathrm{cr}}$ an abrupt increase of ΔG. The good agreement of the critical values supports the above assertion that $E_{\infty,\mathrm{cr}}$ can be adequately predicted with the proposed method.

9.8 Local electric field and streamer criterion

Figure 9.5a shows drop shapes and the computed electric field in the surrounding air for a period of 9 ms before the critical event i.e. partial discharge inception or drop lift-off. The evolution of the droplet is observed with a high speed camera. The shapes of the droplet extracted from the videos are used to simulate the corresponding local electric field. The instant $t = 0\,\mathrm{ms}$ corresponds to the last recorded frame before partial discharge inception (hydrophobic and hydrophilic surfaces) or lift-off (superhydrophobic surface) occurs.

It is apparent that for both, the hydrophobic and hydrophilic surfaces, E around the apex considerably increases during those last 9 ms. The degree of inhomogeneity $E_{\max}/E_\infty$, where $E_{\max}$ is the maximum local electric field strength at the droplet's interface (which occurs at the apex), grows from 4.9 for the hydrophilic surface and 9.3 for the hydrophobic surface at $t = -9\,\mathrm{ms}$ to over 17 at $t = 0\,\mathrm{ms}$ for both cases. Even though both surfaces exhibit the same degree of inhomogeneity at $t = 0\,\mathrm{ms}$ the droplet on the hydrophilic surface is subjected to an electric field strength $E_\infty = 15\,\mathrm{kVcm^{-1}}$ which is approximately 1.4 times greater than that to which the droplet on the hydrophobic surface is exposed, i.e. $E_\infty = 10.6\,\mathrm{kVcm^{-1}}$. The drop on the superhy-

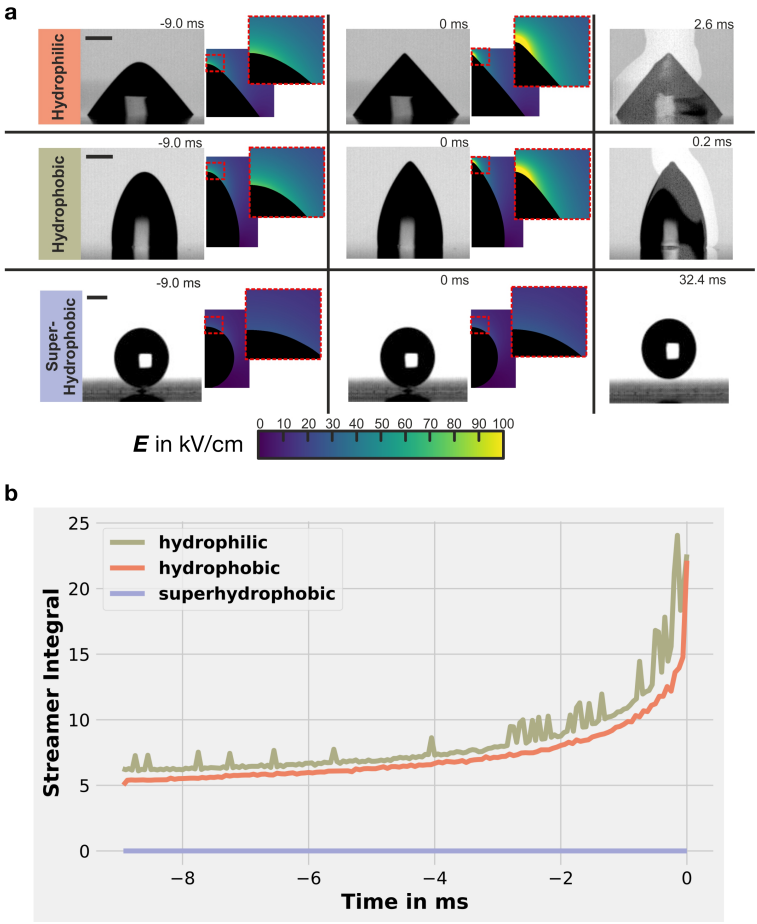

Figure 9.5: (a) Time lapses around the critical instant $t = 0$ for a 10 µL droplet on all three surfaces. High speed video frames are shown alongside FEM simulations of the local electric field strength around the extracted experimental drop shapes at the corresponding instants. Scale bars correspond to 1 mm. (b) Streamer criterion during the 9 ms preceding the critical instant for all three surfaces. The number of free charge carriers grows very rapidly a few instants before partial discharge inception for the hydrophilic and hydrophobic droplets, while it remains zero during the entire period for the superhydrophobic droplet lifting-off at instant $t = 0$.

drophobic surface during the last 9 ms before lift-off shows negligible deformation and the degree of inhomogeneity for this case remains constant at approximately 4 ($E_\infty = 6.1\,\mathrm{kVcm^{-1}}$).

Next, based on the computed electric fields for $t \in [-9\,\mathrm{ms}, 0\,\mathrm{ms}]$ the streamer integral (equation (2.2)) can be computed and the possibility of partial discharges in light of the streamer criterion (section 2.2) can be assessed. Figure 9.5b shows the streamer integral versus time during the instants preceding a discharge. For the case of hydrophilic and hydrophobic surfaces the streamer criterion is exceeded as the two curves pass 18 shortly before $t = 0$ leading to the discharge observed. This self-sustained discharge is generated when the apex of the droplet exhibits infinite curvature denoting that the shape deformation is a predominant factor that abruptly increases the number of free electrons in the avalanche.

It is particularly remarkable, that the streamer criterion is only exceeded within the last ms before partial discharge inception and that it coincides with the rapid change in drop shape observed previously in figure 9.4.

On the contrary, for the case of the superhydrophobic surface, the negligible deformation of the droplet causes minor distortion to the electric field and as a result $E_{\max}$ remains below $E_{\mathrm{crit,\,air}}$ causing the streamer integral to remain 0 and hence no discharge can occur.

9.9 Conclusions and outlook

This study demonstrates that surface wettability has a strong influence on the inception of electric discharges from water drops. Both the static contact angle and the contact angle hysteresis between the advancing and receding contact angle contribute to the onset of corona. The droplet size is also a factor.

In general, the higher the static contact angle of a pinned droplet and/or the larger the droplet, the lower the applied electric field required for discharge inception. This is true as long as the surface is

sticky enough, i.e. has a sufficiently high contact angle hysteresis.

On superhydrophobic surfaces (i.e. surfaces with both high static contact angles and low contact angle hysteresis) when a high enough field is applied, droplets lift-off without causing any partial discharge. This is attributed to the slipperiness of the surface.

Experimental data is supported by prediction models capable of accurately determining the critical field at which a droplet of a given volume and static contact angle will start to coronate, or lift-off from superhydrophobic surfaces.

To elucidate the mechanism that leads to the inception of discharges the evolution of a droplet's shape as deformed by an electric field is analysed experimentally and theoretically. It is shown that the more wettable the surface the smaller the droplet's deformation under the same applied field. Furthermore, it is observed that droplets exhibit an abrupt deformation as the field approaches corona onset. This abrupt deformation is the outcome of a positive feedback loop between the droplet's radius of curvature at the apex and the hyper local electric field both increasing due to the other until the streamer criterion is fulfilled when the droplet reaches the Taylor cone shape referenced in literature. For the droplets on superhydrophobic surfaces this interplay is weak and therefore does not lead to an abrupt local intensification of the electric field (as evidenced by the minimal changes in the local field observed in figure 9.5b).

The present study is limited to sessile droplets in homogeneous electric fields. The experimental setup used for it and described in section 6.1 has served as a basis for the further studies listed hereafter. Logical next steps that have been explored in student projects include impacting droplets (Vorwerk 2018), droplets in inhomogeneous fields (Keller, Kundert, and Tettamanti 2020) and hanging droplets (Reidy 2021). Some results were also published in (Stamatopoulos, Suter, and Franck 2022).

While single drop studies help in understanding fundamental interactions between water droplets and conductor surfaces, they only offer

a microscopic view compared to the macroscopic view needed to understand the behaviour of wetted overhead line. While different geometric configuration of the outer strands and their impact on corona performance have been studied in the past (Pfeiffer, Schultz, et al. 2016), more recently Kirchner and Franck (2022) have demonstrated how important a broader appreciation of wettability is to classify different conductors.

Chapter 10

HVDC PD Data during Weather Transitions

10.1 2D Histograms for partial discharge data

A common way to represent AC partial discharge (PD) measurement results are phase resolved PD plots (PRPDs). They are colour coded heat maps that indicate the incidence of discharges (z-axis or colour) of a given amplitude (y-axis) at a given instant of the AC power frequency cycle or phase (x-axis). They allow a visualization of phase dependency of corona discharges within the 50 or 60 Hz cycle.

The PD data needed to display a PRPD plot is generally captured over several periods, but the purpose is always to reflect a steady-state of the test object. When studying transient phenomena, like the corona behaviour of an AC overhead line during weather transitions, many PRPDs would need to be captured, each associated with a specific moment reflecting the evolution of the test object. A series of PRPDs snapshots taken at different points in time would need to be compared among each other to see patterns in corona characteristics as weather changes.

Furthermore, PRPDs obviously do not provide a satisfactory way of representing PD data for corona on DC overhead lines.

The difficulty to analyse transient corona behaviours and their impertinence in DC studies mean that PRPDs are not ideally suited to represent PD data of overhead lines. But by rethinking them slightly, a significantly more relevant representation method is conceivable.

In data visualization terms, PRPDs are 2D histograms where the occurrence of discharges is binned by amplitude on one axis and phase angle on the other axis. By simply changing the x-axis binning to absolute time intervals rather than phase angles, one obtains another kind of heat map. They show the number of occurrence of pulses of a certain amplitude within each time interval. Here the time intervals are not a repeating periodic window (that matches the AC voltage period or similar), but can be any arbitrary (but regular) subdivision of the entire time axis of a given measurement that can last hours, days or more.

The duration of the consecutive time intervals that form the x-axis should be chosen according to the time constants of the transient phenomena the test object is subjected to. For an overhead line subjected to weather transition, a reasonable timescale would be to observe the evolution of corona performance minute by minute.

In the heat maps of figures 10.1 to 10.3, each horizontal pixel column (x-axis, local time at the test site) thus represents a minute of time. Each vertical pixel line (y-axis, logarithmic, pulse amplitude in C) is a pulse amplitude bin, just like in a traditional PRPD plot. Lastly the colour (z-axis, logarithmic colour bar) indicates how many discharge pulses of that amplitude were recorded during that minute.

These heat maps have the advantage of providing richer information for each time interval compared to single averaged parameters such as the apparent charge or the average discharge current (IEC 2000). The patterns that shall be identified, such as for instance pulses of a higher amplitude becoming more frequent at a certain moment in time are clearly visible regardless of what happens with pulses of lower

amplitude. An average would hide the contribution of high versus low amplitude pulses. Nevertheless, the heat maps still also implicitly give a sense of more classical metrics such as average discharge amplitude and pulse frequency.

Moreover, sources of PD noise in a test measurement circuit that continuously emit discharge pulses of a given amplitude can more easily be identified and disregarded. In figures 10.1 to 10.3, a distinctive yellow line between 1 and 4 nC in amplitude is visible across all heat maps. This unwanted signal, probably caused by a suboptimal design of the high voltage rectifier circuit, can easily be discarded visually. In an aggregated value such as an average pule amplitude for each time stamp, it would significantly affect the results.

Despite this, the storage requirements for those heat maps remain low. They are extremely low compared to the full raw data from traditional PD measurement systems, and they are also lower than having to save PRPD snapshots at regular time intervals.

10.2 Presented outdoor HVDC PD measurement results

In sections 10.3 to 10.5 PD data of the outdoor HVDC test line in Däniken are presented using the data visualization technique described above.

As detailed in section 6.3, the Däniken test line is equipped to measure PD via coupling capacitor and a commercial Omicron MPD system. Over the course of a few days, several hours-long measurements were performed capturing different weather conditions. All the measurements presented here are for a line energized with a positive DC voltage of 350 kV corresponding to a field gradient of 23 kV/cm. The noise threshold of the recorded PD data is set to 150 pC.

To create the heat maps, the Omicron data is first exported using the “Export Matlab-compatible” feature which actually just creates binary files which can also be read for instance in Python as documented in

an application note of the manufacturer (Hoek 2017):

```
dt = np.dtype([('q', 'f4'), ('time', 'f8')])
data = np.fromfile(file, dtype=dt)
df = pd.DataFrame(data, columns=data.dtype.names)
```

The 2D histograms are then obtained with:

```
t_bin_size = 60 #x-axis bin size in seconds
plt.hist2d(df['time'], df['q'].abs())
```

and the two following `kwargs`:

```
norm=mpl.colors.LogNorm()
bins=[np.arange(np.floor(df['time'].min()),
      np.ceil(df['time'].max()), t_bin_size),
      np.logspace(np.log10(1.5e-10),
      np.log10(0.1e-7), 1000)]
```

In his student thesis, Lopez Raichs (2021) explored possibilities to automate parts of the process to facilitate longer measurements campaigns using MPD 600 systems and these heat map visualizations.

10.3 Wet weather transitions

Results

In the measurement shown in figure 10.1 top, the line starts wet from a night of rain. The rain has ceased by the time voltage is applied for the first time on that day. During the first 20 minutes a medium to high number of pulses rise in amplitude and draw a quarter circle bow-like-shape. After 12h30, as it starts raining again, this arc collapses and a very high number of low pulses start occurring. At the same time, a very small number of high pulses are visible until around 13h00 when all that remains (besides the horizontal line attributed to noise) are

a steady but high number of small to medium amplitude discharges. Around 14h05, as rain stops again, a trend similar to that from the beginning is visible where a medium number of pulses increasing in amplitude start to appear.

On another measurement day shown in figure 10.1 bottom, comparable rain onset, steady state and stopping phases as above were witnessed. The line starts wet again from prolonged exposure to rain prior to the measurement. As rain completely ceases around 12h30, pulses of increasing amplitude become more frequent and draw a distinct bow-like-shape (similar but lower shapes are visible between 11h40 and 12h40 as the rain intensity substantially diminishes). Around 13h40, rain starts again, and a very small number of high pulses become visible while the number of small discharges increases dramatically. 20 to 30 minutes after rain onset, the line is left with only frequent small pulses during the more intense rain period. Around 15h20, rain stops and the global amplitude of pulses increases again.

Discussion

Given the observations above, comparisons can be drawn to previous indoor experiments.

Pfeiffer, Schultz, et al. (2016) used an indoor setup with rain simulator to study rain onset, steady state rain and the drying behaviour on realistic conductors under DC energization. The corona current was shown to clearly increase after rain onset while the PD apparent charge decreased. Inversely, the corona current decreased during dry-off while the apparent charge strongly increased until the conductor was completely dry and no active corona sources were left. This behaviour was explained in detail based on a novel optical method described in (Schultz, Pfeiffer, and Franck 2015), with the number and size of water drops being a key for corona performance. While the corona current was observed to increase with the number of water drops and larger drop size allowing to form highly active Taylor cones (Taylor, Chartier, and Rice 1969), the partial discharge amplitude was

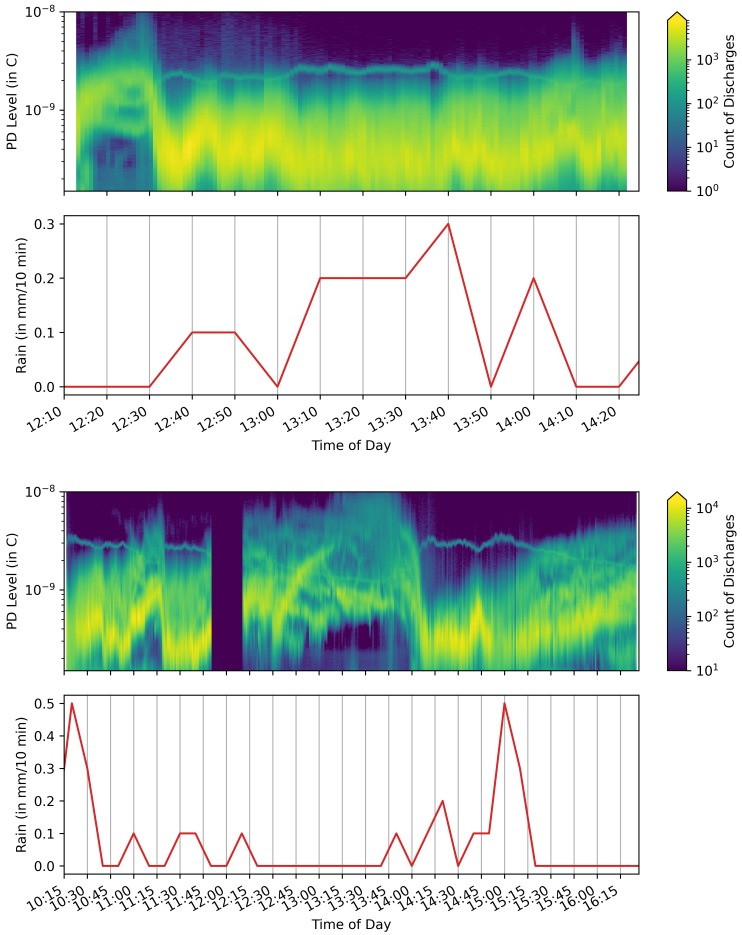

Figure 10.1: PD heatmap during rain transitions. (Top) The line is wet from rain reaching 3 mm/h during the morning in the 4 hours prior to this measurement. (Bottom) The line is wet from rain reaching 5 mm/h in the 5 hours prior to this measurement. Note that no data is provided from 11h50 to 12h10, as batteries of the PD measurement system had to be replaced. This was done without interrupting the energization of the line.

highest for the smallest number of drops. A possible explanation for this behaviour is the concept of “critical number of corona sources” introduced by EPRI (1993) wherein with a higher density of sources, e.g. after rain onset, neighbouring corona sources shield each other and thereby the maximum energy of the individual discharges is reduced, although the macroscopic corona current increases due to the higher number of discharges.

As shown by various researchers, the pulse amplitude of the individual corona discharges is very closely related to the level of audible noise and radio interference voltage (EPRI 1993; Li, Wang, et al. 2018; Trinh 1995). Therefore, Hedtke, Xu, et al. (2020) have investigated the change in audible noise and current pulse patterns during wet weather transitions. In accordance with the previously obtained trends (Pfeiffer, Schultz, et al. 2016), the audible noise strongly decreases during rain and rises again during dry-off, very similarly to the apparent charge. This change in audible noise was discussed in detail by Hedtke, Xu, et al. (2020) based on the observed pulse patterns and water drop distribution. In particular, the pulse patterns allowed to identify the different rain phases. At rain onset, there is a small number of high amplitude pulses and as the rain settles to steady state, those are replaced by very frequent pulses of low amplitude. As rain stops, the beginning of the drying is characterized by a medium frequency of pulses that rise in amplitude (Hedtke, Xu, et al. 2020).

The phases of rain transients for which distinct trends for the amplitude and frequency of discharge pulses were identified indoors with artificial rain, are also observed in the outdoor experiment under real rain presented in this chapter. As in (Hedtke, Xu, et al. 2020), a phase with very few high amplitude pulses right after rain onset is followed by a large number of low pulses during the rain steady state. As rain stops and the line starts drying, a medium number of discharges first appear with low amplitude and rise to higher amplitudes as time goes by. This drying behaviour manifests itself as characteristic quarter circle arcs on the heat map plots.

While the general trends observed for rain onset and drying are consistent with findings from the laboratory, some differences remain. For instance, in the present measurements, frequent pulses of low amplitude concurrent to the few but high pulses also seen indoors are observed, during the onset of rain. This can be attributed to the fact that in the laboratory rain onset always occurred as a step function, on a previously completely dried line and that the rain rate was kept constant from start to finish. On the outdoor measurements presented here, the lines are always wet from weather conditions prior to the experiment and the rain itself was variable. Of course, the controlled setup of the laboratory allows for different starting conditions to be set and the rain rate to be varied with a certain precision. On the other hand, outdoor setups due to the exposition to weather conditions other than solely the rain rate that will allow testing under even broader conditions that affect how the line gets wet and dries.

10.4 Transient behaviour with fog and dew

Results

On colder winter mornings, the region of the test site is often subjected to heavy fog. The measurement presented in figure 10.2 (top) was made on such a day. Before voltage is applied, the dew formed during the night has not dissipated. However, no precipitation of any kind was observed for that day, neither during the night nor for the day. At first, only low amplitude pulses are observed. Around 11h45 a bow-shaped trend of pulses increasing in amplitude begins; very reminiscent of the transient behaviour observed above as rain stopped.

On figure 10.2 (bottom), with a less dense fog, a similar transition trend can be seen, however, this time, the bow starts as soon as voltage is applied. After this initial phase, pulses of medium to high amplitude keep occurring with high to medium frequency respectively. This is a feature not visible in the measurement shown in figure 10.2 (top).

Looking at the meteorological data for figure 10.2 (top), the beginning

of the transient trend at 11h45 corresponds to when the relative humidity of air starts to drop below the 98 % to 100 % band it was in before.

Meanwhile, the measurement of figure 10.2 (bottom) starts when the relative humidity is already below 95 % and dropping. As the post transient pulses appear, the relative humidity is at 92 % or below, while it stays above 93 % for the remainder of the measurement in figure 10.2 (top).

It should be noted that compared to the measurements in rain, the absolute values of the total number of pulse per unit of time are an order of magnitude smaller, i.e. the colour bars have a different in figure 10.1 than they do in figures 10.2 to 10.3.

Discussion

A PD pulse trend very similar to that just described for drying after rain can also be observed when the line is wetted by dew rather than rain. The characteristic arc trend is as visible for dew as for rain. This trend has been attributed to the number of drops decreasing during dry-off, diminishing the shielding effect adjacent drops have on each other and thus allowing for pulses of higher amplitude. This is a phenomenon that should also prevail if the drops stem from humidity and condensation rather than rain precipitation.

Another interesting fact observed in figure 10.2 is the correlation pointed to with the relative humidity of the surrounding air and the moment this drying transient occurs. Although there are not enough measurements to draw conclusions, it could be that the relative humidity needs to drop below a critical value (here around 95 %) for the drying to start. This value would probably be different for a real overhead line as the conductors are not heated by any current in this experiment.

Humidity as an influencing factor for corona discharges has been a widely explored topic in literature. In addition to rain corona and the

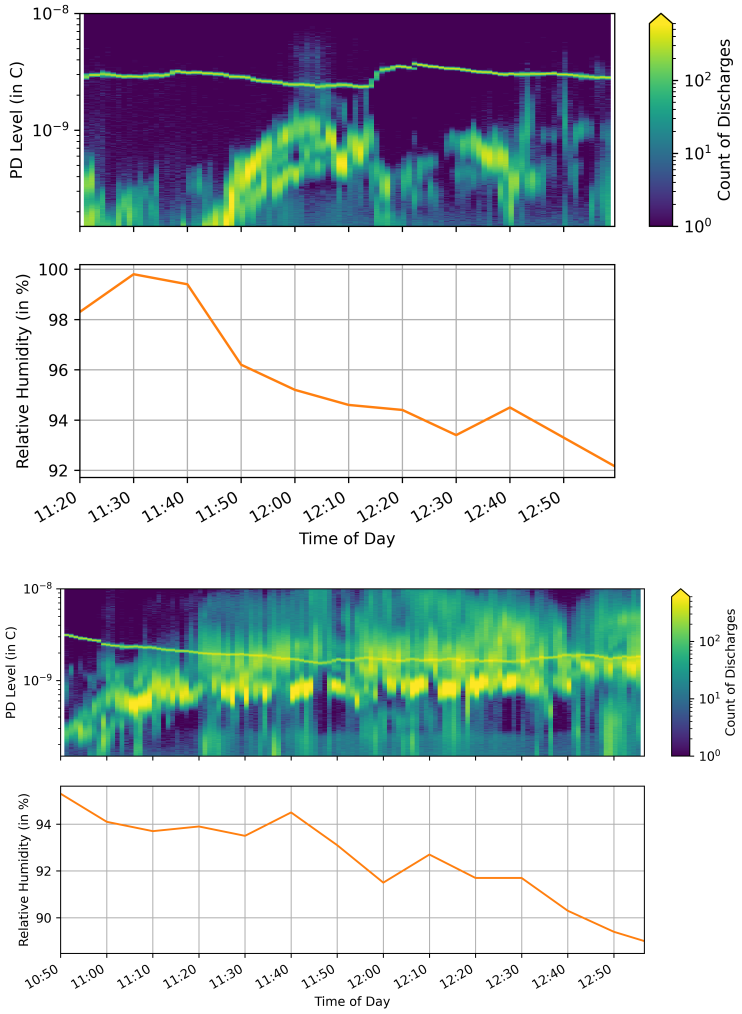

Figure 10.2: PD heatmap during fog dissipation after a night of saturated humidity.

related transients, other researchers have also observed a change in corona performance with dew and humidity. As humidity increases corona losses were observed to increase in outdoor tests (Anderson, Baretsky, and MacCarthy 1966; Comber and Johnson 1982). In a controlled indoor environment, Xu, Zhang, Chen, et al. (2016) and Xu, Zhang, He, et al. (2015) have shown that the pulse amplitude also depends on humidity. For higher humidity values, the pulse amplitude was found to increase for negative voltages (Xu, Zhang, He, et al. 2015) and to decrease for positive voltages (Xu, Zhang, Chen, et al. 2016) confirming results from Hu et al. (2014).

When corona is caused by water droplets on the conductor surface, humidity has at least two mechanisms through which to act. One is the humidity of the ambient air i.e. that of the discharge media itself that thus changes the conditions of the partial discharges. The other is the role humidity plays in different qualities of the droplets themselves, notably their number and overall distribution along the conductor, their size and their ability to deform on the conductor surface (as discussed in chapter 9), as well as possible condensation processes.

10.5 Fair weather corona and humidity

Results

Figure 10.3 shows two measurements made on a completely dry day. No fog or precipitations were observed neither was the line wet by previous weather. From 13h10 to 13h50, the relative humidity in the air is between 80 % and 85 %. The line exhibits a medium to high number of pulses of all amplitudes, although with a bias towards higher amplitude pulses. From 17h20 to 17h45, while humidity is back up between 94 % and 96 % the number of high amplitude pulses is generally lower, but the number of low amplitude pulses is high.

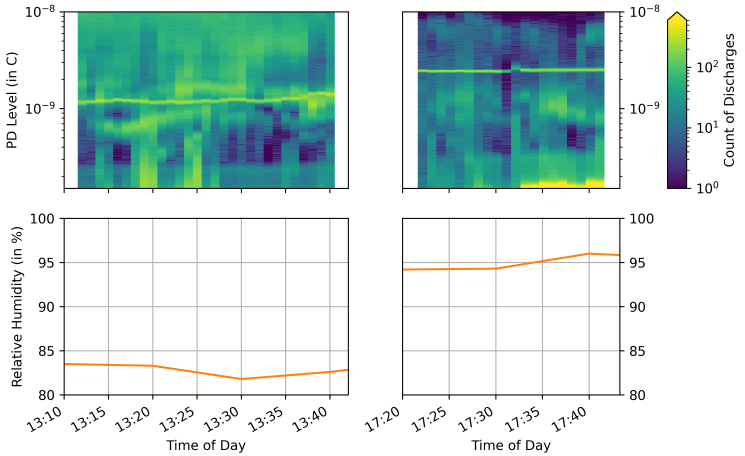

Figure 10.3: PD heatmap during a dry, fair weather day.

Discussion

Figure 10.3 indicates that even in dry conditions, different corona behaviours seem to be attributable to changes in ambient humidity. After the drying phase observed in figure 10.2, corona activity also does not stop completely. While in dry cases the total number of discharges is significantly reduced compared to the wet cases, the amplitudes are generally more dispersed. This could be characteristic of the nature of discharge sources which are not water droplets but rather scratches or other protruding particles on the conductor surface.

10.6 Conclusions

The data visualization method introduced in this chapter allows correlating atmospheric conditions with visible patterns in PD behaviour.

Indeed, many characteristic trends appear as a number of discharges of a given amplitude evolving through time.

Acquiring a significantly larger dataset of those 2D histograms would allow for a more accurate classification of the different PD trends observed. Despite the huge amount of data generated when capturing PD data, these histograms make long-term acquisition feasible.

That said, this visualization method still relies on traditional PD measurements. While PD measurements can give insights into important corona characteristics such as discharge modes, they are also burdened, and ultimately limited in their practicality, by the apparatus they require. Part V of this thesis introduces a second kind of visualization that also permits the analysis of long-term trends without hiding away the variability inherent in corona data.

Chapter 11

Representation of Highly Dynamic Signals

11.1 Smart sensor features

In this chapter, an example outdoor measurement is discussed to illustrate possibilities offered by the smart features of the unified sensor platform introduced in part III. Indeed, the on-board processing capabilities of the platform allow complete freedom and control over the way the raw signal gets treated before being transmitted to the gateway hub. As such, signal representations that are better suited to the nature of the signal and the kind of analysis a measurement is intended for are easily achievable.

Figure 11.1 shows over 4 hours of an ion current at ground level measurement made with the Wilson plate sensor using the rooftop setup from chapter 5.

The sensor samples data at a frequency $f_s = 250\,\mathrm{S/s}$. When performing long-term measurements to observe how the ion current is related to weather phenomena (which have time constants in the order of minutes), it wouldn't be practical to continuously record, transmit and

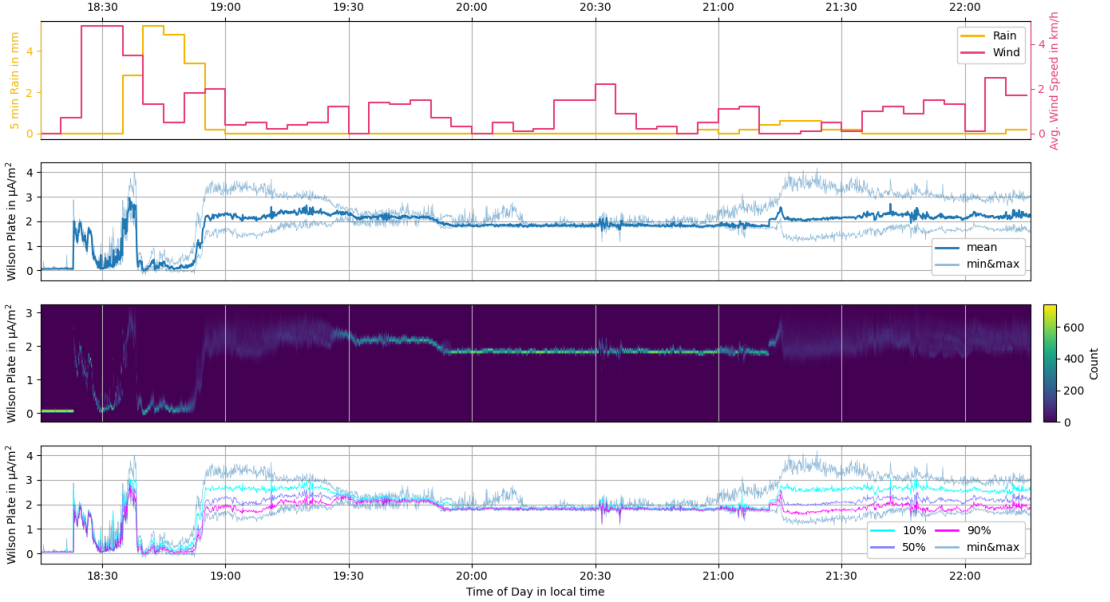

Figure 11.1: Weather data along with three different statistics representing the same ion current data as computed and sent out by one of the sensor nodes. The weather data shows rain precipitation in mm/h and the average wind speed in km/h with a 5 minutes resolution. The second plot shows the minimum mean and maximum of the signal. The third figure shows a 2D histogram of the data with fixed bins. The bottom plot shows quantiles of the measured data along the minimum and maximum.

store data at this rate, neither from an energy consumption nor from a data handling and analysis perspective, especially with the perspective of deploying many sensors for long-term measurements.

Thus, ten times per minute the sensor records data during a sampling interval of $T_{\mathrm{SI}} = 3\,\mathrm{s}$ (still at $f_s = 250\,\mathrm{S/s}$), processes those raw samples and sends out a statistic describing the sampling interval. Deciding on what statistic to transmit instead of the raw data of every single sample is a balancing act between data throughput, energy consumption and storage on one hand and the scientific value of the collected data on the other hand. The bottom three plots in figure 11.1, show different kinds of statistics displayed as sent by the sensor node without further post-processing.

11.2 Example measurement

In the first plot below the weather data, the mean of the measured signal is the dark blue line, while the lighter blue lines, show the extent of the minimum and maximum measured value within a given sampling interval T_{SI}.

The next figure shows a 2D histogram of the ground level ion current density during the same time period. Each horizontal bin is a sampling interval T_{SI} and there are 50 vertical bins covering the range shown on the y-axis (the entire measurement range of the sensor is not shown here for clarity). The colour indicates how many samples (count) of a given amplitude (y-axis) where captured within each sampling interval (x-axis). This representation is somewhat similar in idea to what was introduced in chapter 10 to look at HVDC partial discharge data over long periods of time, but here, every column of pixels always adds up to 750 samples ($T_{\mathrm{SI}} \cdot f_s$) rather than the total number of PD discharges for each specific time interval.

The bottom plot shows different quantiles of all samples measured within each single sampling interval T_{SI}. Specifically the median of the data as the 50 % quantile, the 10 % quantile (the lines above which

lie 10 % of the data points from a sampling interval or reciprocally below which lie 90 % of the data) and the 90 % quantile. Additionally, the minimum and maximum are shown as in the top plot, to indicate the full range within which samples were measured.

The statistic required for the top plot are just the minimum, the mean, and the maximum of each sampling interval T_{SI}, i.e. 3 float numbers have to be sent per interval. The middle image requires 50 integers per sampling interval T_{SI} while the lower plot requires 5 floats for the quantiles, the minimum and the maximum.

Firstly, looking at the top plot, it is obvious, that transmitting only the mean value of every sampling interval T_{SI} would not be sufficient to faithfully represent the signal. Indeed, for instance, while considering only the dark blue line between 20:15 and 20:30 and 21:00 and 21:15, one might be under the impression that the signal is very similar for both time intervals. The minimum and maximum lines already allow us to observe that the signal must have been much more dynamic during the second time interval than the first. They suggest that there are peaks of ion current occurring within each sampling interval T_{SI} after 21:00. The maximum line deviating from the mean happens to correspond with rain activity picking up again at 21:00 after a 2 hour pause. What remains impossible to tell, is whether the peaks are sharp and isolated or broader and/or more frequent while allowing the mean to remain relatively constant.

A representation such as that in the middle figure allows to easily see if values are indeed concentrated around the mean the entire time during 19:30 and 21:15 with only very occasional excursions towards extreme values. Between 18:15 and 19:30 or after 21:15 on the contrary, the values are spread around the entire range between the minimum and maximum recorded values for the given sampling intervals T_{SI}. As rain sets in around 21:00 and the maximum value starts diverging from the mean value, the heatmap confirms that it is only 15 minutes later, starting at 21:15, that the spread in sampled data points within a sampling interval T_{SI} becomes significant. After that time, the middle

figure becomes more difficult to read.

Here, the bottom plot provides deeper insights than the other plots could. For instance, between 21:15 and 22:00, the maximum plot line decreases steadily, but the 10 % line remains relatively flat indicating that 90 % of the data points remain under a fixed threshold. During the same time period it is also notable that the spacing between the quantiles is relatively large and becomes narrower as time passes by, starting around 21:45. While the maximum values seem to start decreasing as soon as rain ceases, the narrowing of the quantiles seems to happen later during the drying of the overhead line. Long-term measurement campaigns aim to establish that kind of correlations in order to better describe the corona behaviour of overhead lines under varying weather conditions.

11.3 Conclusions

The results displayed in figure 11.1 are merely examples of possible data representation taking advantage of the processing capabilities of a smart sensor platform such as the one introduced in part III. Nevertheless, it serves to show how highly dynamic ion current at ground level flowing through a Wilson plate can be.

While some patterns have been identified above, in order to decide what data acquisition parameters (sampling frequency, duty cycle etc.) and representation (statistic, visualization), further results are still needed before making definitive conclusions about what would be best in the context of long-term measurement campaigns.

Also, the possibility to add more Wilson plates to an experiment and to complement ion current at ground level measurements with other corona related quantities is discussed to some extent in chapter 12.

Chapter 12

Benchmarking the Sensor Platform

The sensor platform introduced in part III is a unified sensor platform in that heterogeneous sensors sharing the same sensor node transmit their data to a single gateway hub. The ability to concurrently measure different corona effects on a single line with the developed sensors is demonstrated here.

In this chapter, an example measurement comparing different overhead line conductors' corona performance during a wet weather transition is presented. The corona loss current, the electric field at ground level and the ground level ion current through a Wilson plate are measured each with one sensor node connected to the same gateway hub. The examined conductors differ in their surface properties, not limited to a single contact angle describing their wettability but also other features such as their droplet distribution on the surface as discussed in more detail by Kirchner and Franck (2022). The measurement was conducted in the E31 laboratory mentioned in section 6.2.

12.1 Measurement results

Figure 12.1 shows the simultaneous progression over time of the signals from all three sensors from the platform. Here a new conductor (darker coloured plot lines) and an aged conductor (lighter coloured plot lines) are compared. Both are common European conductors without any special treatment, but the aged one has a significantly more hydrophilic surface, in the more generic sense discussed in previous literature (Straumann and Weber 2010).

Both conductors tested have a diameter of 22.4 mm, which energized at 185 kV DC yields an electric field gradient of 27.25 kV/cm at the conductor surface.

The corona current is shown in blue at the top, the electric field at ground level as measured by the field mill in orange and the ion current density at ground level through the Wilson plate in green at the bottom. While the corona current is measured for the entire length of the conductor, the electric field and ion current density measurements are localized to where the respective sensors are placed. As the corona discharges influence the electromagnetic environment not only right below the line, but along the entire right of way corridor (a few meters wide and parallel to the line) as well, both sensors are placed 2.5 m off the axis of the conductor.

Before the line is energized, all sensors show 0. As voltage is applied, the space charge free electrostatic field (Laplace field) rises to the same value of around 17 kV/m for both conductors (figure 12.1 instants A to B). Here, the setup does not exhibit dry corona as shown by the corona current and ion current at ground level remaining null. While rain is applied on the line at the same rain rate of approximately 4 mm/h for both conductors (instants B to C) all three quantities first raise very rapidly, then more slowly towards a wet steady state that is reached after around 15 minutes after rain start. It is now obvious, that the new conductor produces significantly more corona than the aged one when wet.

Some of the water droplets from the falling rain act as corona sources. Those corona sources cause an ion current that can be measured as the total corona current flowing through the line or an ion current density at ground level through the area of the Wilson plate. Moreover, the presence of free charge carriers in the air between the line and ground modify the electric field, adding a Poisson field component to the Laplace field the field mill measured between times A and B.

As rain ceases (instant C) both conductors start to dry and corona levels decrease. The way in which both conductors dry show significant differences as well. Shortly before instant D, the rate at which corona activity decreases on the new conductor accelerates again, before completely drying out. The aged conductor will go on at the more or less constant level of corona activity for over 5 more hours before drying out. This phase is not shown here for clarity. It should be noted that acoustic emissions from the lines were audible whenever the corona current was above zero.

The lower corona current measured for the aged conductor during the wet state (instants B to C) can be explained by the lower number of water droplets on the surface. Thus, fewer discharges occur compared to the new conductor. The aged conductor also shows a clear difference in the drying behaviour (instants C to D). Due to the strong hydrophilic properties of the surface, a water film is formed. This "feeds" the few coronating water droplets long after the rain stops. For this reason, the drying phase is much longer for the aged conductor than for the new one without the hydrophilic properties.

At the 12 minutes mark, a small peak of dry corona (probably a dust particle on the line) is visible for the new conductor measurements of the corona current and the electric field but not for the Wilson plate. This is a consequence of the localized nature of the bottom two sensors. Again, the corona current is measured for the discharges happening along the entire line, while the ion current density and field enhancements caused by space charges are localized.

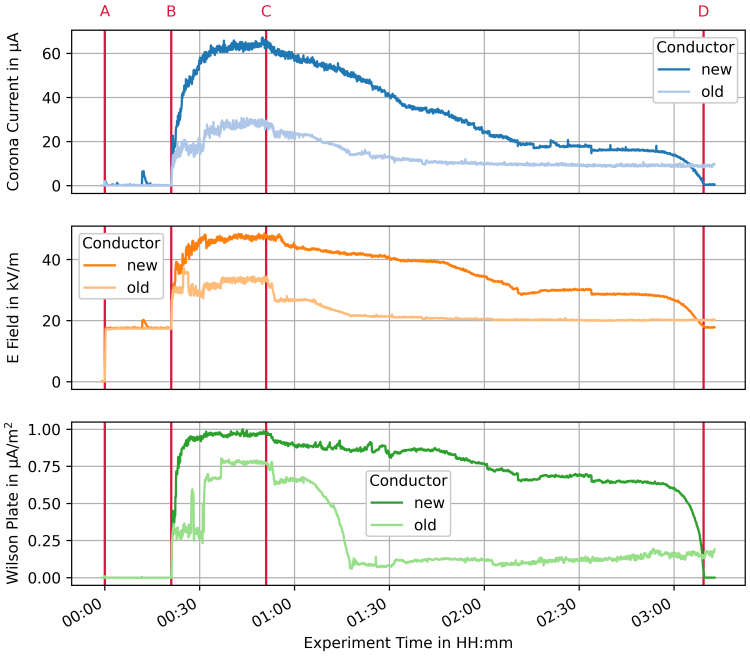

Figure 12.1: Two measurements showing the corona behaviour of two different conductors in corresponding fair weather, rain, and drying phases. The vertical lines respectively show the time instants when (A) the originally dry and grounded line was energized to 185 kV, (B) rain started pouring on the line, (C) rain ceased and (D) the aged conductor was fully dry again. The darker coloured plot lines are from a new conductor, the lighter ones from an aged conductor.

12.2 Conclusions

The measurement above demonstrates that despite their comparatively low cost, the sensors used are more than adequate to very clearly discriminate the two conductors based on their corona performance.

Of course, here, only one of each ground based sensor was used. Ideally the ground based values should be measured at several points on an axis perpendicular to the line, allowing to determine a section profile of ion current or electric field values. This was done in the past by such authors as Comber and Johnson (1982) or even in Däniken (Hedtke, Pfeiffer, Gobeli, et al. 2018) but using a different much less precise and reliable acquisition method than the sensors used here.

The low cost and high precision of the sensors introduced in part III make it imaginable to not have just one line of Wilson plates perpendicular to the line but several parallel series of sensors on several axes perpendicular to the line along the line's length. This would help "dilute" sources of measurement noise such as the small peak alluded to above caused by a localized corona source that can significantly alter ground based corona effect values when measurements are taken at a single position along the conductor thus not reflecting the overall behaviour of a line.

This measurement also nicely illustrates the complementarity of sensors measuring different corona effects.

Finally, this example highlights the importance of taking the drying phase into account when assessing the corona performance of an overhead line. Drying phases of HVDC overhead lines will be discussed more thoroughly in section 15.3.

Part V

Long-Term Measurement

Chapter 13

Introduction to Rooftop Experiment Results

13.1 Long-term energization

By far the longest almost continuous line energization that occurred during the duration of this thesis happened on the rooftop setup presented in chapter 5.

Figure 13.1 gives and overview of the energizations during the year 2022 along with cumulative rain during the year. The time periods with a background colour shading are those where the line was energized with a positive or negative voltage for the red and blue areas respectively. The voltage was always set to either ±60 kV. The white areas indicate the times when the line was not energized, mainly for testing new sensors and for maintenance, hence the "almost" continuous energization.

During its commissioning phase in early 2022, there were many short energizations, until the longer energization blocks occurred under positive polarity from mid-February to early May. The line has been almost continuously energized with a negative voltage during more

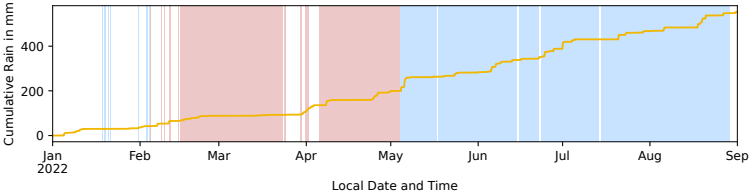

Figure 13.1: Line energization periods during the year 2022 coloured by polarity; positive in red and negative in blue. The cumulative rain over the time span is indicated by a yellow line.

than 4 months starting in early May 2022.

Despite a remarkably hot and dry summer all over Europe, the cumulative rain curve shows that the line experienced a fair share of dry and wet periods.

Over 60 rain events of varying intensities and duration were observed as discussed in more details below.

13.2 Corona data presented

The corona related quantities measured on the rooftop setup have included traditional partial discharge measurements as well as ground level electric field and ion currents using the IoT platform presented earlier. The corona current was also measured using both the ammeter in the high voltage source and the on-potential device from the IoT platform.

The current as measured by the source has the advantage of having been always recorded whenever the source was energized. This is not the case for any of the IoT sensors or the partial discharge measurement. The high voltage source measured corona current is thus the quantity that constitutes the largest dataset and is therefore the long-

term corona quantity studied in this work.

It has been reported that a larger number of insects and particles tend to be deposited on positive rather than negative poles (EPRI 1993, p. 3-12). The number of airborne corona sources depends on conductor gradient and, at high gradients comparable to those of the line studied here, this difference between polarity can amount to up 6 to 8 times (EPRI 1993, p. 3-13). Nevertheless, as the crude distributions shown in figure 13.2 show, the observed values tended to be an order of magnitude smaller under positive polarity than they were under negative. Higher corona losses for negative compared to positive poles have been reported for instance in (Morris and Rakoshdas 1964), while Maruvada, Trinh, et al. (1981) find this to be true only for fair weather during the winter. All the results cited above are from North America, and it is not known to what extent they can be generalized to the Swiss urban environment. In the experiment presented here, the polarity was set to stay negative after May 2022.

The dataset analysed hereafter always refers to the negative polarity data captured since May. It means that the dataset spans three seasons, namely spring, summer and fall. It should thus cover the times of the year when airborne sources suspected to impact fair weather corona performance are more numerous (EPRI 1993, p. 3-9).

As long as the line voltage stays constant, reporting corona losses or corona currents is equivalent up to a factor ($P_{\text{corona}} = U \cdot I_{\text{corona}}$). In literature, it is more common to see corona currents reported as power losses rather than currents. They can be presented as a raw power, such as in (Yu et al. 2019), power per unit length of line such as in (Bailey 1967; LaForest et al. 1963) or in dB above a power level per unit length (Corbellini and Pelacchi 1996; Hirsch and Schafer 1969; Maruvada, Trinh, et al. 1981). Corona currents are nevertheless sometimes reported directly as currents such as in (EPRI 1993, Ch. 3). In this reduced geometry setup, reporting corona losses, even per unit length would be relatively meaningless since a comparison with real lines would still not be possible. Rather than absolute numbers it is

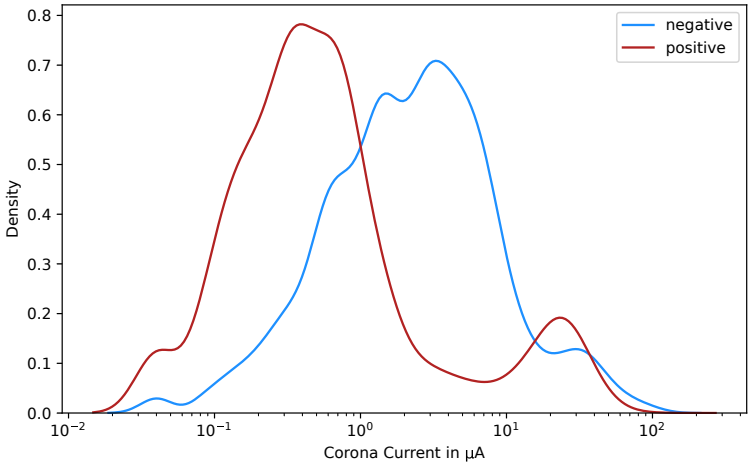

Figure 13.2: Crude kernel density estimates of corona currents under both negative and positive polarity. The aim of this figure is to give a general qualitative sense of the data distribution and thus the bandwidth is selected to be large, and the curves extend beyond extreme data points.

trends shown by the corona current over time that are of interest here. Corona currents will thus directly be reported and for the sake of simplicity always as positive values.

13.3 Source current and line current

Most, but not all the time, the current was also measured by one of the IoT sensor presented in part III. The on-potential corona current sensor measures the current directly where the connection of the cable coming from the high voltage source meets the overhead conductor

itself. While this does not exclude insulator losses, it does avoid all other leakage currents present between the high voltage source and the line (i.e. along a long high voltage cable connection and bushing, see also chapter 5).

Figure 13.3 shows that most of the time, the source current and the line current match extremely well. However, sometimes, the current as measured by the source has some extreme peaks not measured by the on-potential line current sensor.

The current difference during those peaks were determined to generally occur on the bushing installation between the high voltage source and the overhead line itself generally during intense rain. Figure 13.4 bottom shows such a peak. After the 9:15 mark, as the source current comes down to a steady state, it can be seen that its value remains higher to the line current, unlike during the steady state preceding the peak.

LaForest et al. (1963) note that "corona losses on actual lines are always associated with insulator loss" and use this as a justification for not even attempting to discriminate corona currents due to discharges on the actual line conductor from other current sinks. This reasoning supports presenting the current data from this experiment as is.

Figure 13.4 also shows the relative lack of resolution of the voltage source measurements. The quantization steps are especially visible for smaller current values and will be visible in the rest of the data presented. Beyond the difference in sampling frequency, the on-potential measurements are oversampled (internally, the sensor measures more samples per second than what is displayed, and it sends out data points averaged over time), which causes a significantly smoother plot line. However, statistically, noisier voltage source current will still reflect similar trends to the on-potential sensor data.

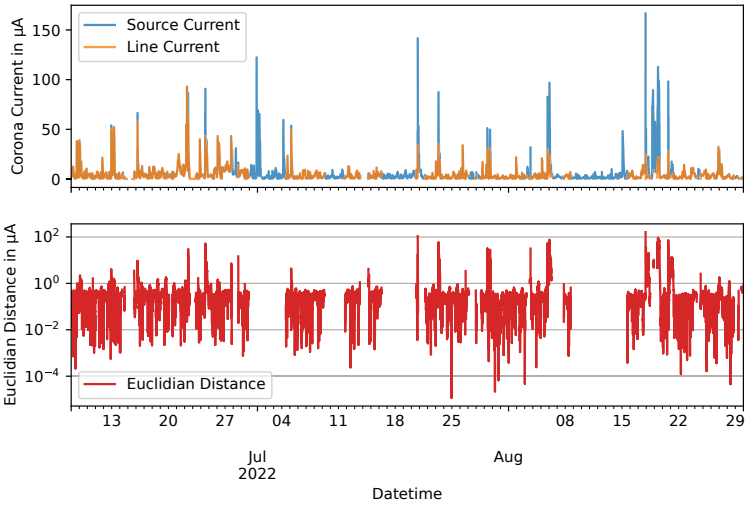

Figure 13.3: Comparison of the corona current as measured by the high voltage source and the IoT sensor directly connected to the line over a period of 6 weeks using mean values as resampled every 5 minutes. Note that the IoT sensor is not always active during the time when the line is energized while the current measured by the source is always recorded. Overall the two signals match well, but large peaks of the blue plot line sometimes largely exceed the orange plot line.

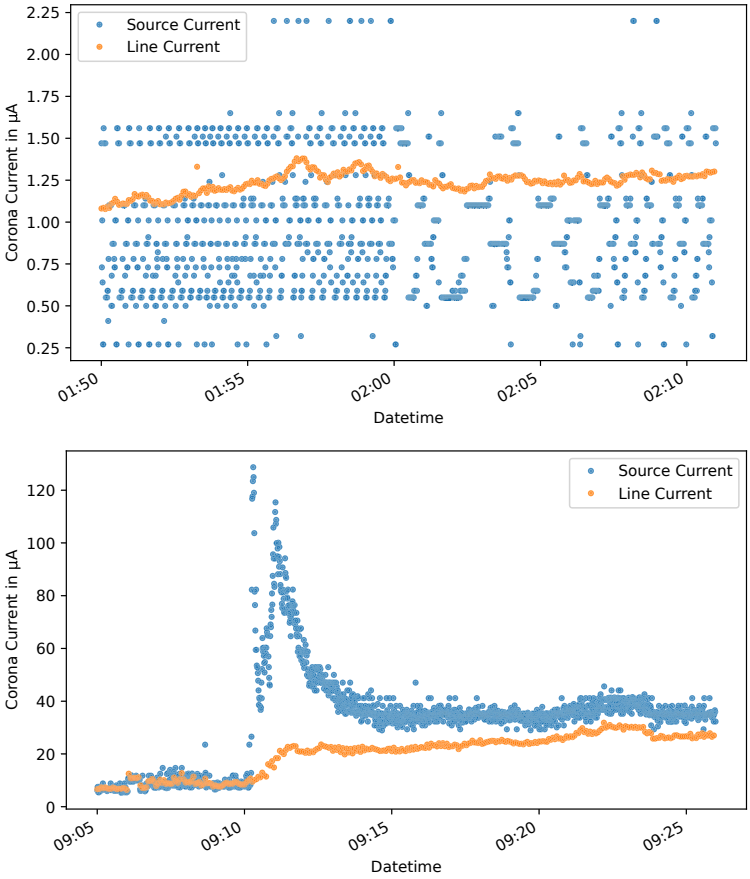

Figure 13.4: Comparison of the corona current as measured by the high voltage source and the IoT sensor directly connected to the line over two 20 minutes windows using raw measurement samples. The difference in sampling rate and resolution becomes apparent. Note that the y-scale is different for the top and bottom plots.

13.4 Distribution of corona current samples

In (EPRI 1993, Ch. 3) it is noted that experimental corona loss data for HVDC lines is "quite fragmented and often not-self consistent" and that it is typical of HVDC corona data to show large spreads. This large range in corona current values and the stochastic nature of processes associated with it encourages looking at corona current distributions rather than other summarizing quantities such as an arithmetic mean over a certain period of time. Studying the distribution of a dataset allows to aggregate the samples in simple and easy to compare visualizations while retaining the full span of the information it contains as also discussed in chapters 10 and 11.

Histograms, such as those in figure 13.5 are among the most common ways of presenting univariate datasets. As noted in (Dekking et al. 2005, Ch. 15), the choice of bins has a big impact on the way the data looks. The top and bottom plots in figure 13.5 are extreme examples where not only the overall shape of the histogram changes but even the position of the highest peak is shifted based solely on the choice of bin width.

Kernel density estimate (KDE) functions such as in figure 13.2 are also very sensitive to tuning parameters such as their bandwidth. Empirical cumulative distribution functions (ECDF) on the other hand, have no such dependencies. They always fully reflect the dataset they represent and are based exclusively on observations. An example is given in figure 13.6, where the data from figure 13.5 is displayed as an ECDF.

The ECDF has an S-shape, with relatively flat parts for very low and very high current values and a steeper part for medium current values. This corresponds to the bell shape of a histogram or KDE. Sometimes ECDFs are shown with non-linear axis for the y-axis, preferring for instance so-called probability scales designed so that perfectly normal distributions produce perfectly straight lines (Berendsen 2011, Ch. 4).

ECDFs with linear y-axis have the advantage of making no assumption about the distribution of the underlying dataset, nor of being de-

pendent on any parameter that one could tweak. One other advantage they have over histograms that is significant for us is that it is often easier to compare overlapping distributions when represented as ECDFs.

Figures 13.2 to 13.6 also show that long-term corona current data ranges over several orders of magnitude. Hence, corona currents will always be presented on a logarithmic scale when considering long-term distributions. A logarithmic scale should also make the small differences in amplitude when compared to on-potential measurements less significant. Sometimes, notably when presenting corona currents as time series, a linear scale might be more appropriate and will also be used.

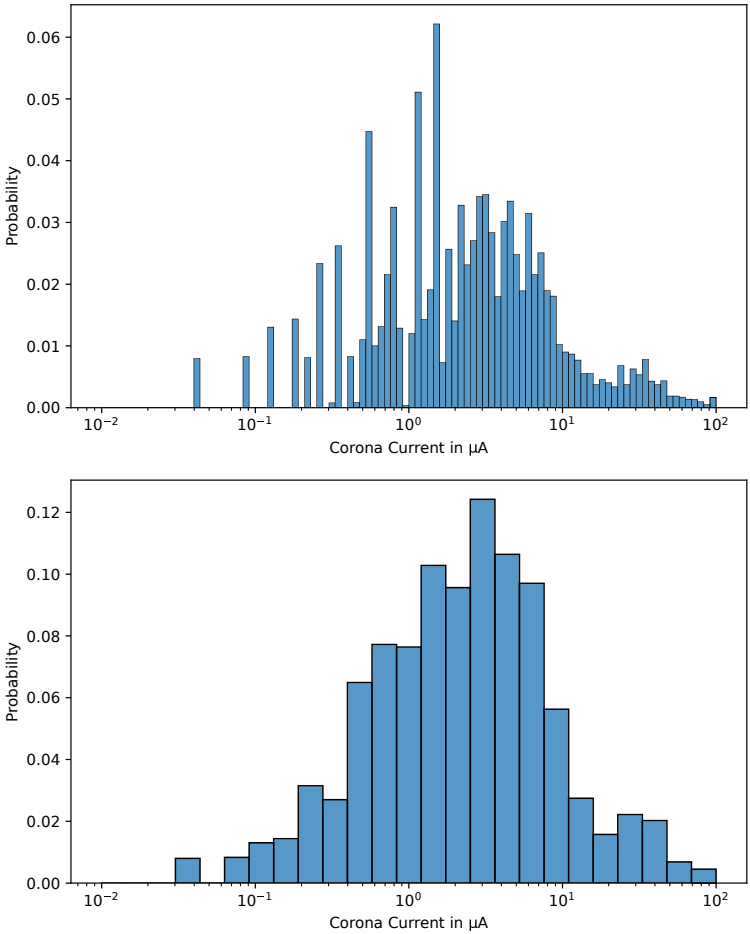

Figure 13.5: (Top) Histogram of all current samples in the dataset studied hereafter using 100 bins. Note that the x-axis is logarithmic. Due to the limited resolution of the current measurement, small values cause notch like artefacts in the histogram. (Bottom) Histogram for the same data but with only 25 bins. Both histograms are respectively normalized such that the bar heights sum to 1.

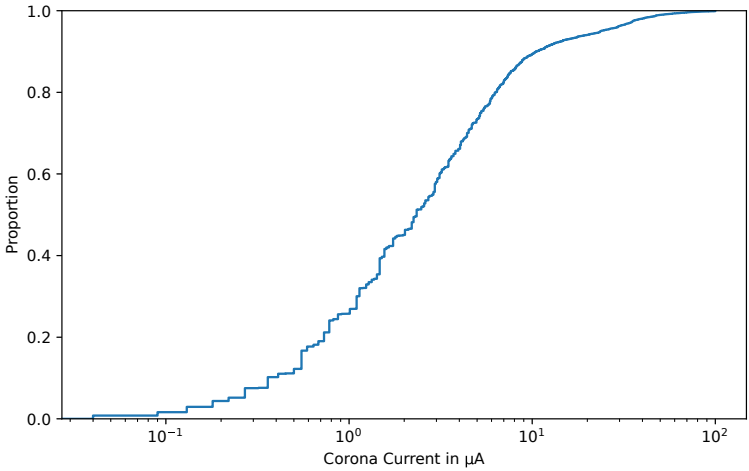

Figure 13.6: Same data as in figure 13.5, but this time as an empirical cumulative distribution function rather than a histogram. The y-axis is linear.

13.5 Empirical cumulative distribution functions in corona research

In 1961, Mather and Bailey (1961) were among the earliest authors to introduce the use of empirical cumulative distribution functions (ECDFs) to present corona data.

ECDFs have since been used quite extensively to compare radio interference data caused by corona under different conditions by Anderson and Zaffanella (1972), Bailey (1967, 1970), Mather and Bailey (1963), Olsen, Schennum, and Chartier (1992), Perry, Chartier, and Reiner (1979), and Sawada et al. (1977). Some (EPRI 2005; Tian, Yu, and Zeng 2012; Trinh 1995) show radio interference ECDFs alongside

audible noise ECDFs. In fact ECDFs are widely used in the context of corona generated audible noise during rain as well (Chartier and Stearns 1981; EPRI 2005; Perry, Chartier, and Reiner 1979; Xie et al. 2020).

When it comes to radio interference noise and especially audible noise, ECDFs are often used in conjunction with the concept of so-called L_n exceedance levels. Here n is a number between 0 and 100 (most commonly 5, 10, 50 or 90) that indicates the percentage of time when the L_n value is exceeded for a given dataset. These L_n levels are commonly used in acoustics (Perry, Chartier, and Reiner 1979; Straumann and Fan 2009), not only for noise caused by corona, but also for instance to quantify traffic noise and have become standard practice in the study of radio interference as well (EPRI 1993). L_n exceedance levels can be read directly on ECDF plots, by looking for the x-axis value for which the plot line crosses the horizontal line $y = \frac{n}{100}$.

ECDFs are less often seen to represent other corona related quantities. An early publication showing corona loss distributions as ECDFs is (LaForest et al. 1963). Here corona losses for different tower geometries are compared. Maruvada, Trinh, et al. (1977) and Maruvada, Trinh, et al. (1981) show ECDFs for radio interference, audible noise and corona losses, all three as dB values above a reference, in order to compare different bundle arrangements. The authors even state that ECDFs are the way in which "the statistical corona performance of a long line is generally expressed" (Maruvada, Trinh, et al. 1981). (Yu et al. 2019) is a rare recent example where ECDFs are used to show corona loss distributions. Comparisons of varying wind speeds and line geometry are made. The same research group from Tsinghua also have a publication where ground level ion current distributions are given for different wind and weather conditions (Ya et al. 2019). In (Maruvada, Dallaire, and Rivest 1984), ion current ECDFs are given together with electric field and even ozone level distributions.

In this report, corona current is generally be given on a logarithmic

axis similarly to (LaForest et al. 1963) and unlike (Yu et al. 2019). However, the percentage of time above a certain current value is on the x-axis and the current on the y-axis as in (Yu et al. 2019) and this time unlike what can be seen in (LaForest et al. 1963). This should make it easier to present and compare data distributions.

13.6 Defining rain events

Rain events and their definition are much discussed in meteorological sciences (Dunkerley 2008; Larsen and Teves 2015). Intuitively, a rain event is the period of time between when rain starts and rain stops. However, a rain event does not have to be a period of continuous rain and even time intervals with short interruptions in precipitation can be considered to be part of a single rain event. In fact the nature of rain is such that it falls in discrete drops and is thus de facto discontinuous in time. Additionally, rain detectors have a fixed and limited sampling area and time associated with them.

Thus, it is only by defining an arbitrary duration for rainless intervals, the so-called Minimum Inter-event Time (MIT) that rain events can be defined. In their literature review Dunkerley (2008) finds this MIT to vary from 15 minutes to 24 hours and Larsen and Teves (2015) note that different fields of studies tend to use different values. A quick survey shows that the MIT also has geographic specificities depending on the local climate (Carbone et al. 2014; Medina-Cobo et al. 2016; Nojumuddin, Yusof, and Yusop 2018).

Regarding corona, in addition to when precipitation is being measured, the distinction between a still wet conductor and an already dry one after rainfall is of interest. In this study, it was observed that 3 hours after the last rain was recorded by the weather station, most of the time the corona activity on the conductor can be considered to have returned to its steady-state level prior to the first rain detected for that event.

The MIT is thus arbitrarily set to 3 hours anytime rain events are dis-

cussed in this report. Other corona researchers such as LaForest et al. (1963) require no rain during the previous 4 hours to declare a period as dry, which is comparable to this criterion.

Since the weather station is only sensitive to rain rates of 0.2 mm or more in intervals of 5 minutes, it can occur that it fails to detect the true beginning of a rain event. A qualitative assessment of the dataset indicates that often rain events begin with rainfall below this threshold before increasing in intensity. It was thus decided to also include the 20 minutes prior to the first rain reported by the weather station in the definition of rain events for this study. A rain event is shown as an example in figure 13.7. Every 5 minutes interval during which the measured rain was non-zero is a period of *active rain* as opposed to other instants during a rain event when no rain was measured.

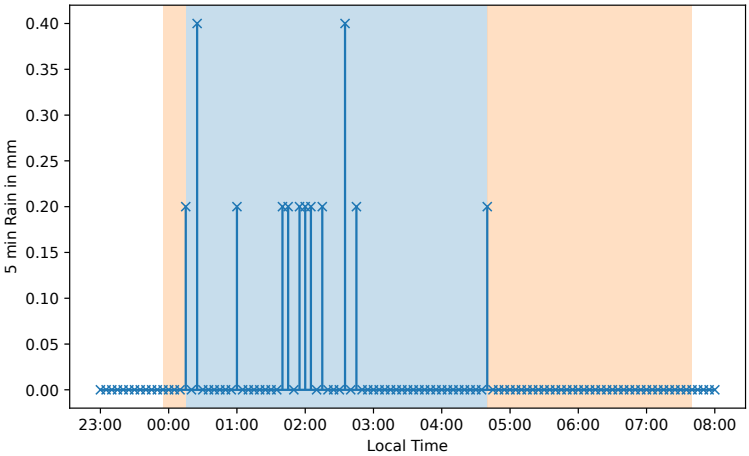

Figure 13.7: Example of a typical rain event. The event ends after no rain is recorded during 3 consecutive hours (orange shaded period on the right). The first 20 minutes before the first rain is measured is also included (orange shaded period on the left).

Chapter 14

General Observations and Fair Weather Corona

14.1 Fair versus wet weather and seasonality

Figure 14.1 shows the empirical cumulative distribution (ECDF) of corona currents for the studied dataset for fair and wet weather. The plot shows that current values can be up to orders of magnitude larger in wet weather rather than during fair weather. Currents smaller than 0.1 µA are only recorded outside of rain events. Those smaller than 1 µA can occur during rain events, but only during drying phases; no such currents are observed during the active rain period of rain events.

While large currents above 10 µA can happen during fair weather, those account for less than 4 % of the measured data whereas they amount to over 55 % of the samples while the line is wetted by rain and even over 95 % during active rain periods.

Since a large majority of the time the weather was fair, the curve for the entire dataset resembles that for fair weather only. However, both curves diverge for higher currents which are fewer during fair weather.

To simplify the description of later ECDF plots, “shape classes” are attributed to the curves in figure 14.1. The entire dataset and fair weather curves have a similar shape and are reminiscent of the *S-shape* discussed regarding figure 13.6. The active precipitation curve, with its much closer to vertical middle part, larger curve at the bottom and short flat top is more reminiscent of a *J-shape*. The entire rain event curve (which also includes drying period as well as periods within a rain event when no active precipitation was measured) is in between the *S-shape* and the *J-shape* with its longer diagonal section and short horizontal parts both at the top and bottom. In more mathematical terms, the *J-shape* exhibits the most obvious concave up curve (negative first and second derivatives) while the *S-shape*d curves show a larger concave down (negative first derivative but positive second derivative) portion (in their upper third).

While corona currents are lower during fair weather than wet weather, it does not mean that they are negligible in dry conditions.

Figure 14.2 shows the different corona current distributions for spring and summer. Unlike previous reports from literature, the corona currents presented here were generally smaller in the summer than in the spring. And this despite more rain having been measured in summer than in the spring.

With the dataset limited to a single year and seasons not being captured in their entirety this can not directly be attributed to climatic specificity. However, it again illustrates the need for more long-term measurements in more geographic locations. Indeed, differences between seasons can vary a lot from place to place, and it is difficult to make general statements based on observations in a restricted number of environments.

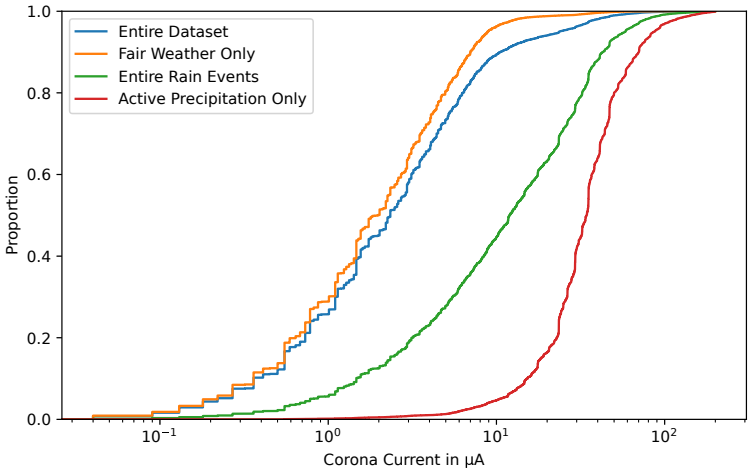

Figure 14.1: Proportion of current samples above a certain corona current value for the entire dataset, during fair weather only, during entire rain events (including drying phases) and only during the phases within rain events when active precipitation was actually measured. Note that the x-axis is logarithmic.

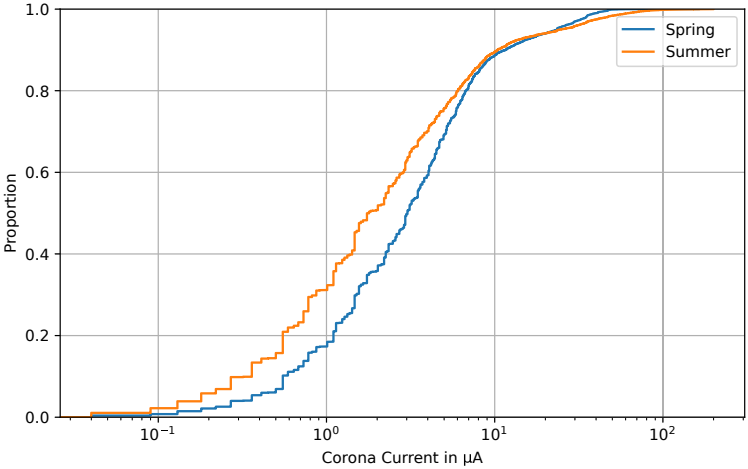

Figure 14.2: Current distribution according to seasons. This plot includes the entire dataset regardless of weather condition.

14.2 Time series

To gain more insight into fair weather corona, corona figure 14.3 shows the corona current directly as a time signal.

Plotting the raw current signal as time series results in a relatively convoluted image as shown by the blue trace in figure 14.3 (bottom). When zooming in and drawing each individual point such as in figure 14.3 (top) it becomes obvious that most data points lay in a baseline on top of which current peaks, that can be several times higher in amplitude than the baseline, are observed. Those peaks can last at least a few tens of seconds which indicates that they are not merely attributable to measurement noise.

It is possible that those current peaks are caused by attached particles which burn away or otherwise appear and disappear in the time scales visible in figure 14.3 (top). Full-scale overhead test lines, or indeed operating lines have a significantly larger surface to which such particles could attach. A line of significantly longer length, with more than one conductor in a bundled configuration, and larger circumference due to larger conductor radius could have so many of those particles simultaneously coronating, that the individual peaks might no longer be perceptible and thus the baseline shifted.

This is an illustration of how different corona modes identifiable for HVDC corona (section 2.3) directly impact the behaviour of the various corona effects. Again, the corona current studied here is not the current from a single discharge source, but the total current from all corona sources along the entire test line. On a negatively energized conductor, the total current can be comprised of many small amplitude pulses repeating rapidly, pulseless glow discharges, or moderate amplitude pulses with a moderate repetition rate, but the distinction between those discharge modes is not the focus of this study.

Here, to make the trend of the baseline more apparent subsequent figures will show a line made out of the median of the signal taken every 15 minutes. Indeed, figure 14.3 (top) shows that given the amplitude

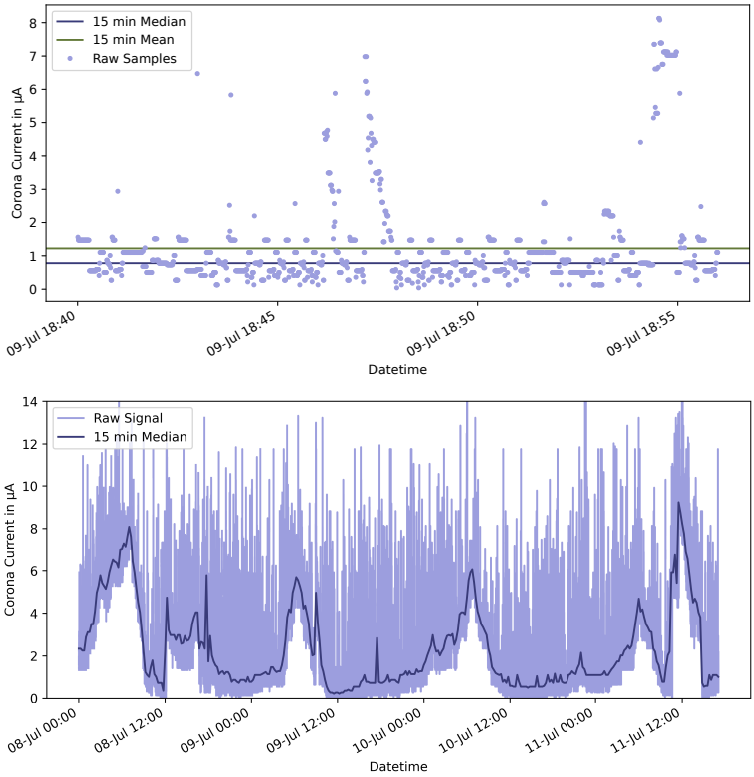

Figure 14.3: (Top) 15 minutes window of the dataset. Raw samples of the corona current are shown as dots. The quantization steps are visible for low current values. Three current peaks are distinguishable above a baseline between 0 µA to 1.5 µA with a more isolated high current samples forming peaks. The median and mean (in purple and green respectively) of the current are also indicated for the time interval. (Bottom) Zoomed out image of the above plot. This time, the raw current is a continuous line. In darker purple, the median of the raw signal resampled every 15 minutes is given.

and duration of typical peaks relative to the amplitude spread of the baseline and the sampling frequency the median is a better indicator of the baseline value than the mean.

14.3 Humidity

Once this 15 minutes median is plotted over longer timespans along with humidity as in figure 14.4, a correlation becomes apparent [1].

The humidity line shows a very obvious daily periodicity which is part of a phenomena known in atmospheric sciences as the diurnal cycle (Betts 2015). Every morning around dawn, as temperature reaches its minimum daily value, relative humidity reaches a daily maximum. This cycle might be drowned in "noise" on rainy days but is otherwise very obvious in figure 14.4.

Figure 14.4 shows that most of the time in fair weather, as the humidity reaches its diurnal peak, the corona current will also show a coinciding peak if not its own daily maximum. This correspondence is nevertheless not bijective. For instance in figure 14.4 on the 6th of July, the highest point of the 15 minutes median current is reached during when the diurnal humidity peak is around its minimum.

Condensation

One might wonder whether this is simply caused by condensation on the line. However, the consistency of those peaks seems to speak otherwise. Comparing the daily minimum temperature, with the dew point in figure 14.4 shows that the peaks occur regardless of the difference between the two. The temperature is measured at a height above ground very close to that of the line. One can assume that the conductor surface temperature will never be significantly lower than that of the minimum measured temperature during a given day, if at

[1] In the appendix B, similar time series for the entire dataset are given to show that figure 14.4 is not merely a coincidence.

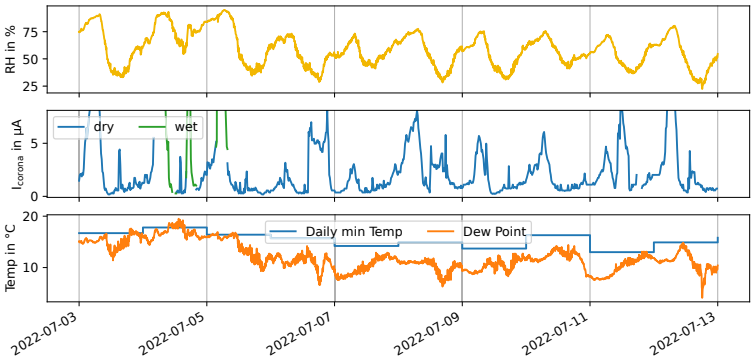

Figure 14.4: (top) Relative humidity, (middle) corona current and (bottom) dew point in orange and daily minimal temperature in blue. Note that during rain events, the current is plotted in green while it is blue otherwise.

all. On real operating lines carrying a load current, conductor surface temperature will be above the dew point even more often.

Humidity and temperature correlation

Diurnal cycles affect other atmospheric parameter than the relative humidity such as the ambient air temperature. In fact, as suggested by figure 14.5 (top), temperature and humidity are very correlated. As stated before, the diurnal maximal humidity occurs around the same time as the diurnal minimal temperature. Nevertheless, the data suggests that humidity is more of a factor in determining dry corona current than temperature. Indeed, the peak correlation was observed on days in May when the temperature varied from 12 °C to 18.5 °C as well as on days in July where the range was from 22 °C to 37 °C.

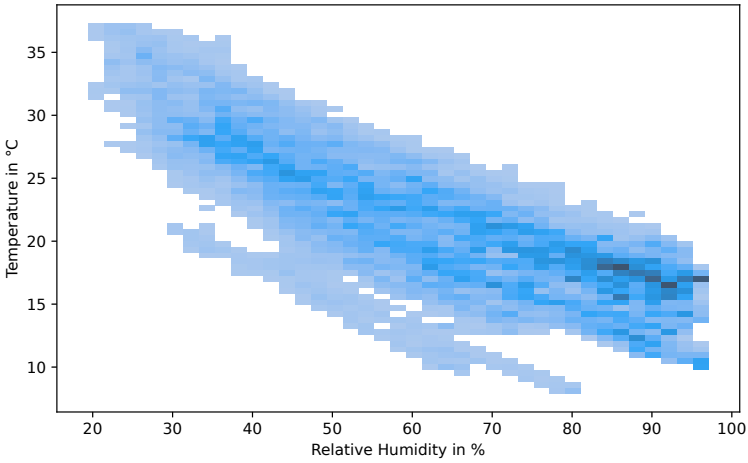

Figure 14.5: Heatmap of the 2D histogram showing humidity and temperature samples collected by the weather station. Note the obvious diagonal correlation.

Aggregated statistic

Trying to quantify the correlation of the humidity and corona current as time series using for instance a Pearson correlation with a moving window does not yield meaningful results. Despite the obvious peak correlation, the absolute values of the humidity, the current peaks or the current baseline tend to vary too much. Moreover, the current signal contains too many features not reflected in the humidity.

While not constituting a direct illustration of the correlation between corona current during fair weather and ambient relative humidity, the plot on figure 14.6 shows some trends nonetheless. This representation is obtained by binning together the humidity data and looking at the aggregated dry corona current distribution for each of those hu-

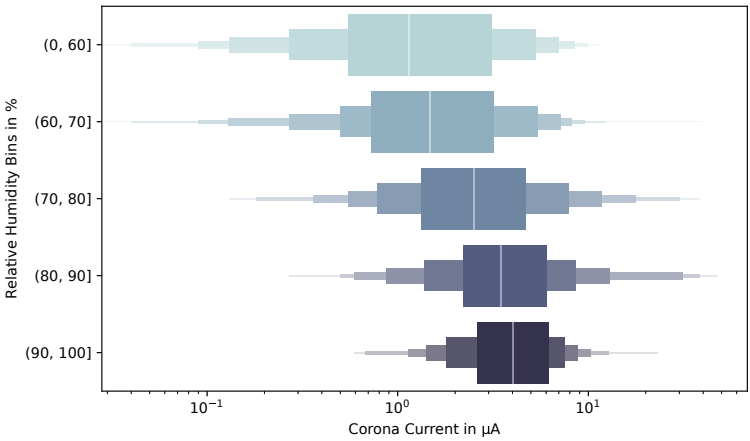

Figure 14.6: Enhanced box plots showing current values binned by relative humidity levels. Note that the x-axis is logarithmic.

midity bins.

The distributions are then plotted as so-called enhanced box plots (also sometimes referred to as letter value plot). First introduced by Hofmann, Kafadar, and Wickham (2011), the implementation from the Seaborn Python package (Waskom 2021) is used here. Enhanced box plots, as their name indicates, aim to provide more information than that found in traditional box plots. In particular, they offer more detail at the tail ends distributions by showing quantiles beyond the quartiles that define the bound of the single rectangle of traditional box plots. This is meaningful in particular for larger datasets ($n > 200$, as is the case for the presented long-term corona currents), where the reliability of values beyond quartiles is greater.

For figure 14.6 the enhanced box plots were plotted using the following options:

```
k_depth='proportion', outlier_prop=0.03
```

further documented in (Hofmann, Kafadar, and Wickham 2011; Waskom 2021). The white vertical line within the middle is the median of each distribution, just like it would on a simple box plot.

On figure 14.6 the median clearly shifts to the right of the current axis as humidity increases. It is also clear that as humidity increases, the smallest recorded current values increase as well. However, the high current samples are already present in the 60 % to 70 % relative humidity range as well as those above, although the very highest values were not observed for the 90 % to 100 % bin. While it is difficult to say whether this is due to there being less current samples for those very high humidities, there is a notable tendency for the spread in current distribution to shrink as humidity increases.

While the dataset is biased towards larger humidity values, it also seems to be the case that the effect of humidity only manifests itself significantly for humidities above 65 % to 70 %. The exact same observation was made by Comber and Johnson (1982) for ground level electric fields and ion currents. A larger dataset with more measurements during periods of low relative humidity might help explain why.

Also note that the results presented here can be compared to those presented in section 10.5 that seem to indicate that for dry corona, while the amplitude of the discharge pulses are generally lower with higher humidity, their number increases significantly. On the other hand, for a line wetted by condensation, section 10.4 suggests that corona activity should increase with decreasing humidity.

14.4 Wind

For wind, the deviations expected between this setup and a full scale test line amount to more than the reduced geometry. Indeed, a more realistic conductor arrangement will have several parallel conductors.

Whether it be a pole of opposite polarity, a metallic return conductor, AC lines in a hybrid AC/DC setup, or even just the earth wire, they will all act as electrodes (in addition to the ground plane) towards or away from which wind can blow from the perspective of the studied conductor. These additional electrodes impact the trajectories of space charges just like wind does and, if coronating, add a source of oppositely charged space charges that can be transported close to a conductor through wind. Such effects have been studied for instance in EPRI (1993), Hirsch and Schafer (1969), and Khalifa and Morris (1967).

Moreover, architectural constraints in this rooftop setup strongly colour the distribution of wind directions which for an overwhelming majority have a dominating component collinear to the line which is parallel to a nearby building wall.

Most studies on the effect of wind on corona losses report increasing losses with wind velocity (Bailey 1967; Gehrig et al. 1967; Hirsch and Schafer 1969; Yu et al. 2019). Bailey (1967) suggests that the increase in corona current grows linearly with the normal component of the wind velocity. Maruvada, Trinh, et al. (1981) establish linear correlations and compute their parameters. While they note that corona losses generally increase with wind velocity, they do observe negative correlations for specific wind directions on the positive pole of their bipolar test line.

Some other authors have also reported decreasing corona losses on negative lines with increasing wind speed in specific conditions for specific wind directions. Khalifa and Morris (1967) report that on a negative unipolar line parallel to a grounded line, corona losses decrease as the wind speed blowing from the grounded line to the energized line increases. In (EPRI 1993, pp. 3–163), bipolar lines show a decrease in corona losses on the negative pole for increasing winds blowing from the negative to the positive pole.

The observations presented in figure 14.7 seem to suggest losses decreasing with increasing wind speed. In this setup, wind is mostly collinear, and consequently the normal components are small or in-

existent. This is not usually a wind direction studied by the authors cited above.

Additionally, while monopolar, the line's reduced geometry puts it in proximity with grounded fences or the ground itself. It is thus not "as monopolar" as the monopolar cases discussed in literature while not being bipolar either.

Moreover, the range of wind speeds observed is relatively small. For instance, while one of the conclusions in (Yu et al. 2019) is that corona losses increase with wind speed, they only show a distribution for wind speeds ranging from 1.5 m/s to 5 m/s and one for wind speeds from 2.5 m/s to 10 m/s. In the present case the highest wind speed recorded was 2.25 m/s which makes a direct comparison difficult. This strong skew towards lesser wind speeds also explains why the curve for strong winds is so similar to that for medium winds.

The higher the wind, the lower the maximum current value as illustrated by the curves (almost) reaching the top further to the left as wind increases. This is again analogous to conclusions in (Comber and Johnson 1982) regarding ion current peak values.

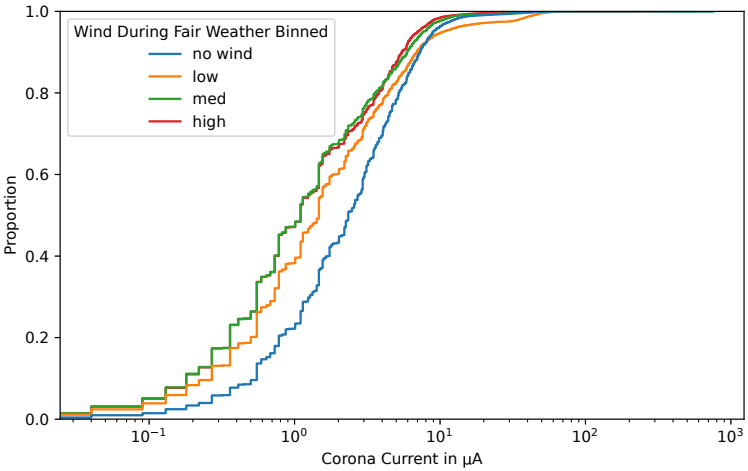

Figure 14.7: Currents binned according to the 5-minutes average wind measured outside of rain events. Low winds are up to 1 km/h, medium up to 2 km/h and high are above. "No wind" data is data recorded during fair weather with no measurable wind speed.

Chapter 15

Characterizing Foul Weather Corona

15.1 Rain rate metrics

Contrary to AC (EPRI 2005; Lundquist 1990), there are no widely used rain rate corrections in the audible noise prediction formulas for DC as discussed in section 3.2. This does not mean that the magnitude of rain does not affect wet weather DC corona behaviour.

The magnitude of rain itself is not trivial to quantify. In this work, three metrics to characterize precipitation during rain events are defined. They are all computed using the same source raw data which is the precipitation data from the local weather station. Every 5 minutes, the weather station gives an amount in mm of how much rain has fallen within the last 5 minutes. The smallest amount of rain it can detect during this time interval is 0.2 mm. In general a rain event such as defined in section 13.6 will contain more than one of those 5 minutes quasi-instantaneous values, but not all recorded precipitation value greater than zero have to be consecutive. It is recalled that the end of a rain event is set three hours after the last rain was measured for that event.

- *Maximum rain rate*: The highest 5 minute value recorded during the entire event. It is an instantaneous value (within the time resolution limit of the weather station) and says nothing about the rest of the event.
- *Cumulative rain*: The sum of all precipitation values recorded during the entire rain event. In other words, this metric indicates how much water the line was exposed to during a rain event.
- *Average rain rate*: The cumulative rain rate divided by the number of non-zero precipitation samples. This value reflects the intensity with which it rained during the event, on average, and when it was raining at all. A 2 hours pause between two active precipitation phases of a given rain event will not impact the average rain rate.

Figure 15.1 shows the raw measurements during a rain event along with the three metrics above.

The ECDFs in figure 15.2 show that in general, the dataset is skewed towards lesser rain events. All three metrics show appreciably different distributions particularly in the lower half of their range.

Figure 15.3 shows the occurrence in the studied dataset of specific combinations between the metrics which correspond to intuitive descriptions of rain events. Long and intense rain events will have both a large cumulative rain and a large average rain rate. Meanwhile, short and intense rain events will have a high average rain rate and a high maximum rain rate, but the cumulative rain could be low. Short and gentle rain events will have low values for all three metrics etc...

Characterizing single rain events

Figures 15.4 to 15.6 show the current distribution per rain event as enhanced box plots[1] with the events sorted by their respective rain

[1] Enhanced box plots are discussed in more details in section 14.3. The same settings are used here.

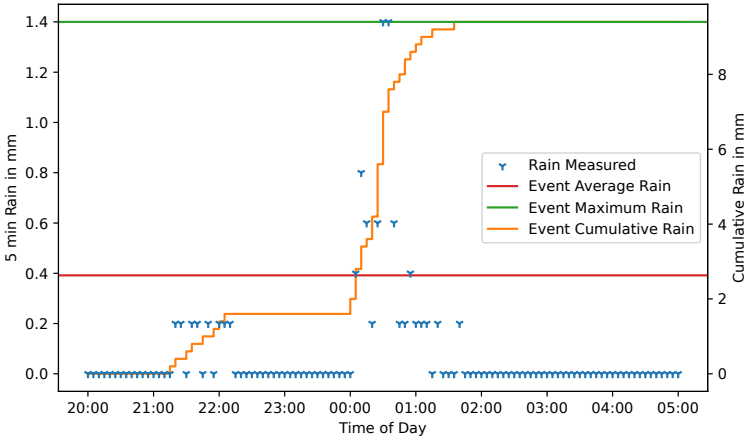

Figure 15.1: Example rain event showing the rain metrics defined in section 15.1. The blue three branched stars represent the raw samples measured every 5 minutes. The average rain rate for the event amounts to 0.39 mm per 5 minute as shown by the red line. The maximum rain rate was measured twice, once at 00:30 and once at 00:35 and reached 1.4 mm, as shown in green. At the end of the rain event a cumulated amount of 9.4 mm was measured.

metric, from low at the top to high at the bottom.

A slight increasing trend is visible for cumulative rain in figure 15.4. Indeed, broadly, the further down a box plot is, the further to the right it will be. But even then, some box plots are very elongated and others very short regardless of how high or low they are. The light-coloured vertical median line within each box plot, too, has a general tendency to shift towards the right from top to bottom, but the trend is very vague and shows many inconsistencies.

The behaviour seems even more erratic for average and maximum

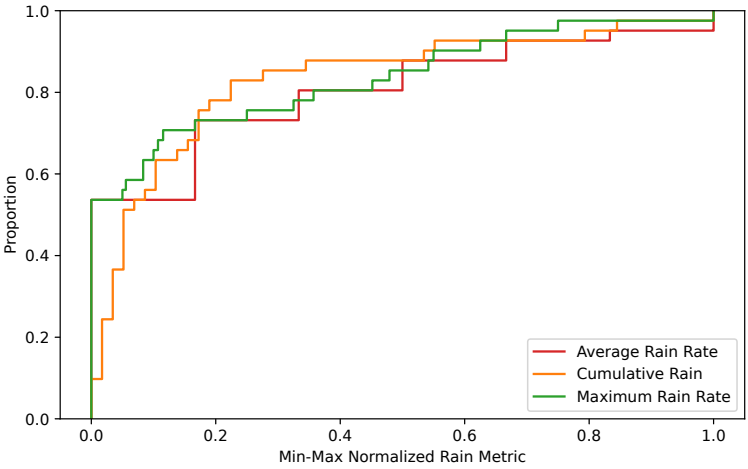

Figure 15.2: Overall distributions of the different rain metrics.

rain in figures 15.5 and 15.6 respectively. No trend can be discerned, not even a loose one.

Here again it is useful to plot empirical cumulative distribution functions (ECDFs) aggregating the data from several comparable rain events. They avoid the biases inherent to every single event and their curves are not fuzzy. The aim is to "visually quantify" trends that are either not at all visible or only intuitively visible in figures 15.4 to 15.6. ECDFs might also show that while no overall trend is visible, there is a trend at least for a subset of current values.

Aggregated characteristics of corona current during rain

In the paragraphs that follow, ECDFs are shown for all the recorded rain events grouped in three categories; weak, medium and strong.

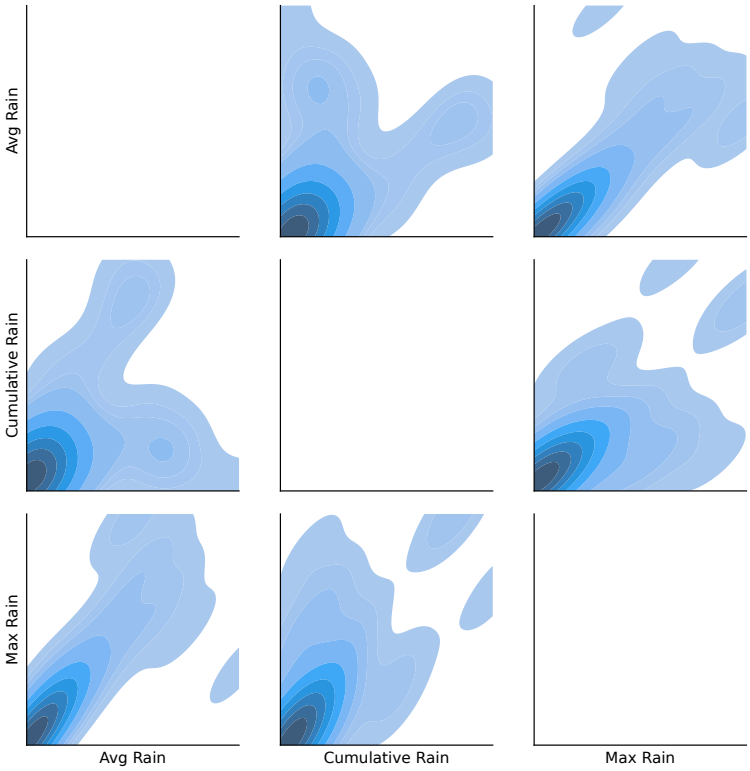

Figure 15.3: Pairgrid showing correlations as bivariate KDEs between different rain metrics. Attention is drawn to the general shapes and not the absolute value hence the absence of graded axis; nevertheless, for each subplot values further right or further up are higher and further down or left are lower. Darker colours indicate more rain events with both metrics in the corresponding range. The diagonal is left empty.

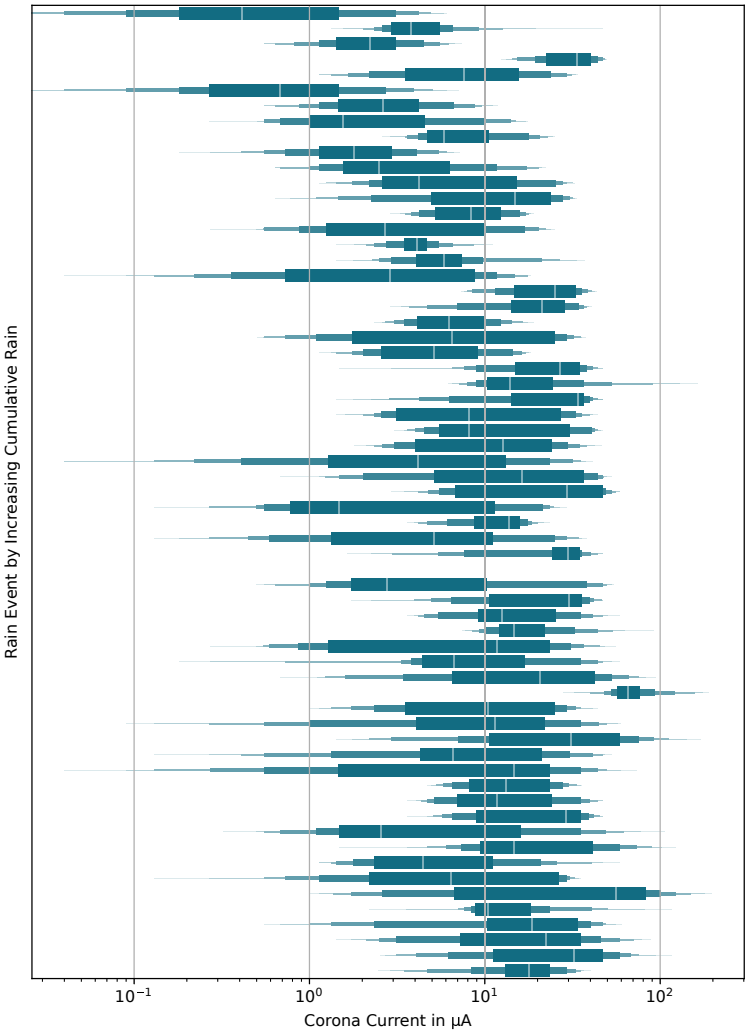

Figure 15.4: Current distribution per rain event as enhanced box plots. Each box plot contains all current samples for one event. Events are ordered by increasing cumulative rain during the event, from top to bottom. Note that the current scale is logarithmic.

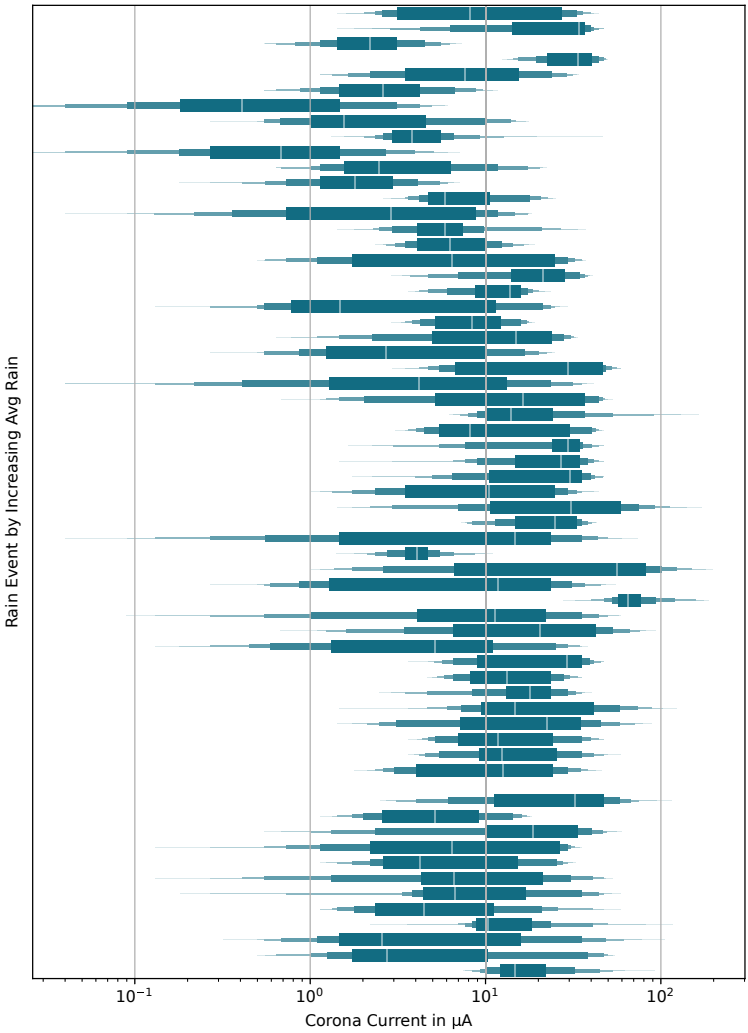

Figure 15.5: Current distribution per rain event as enhanced box plots. Each box plot contains all current samples for one event. Events are ordered by increasing average rain rate during the event, from top to bottom.

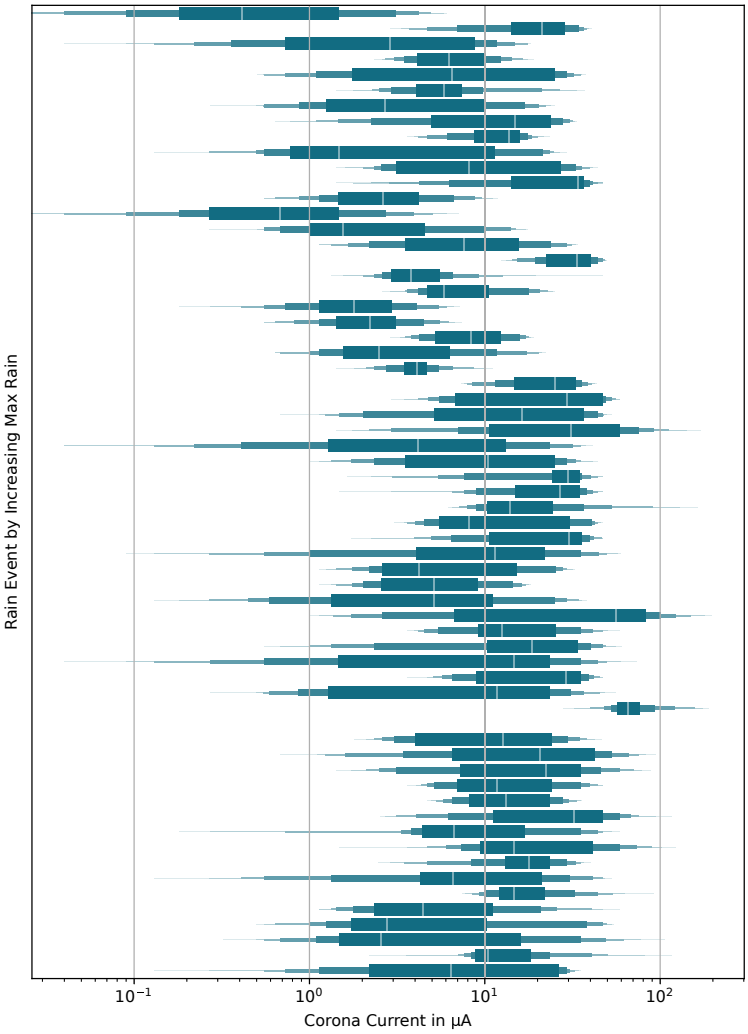

Figure 15.6: Current distribution per rain event as enhanced box plots. Each box plot contains all current samples for one event. Events are ordered by increasing maximum rain rate during the event, from top to bottom.

While those categories are to a degree arbitrary and do influence the resulting ECDF curves, they were determined by looking at the histograms of the rain metric in question and intend to balance the availability of the data and the manifestation of trends.

Figure 15.7 establishes that lower current values are found more frequently for lower cumulative rain. Thus, until currents of about 20 µA, the plot lines appear in the order: no rain, weak, medium and strong. Above 20 µA, the lines for medium and strong cross each other, but remain very close together. The steeper slope of the red curve indicates that currents are more concentrated during strong cumulative rain (on a logarithmic current scale).

The highest currents observed under low cumulative rain are also observed in fair weather, although the flatter blue curve at the top indicates that those currents are fewer in fair weather. On the other hand the highest currents observed under medium rain have a very similar distribution under strong rain.

Figure 15.8 shows relatively similar curves for maximum rain rate to those in figure 15.7 for cumulative rain. But here, the crossing between the curves for medium and strong rain happens much lower, around the 40 % mark and the separation between both curves is more obvious for larger current values. In fact, higher current values occur more often for events with medium rather than high peak rain intensities.

Looking at the average rain rate distributions in figure 15.9, the results are even more surprising. Here the strong curve appears fully left of the medium curve indicating that for the events with the highest average rain intensities, currents are generally lower than events with medium average rain intensities.

While the behaviours highlighted here might be due to biases in the dataset, they are a reflection of the observed rain events. Looking back at figure 15.3 it can be noted for instance that events with large cumulative rain tended to have relatively medium average rain intensities and events with high average rain intensities tended to have low cu-

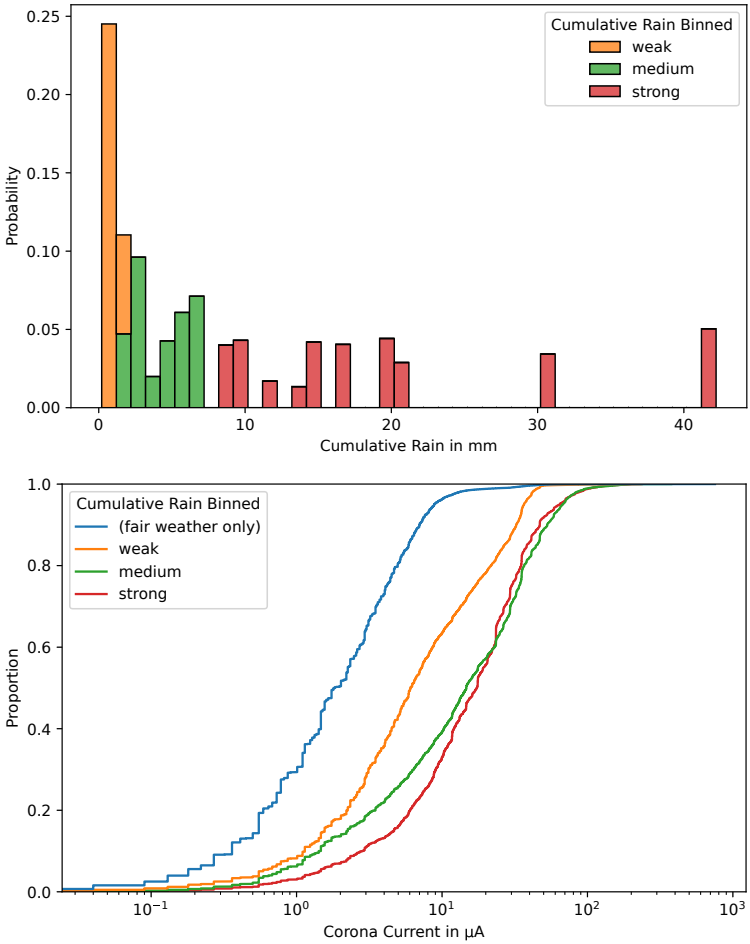

Figure 15.7: (Top) Histogram showing the distribution of cumulative rain per event. Cumulative rain from 0 mm to 1.6 mm, 1.6 mm to 7.4 mm and 7.4 mm and above are coloured as weak, medium and strong categories. (Bottom) ECDF of the current during all events classified according to the event's cumulative rain. The ECDF for fair weather only is shown for reference.

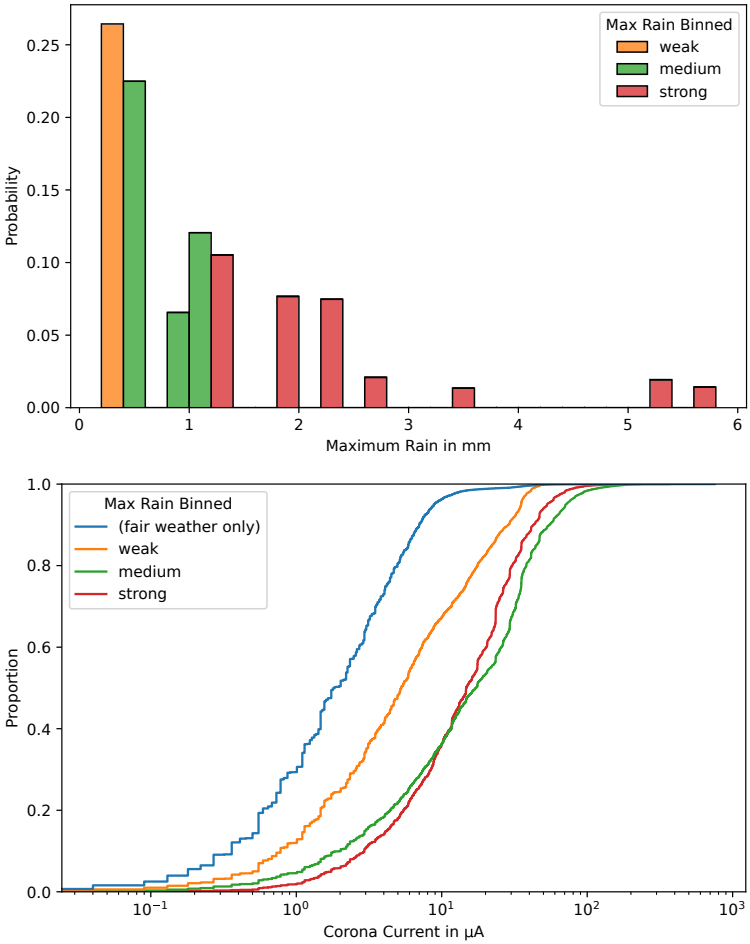

Figure 15.8: (Top) Histogram showing the distribution of maximum rain rate per event. Maximum rain rate from 0 mm to 0.2 mm, 0.2 mm to 1 mm and 1 mm and above are coloured as weak, medium and strong categories. (Bottom) ECDF of the current during all events classified according to the event's maximum rain rate. The ECDF for fair weather only is shown for reference.

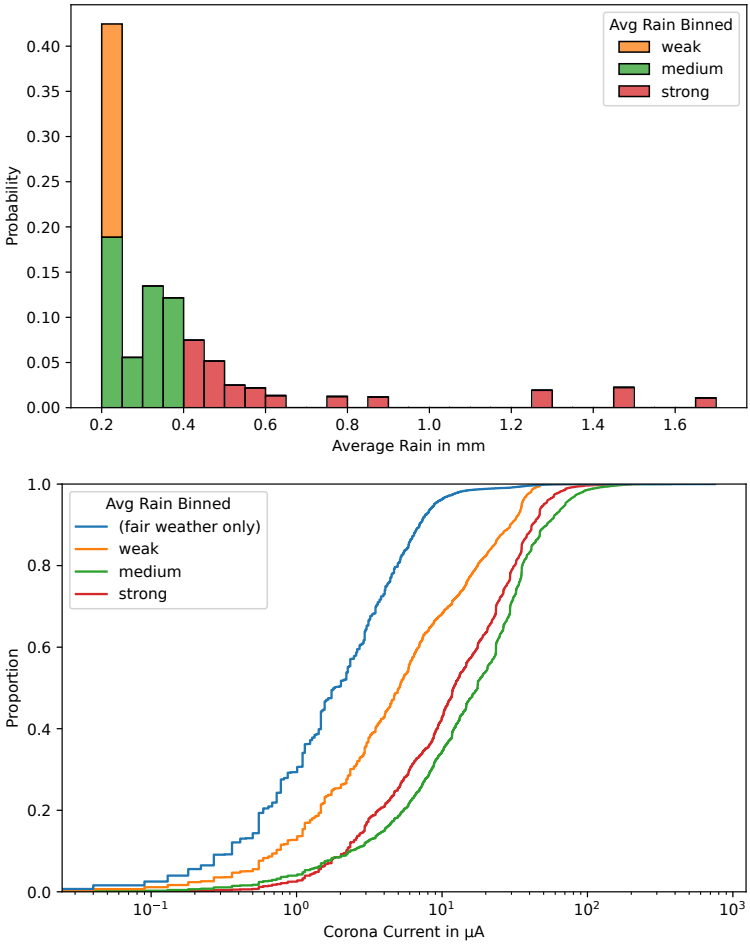

Figure 15.9: (Top) Histogram showing the distribution of average rain rate per event. Average rain rate from 0 mm to 0.2 mm, 0.2 mm to 0.4 mm and 0.4 mm and above are coloured as weak, medium and strong categories. (Bottom) ECDF of the current during all events classified according to the event's average rain rate. The ECDF for fair weather only is shown for reference.

mulative rain. This could explain the non-monotonic curve order observed in figure 15.9.

The next question to ask would naturally be if this combined distribution of cumulative rain and average rain intensity is a bias of the dataset or really characterizing the situation in the experiment's climate. In a different climate, the correlations of figure 15.3 could look different which would impact the shape and order of the ECDFs plots just described.

15.2 Wind during rain

Not only rain metrics are of interest during rain events. Just as it does for dry corona, wind will also affect wet weather corona. Here, the effect is easier to grapple intuitively. Wind blows water drops from the conductor and thus corona behaves closer to what it does in fair weather for stronger winds. This is illustrated by figure 15.10.

For increasing wind speeds the proportion of low currents under 1 µA increases. The middle part of the curves are relatively parallel regardless of wind speed. High currents above 20 µA occur more often for lower wind speeds. Note that rain events are considered in their entirety, including their drying phases as well as precipitation breaks within them. This is justified by the assumption that wind affects the dissemination of water droplets on the conductor regardless of whether it is currently raining or not and that as soon as the line is wetted, its corona behaviour is dominated by droplets.

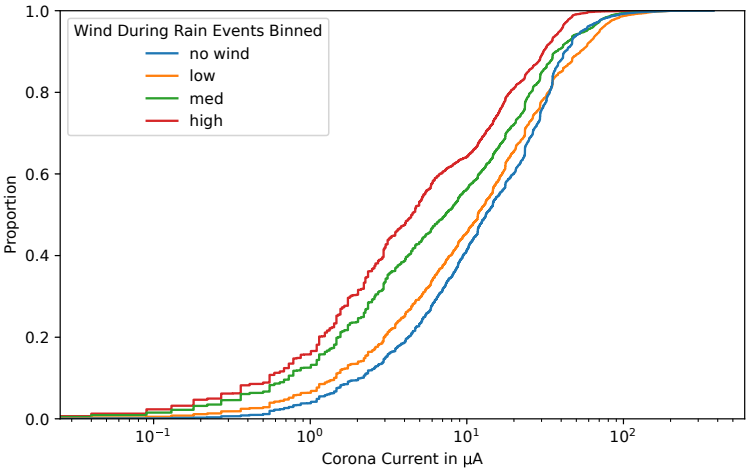

Figure 15.10: Currents binned according to the corresponding 5 minutes average wind speed. Data of all 4 curves taken during all rain events in their entirety including their drying phases. Low winds are up to 1 km/h, medium up to 2 km/h and high are above. "No wind" data is data from moments during rain events with no measurable wind speed.

15.3 Drying phase of rain events

On figure 15.11 the drying phase curve shows a transitional distribution somewhere between an *S-shaped* fair weather distribution and a *J-shaped* wet weather distribution. The flatter shape of the drying phase curve implies that drying phases see a large spread in current values.

This highlights the importance of treating drying phases as a corona regime in and of itself. In other words, wet corona can not be re-

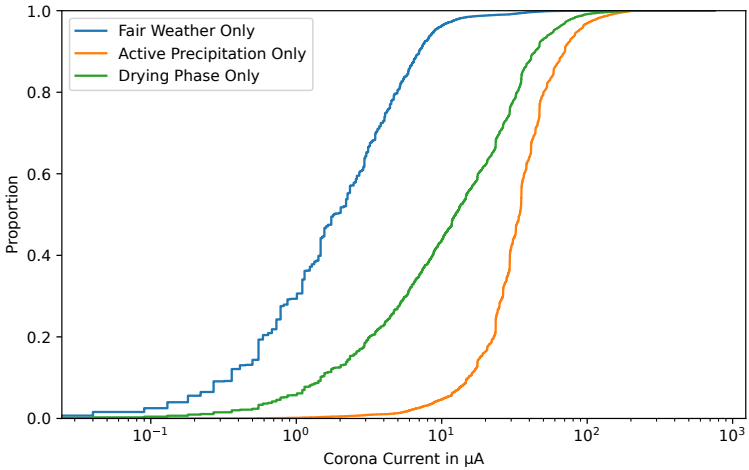

Figure 15.11: Current distribution during the periods within rain events when rain was actively measured and during only the drying phases constituting the last 3 hours of each rain event. Fair weather curve for comparison.

stricted to when precipitation is measured.

Humidity during the drying phase

In figure 15.12, drying phases of all rain events are classified according to the median value of the humidity during those drying phases.

It shows that drying phases with high humidity have an ECDF curve that has the same shape as a *J-shaped* rain curve, while those with medium and low humidities reassemble a no rain *S-shaped* curve.

They follow an order that intuitively makes sense with the more humid drying periods exhibiting corona resembling the behaviour of wet

conductors the most. Assuming the relative humidity to be monotone decreasing during the drying period, the median of the humidity during the drying phase is a proxy indicator of how fast the air gets drier in the first three hours after precipitation has stopped.

The clear distinction between the low, medium and high curves suggests that the arbitrary 3 hours chosen as the minimum inter-event time has its limits. Indeed, during this fixed period, after some events the line still shows a corona behaviour very close to a wet line, after others it more resembles that of fair weather. Setting the end of rain events not solely by time but also looking at when the corona current reaches pre-rain levels might show an even stronger correlation with relative humidity.

Day/night

Ambient temperature could also affect conductor drying, but two reasons make its analysis here of little relevance. Firstly, the conductors being unloaded, the results would not be applicable to real lines. Moreover, since the dataset covers seasons with large amplitudes in temperature, the warmest temperatures of a given drying period could still be lower than the lowest temperature of the drying of another rain event.

Unfortunately, the local weather station is not equipped with a solar radiation sensor, so rather than focus on solar radiation as a source of energy to dry the line, the currents are simply distinguished by day and night. The day and night phases are determined using the sun elevation calculated for the experiment's location and its sign is used directly. This results in the distributions of figure 15.13.

It shows that small currents are more often observed at night regardless of whether the line is wet or not. Larger currents have similar distribution for day and night unless the line is wet. Then, large currents are more numerous at night. This might suggest that as the sun hits the line and contributes to removing the water droplets on it, large current values are the first to diminish. However, the observations

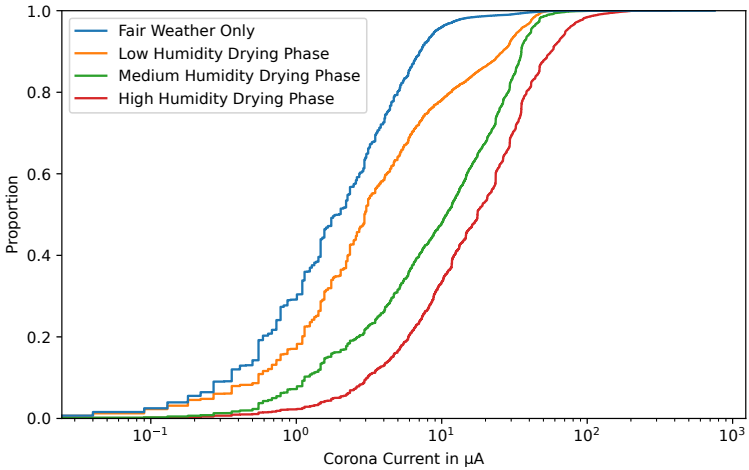

Figure 15.12: Currents binned according to the median relative humidity measured during the entirety of every drying phase. Each full drying phase falls in one of the three categories. Low median humidity is up to 80 %, medium up to 90 % and high up to 100 %. Fair weather curve for comparison.

made in section 14.3 regarding humidity's diurnal cycle is also at play here, affecting both the drying performance of the conductor and the discharge properties of the atmosphere.

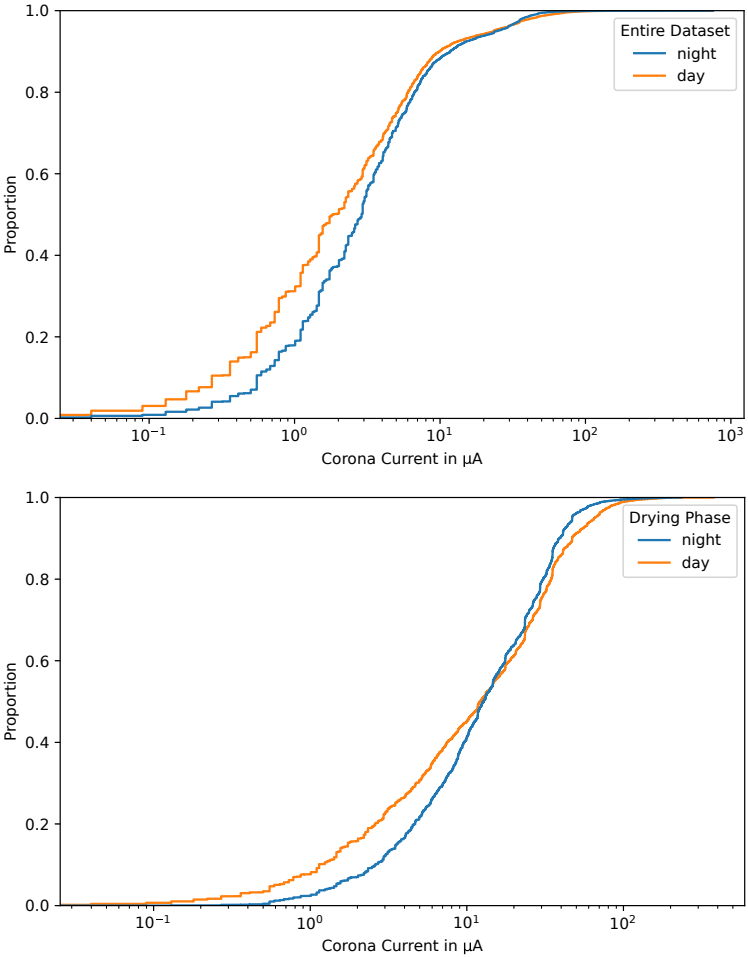

Figure 15.13: ECDFs for corona loss current during the day and night for (Top) the overall dataset and (bottom) during drying phases.

15.4 Conclusions

It has been decided in the present study to put an emphasis on *rain events* rather than precipitation metrics by themselves. The aim is thus not to say that if "such rain conditions are observed the corona performance will be like that", but rather "if an entire rain event has these characteristics, then corona performance will be like that".

Of course a rain event is characterized by precipitation metrics. But those defined here describe the entire event and are not limited to instantaneous values. Moreover, it was showed that precipitation metrics are not the only relevant quantities that determine corona behaviour during a rain event. In fact corona is affected by rain outside of periods where rain is measured, whether it be during precipitation pauses within the event, or the drying phase.

Lundquist (1984) notes that rain distribution from one "short-term" test can differ considerably from that of another. In the cited publication's context "short-term" means the duration of what here is called a rain event. He then goes on to say that "when the conductor is completely wet" results should nevertheless be reproducible for comparable rain rates.

The rather weak intensity rain events recorded and the apparent lack of trend when isolating events in figures 15.5 and 15.6 suggests that the above hypothesis can not necessarily be guaranteed or at least might not be sufficient.

Part VI

Conclusions and Outlook

Chapter 16

Conclusions and Outlook

16.1 Conclusions

The introduction of this thesis and especially chapter 3 detailed the diversity of approaches that exist with regard to research on overhead line corona. This work introduced new tools, whether they be measurement tools or analysis tools and highlighted corona characteristics that are specific to a geographic region precisely by embracing this diversity.

It shows results ranging different scales. Scales in the level of detail that is investigated, from single water droplets to full-size outdoor overhead lines. Scales in duration of experiments, from the deformation of droplets within milliseconds to test lines energized during months. Scales in the condition of the conductor, from completely dry to completely wet and the entire transient behaviour in between.

The tools introduced are manifold as well. They include novel sensors, visualizations, and metrics that are all meant to make long-term continuous outdoor measurements easier. This is required to imagine being able to monitor corona effects over large geographic regions and thus obtain a more complete picture of how local climatic and

environmental parameters affect them.

Single water drops and their deformation depending on surface properties were studied. As expected from what is observed when comparing old and new conductors, it was shown that generally more hydrophilic surfaces make droplets more difficult to deform with an electric field. This in turn means that a higher background field strength is needed for a discharge to occur from a droplet's tip. On the other hand, on more hydrophobic surfaces the critical background field for corona onset is lower. Partial discharges from water droplets occur because of a positive feedback loop between the increasingly pointy droplet tip and the increasing electric forces around this tip leading to the fulfilment of the streamer criterion. The dependency of the onset field strength on droplet volume was also shown.

However, it was also exposed that the static contact angle is not a sufficient metric to determine how likely it is for a surface to have coronating droplets. Indeed, droplets on highly slippery super hydrophobic surface, i.e. those surfaces with both a large static contact angle and a small contact angle hysteresis, can lift-off without being deformed enough to cause any discharge.

All those results were obtained experimentally as well as from predictive simulation models.

A unified corona sensor platform was developed using the IoT technologies relevant for corona research. This platform allows a much lower cost and logistically easier deployment of a large number of sensors. A single gateway hub saves data from common satellite nodes that have heterogeneous sensing capabilities. Sensors for corona loss current, ion current density and electric field at ground level were implemented. The low energy performance of the platform was demonstrated making uninterrupted long-term experiments viable, even with sensors that have to be on high potential.

The complementarity of the different corona effects measured using this platform was shown. The sensors allowed to easily discriminate conductors with different corona performance. Moreover, using the

smart processing capabilities of the sensor nodes, it is investigated what representations of a highly dynamic raw signal allow distinguishing patterns important for the evaluation of long-term corona characteristics while keeping the amount of data saved at reasonable levels.

A new method for representing traditional partial measurement data useful during weather transients was introduced. An important potential application for it are long-term HVDC measurements.

The long-term measurements performed during this thesis principally focused on the corona loss current. Corona loss current data captured over several months was analysed using empirical cumulative distribution functions to show the full extent of the recorded data, which generally spans several orders of magnitude.

Wet weather corona was studied by first defining rain events and rain rate metrics. Precipitation characteristics of those rain events are used to classify corona behaviour. At several points in this thesis, an emphasis is also put on the drying phase after a line is actively wetted as being an important consideration when describing wet weather corona.

Observations are also made on fair weather corona, for instance with regard to correlations with humidity and wind.

The results are compared with reports found in literature for other geographic regions. In light of that, it is discussed what corona characteristics might be seen as specific to a place.

16.2 Outlook

While many of the results presented are specific to the climate and environment of the experiments, and may even be specific to the particular test setup, the tools and methods introduced are valid everywhere.

The investigation on single droplets and surface properties allows a

better understanding of fundamental interactions of different conductors and the corona sources they are subjected to. However, the droplet scale alone is not enough to fully explain the different behaviours observed. If modern surface engineering is to be used to manufacture overhead conductors less prone to corona, further research is needed.

The unified sensor platform that was introduced was designed with modularity in mind. The same platform is already being used for completely different applications such as the for the predictive maintenance of switchgear. But there are still other corona effects for which it could also be expanded. In particular audible noise emissions would hugely benefit from the ability to place the sensor on high potential as closely to the coronating protrusions as possible.

Even with the tools available, the task of actually collecting data in various geographic locations over several years remains significant. But just as literature has suggested until now, this work tends to indicate that this task is still necessary today. A big difference being that modern technologies make this much more feasible than in the past. The results presented here are meant to facilitate such measurement campaigns and to allow drawing more meaningful conclusions from the collected data.

This should ultimately help a better planing of new overhead lines or the uprating of existing ones, but also accelerate permitting processes. As such, corona research contributes to the build-up of transmission capacity needed to make the world's electricity grids suited for the energy transition.

Appendix A

Single Droplet Models

Details for models used in chapter 9 using the same nommenclature as in the main text.

A.1 Numerical model for droplet deformation

Here, the implementation made for this work of the algorithm presented by Glière, Roux, and Achard (2013) is descirbed. The symmetry of the problem allows us to work in cylindrical (r, z) coordinates. The drop shape is parametrized as the arc length measured from the drop apex. The calculation of the droplet's shape is based on the augmented Young-Laplace equation:

$$\gamma \nabla \cdot \mathbf{n} = -(\rho_{\text{water}} - \rho_{\text{air}}) g z + \Delta p + \frac{\varepsilon}{2} (\mathbf{E} \cdot \mathbf{n})^2. \tag{A.1}$$

As shown elsewhere (Glière, Roux, and Achard 2013; Myshkis et al. 1987), this can be re-written as

$$r'' = z'[\frac{1}{\gamma}[(\rho_{\text{water}} - \rho_{\text{air}})gz + \Delta p - \frac{\varepsilon}{2}(\mathbf{E}\cdot\mathbf{n})^2] - \frac{z'}{r}] \tag{A.2}$$

$$z'' = -r'[\frac{1}{\gamma}[(\rho_{\text{water}} - \rho_{\text{air}})gz + \Delta p - \frac{\varepsilon}{2}(\mathbf{E}\cdot\mathbf{n})^2] - \frac{z'}{r}]. \tag{A.3}$$

everywhere except for the apex where z'=0

$$r'' = \frac{z'}{2}[(\rho_{\text{water}} - \rho_{\text{air}})gz + \Delta p - \frac{\varepsilon}{2}(\mathbf{E}\cdot\mathbf{n})^2] \tag{A.4}$$

$$z'' = \frac{-r'}{2}[(\rho_{\text{water}} - \rho_{\text{air}})gz + \Delta p - \frac{\varepsilon}{2}(\mathbf{E}\cdot\mathbf{n})^2]. \tag{A.5}$$

The prime symbol indicates differentiation with respect to the arc length. In the absence of electric field, the term $\frac{\varepsilon}{2}(\mathbf{E}\cdot\mathbf{n})^2$ is omitted from equations (A.2)-(A.5).

For a given set of apex height z_{apex}, pressure difference Δp and electric field values along the drop shape $\mathbf{E}$, equations (A.2)-(A.5) will give a drop shape if the latter is physically possible. MATLAB and a Runge-Kutta solver are used to integrate these equations.

The shapes obtained solving the ordinary differential equations (A.2)-(A.5) have a given volume Ω and contact disc radius r that can be compared to target values. Subsequently, a simple optimizer minimizes the root-mean-square error between the computed volume and contact disc and the target values by adjusting the apex height and excess pressure. Figure A.1 shows a flow chart of the full algorithm through which drop shapes are numerically obtained.

The electric field along the drop shape at each iteration is computed using finite element method (FEM) in Comsol.

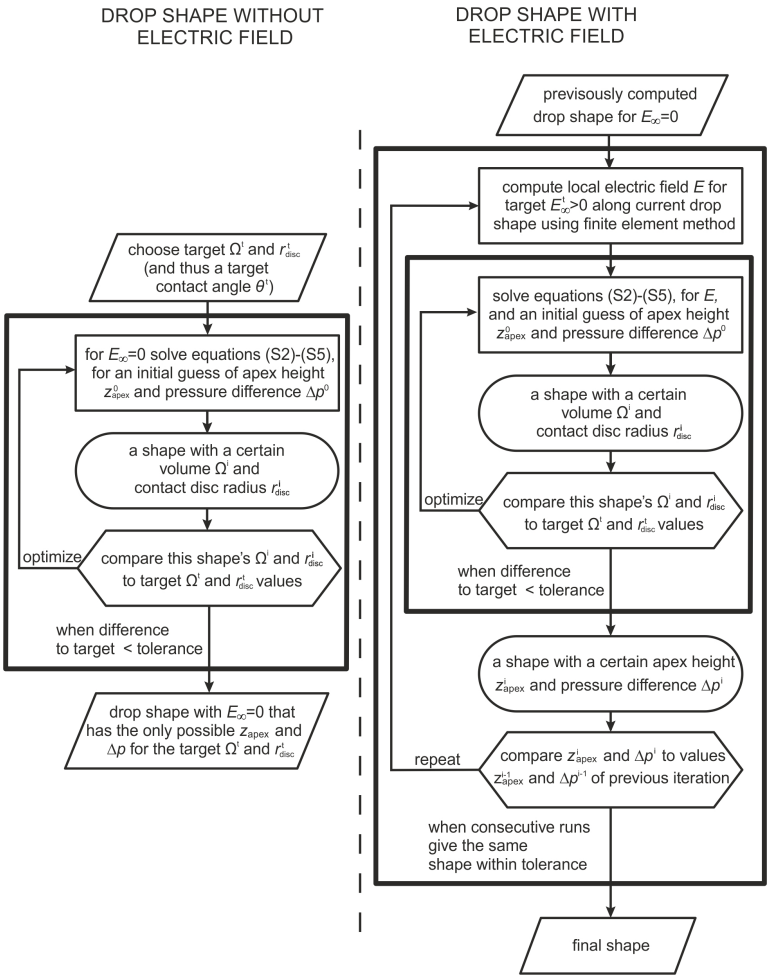

Figure A.1: **Flowchart describing the algorithm.** First, the drop shape in the absence of any electric field has to be computed (left). This shape is then used to compute a drop shape deformed by a given background electric field (right). All of the steps are performed in MATLAB except for the local field calculation along the drop surface for which Comsol is used.

A.2 Droplet lift-off

The derivation of the critical applied electric field $E_{\infty,\mathrm{cr}}$ is based on a force balance where the electrostatic force F_{el} resulting from the applied electric field, the buoyant force F_b,the gravitational force F_g, the force F_c due to intefacial interactions between surface and droplet and the force F_p due to Δp (Glière, Roux, and Achard 2013) are considered. The overall force balance at the droplet (figure A.2) is described by the following equation:

$$\underbrace{\rho_{\mathrm{water}}\Omega g}_{F_g} + \underbrace{2\pi r_{\mathrm{disc}}\sin(\theta)}_{F_c} = \underbrace{\rho_{\mathrm{air}}\Omega g}_{F_b} + \underbrace{\Delta p \pi r_{\mathrm{disc}}^2}_{F_p} + F_{\mathrm{el}}. \tag{A.6}$$

With increasing E_∞ the radius of droplet's contact disc (figure A.2) decreases and marginally before droplet lift-off $r_{\mathrm{disc}} \approx 0$ (Figure S4c). Therefore, the force due to interfacial interactions between surface and droplet is $F_{\mathrm{c}} \approx 0$ and the force due to the pressure difference $\Delta p = p_{\mathrm{water}} - p_{\mathrm{air}}$ between the drop and the surrounding air at $z = 0$ is $F_{\mathrm{p}} \approx 0$ (Lebedev and Skal'skaya 1962; Roux, Achard, and Fouillet 2008). Based on the aforementioned conditions, equation (A.6) is formulated

$$F_{\mathrm{el}} = (\rho_{\mathrm{water}} - \rho_{\mathrm{air}})\,\Omega\, g. \tag{A.7}$$

Furthermore, it is assumed that the droplet is conductive and its deformation at the moment of lift-off has a negligible influence in the estimation of the electrostatic force proposed by Lebedev and Skal'skaya (1962). Thus, the electrostatic force F_{el} is estimated

$$F_{\mathrm{el}} = 4\pi\varepsilon_0 E_{\infty,\mathrm{cr}}^2 r_{\mathrm{eq}}^2 \left(\zeta(3) + \frac{1}{6}\right), \tag{A.8}$$

where r_{eq} is the equivalent droplet radius assuming that the droplet at the instant of lift-off attains a spherical shape and is given by the following equation

$$r_{\mathrm{eq}} = \left(\frac{3\Omega}{4\pi}\right)^{\frac{1}{3}}. \tag{A.9}$$

Combining equations (A.7), (A.8) and (A.9) and reordering all the variables involved the estimation of $E_{\infty,\mathrm{cr}}$ for droplet lift-off is obtained.

$$E_{\infty,\,\mathrm{cr}} = \left(\frac{(\rho_{\mathrm{water}} - \rho_{\mathrm{air}})g}{6^{2/3}\pi^{1/3}\varepsilon(\zeta(3) + \frac{1}{6})}\right)^{1/2} \Omega^{1/6}. \tag{A.10}$$

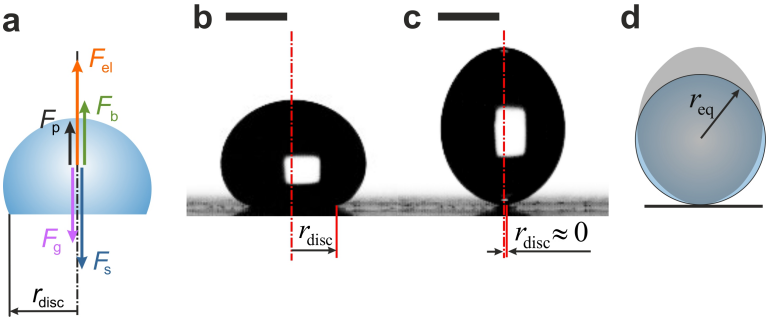

Figure A.2: **Geometrical considerations for the prediction of droplet lift-off.** **a**, Force balance on a droplet before lift-off. **b**, Contact disc radius r_{disc} of a 40 µL droplet. **c**, Marginally before lift-off droplet's contact disc radius becomes $r_{disc} \approx 0$. **d**, Sphere of radius r_{disc} and the same volume (40 µL) with the deformed droplet (superimposed black translucent shape) marginally before lift-off. Scale bars correspond to 2 mm.

Appendix B

Time Series with Humidity

Additional figures for section 14.3. The caption of figure 14.4 applies for all figures in this appendix: (top) relative humidity, (middle) corona current and (bottom) dew point in orange and daily minimal temperature in blue. Note that during rain events, the current is plotted in green while it is blue otherwise.

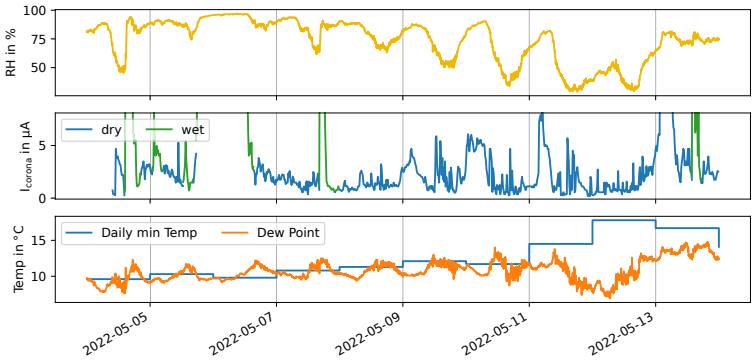

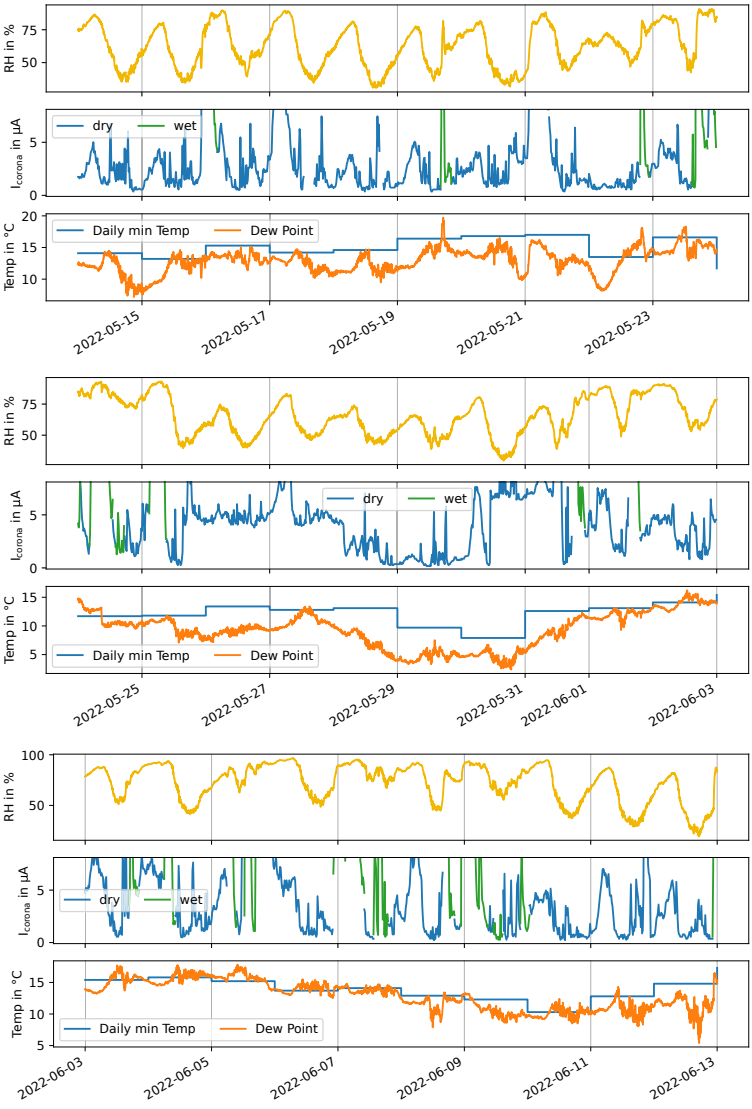
RH in %
75
50
I_{corona} in µA
dry
wet
5
0
Temp in °C
20
15
10
Daily min Temp
Dew Point
2022-05-15
2022-05-17
2022-05-19
2022-05-21
2022-05-23
RH in %
75
50
I_{corona} in µA
dry
wet
5
0
Temp in °C
15
10
5
Daily min Temp
Dew Point
2022-05-25
2022-05-27
2022-05-29
2022-05-31
2022-06-01
2022-06-03
RH in %
100
50
I_{corona} in µA
dry
wet
5
0
Temp in °C
15
10
5
Daily min Temp
Dew Point
2022-06-03
2022-06-05
2022-06-07
2022-06-09
2022-06-11
2022-06-13

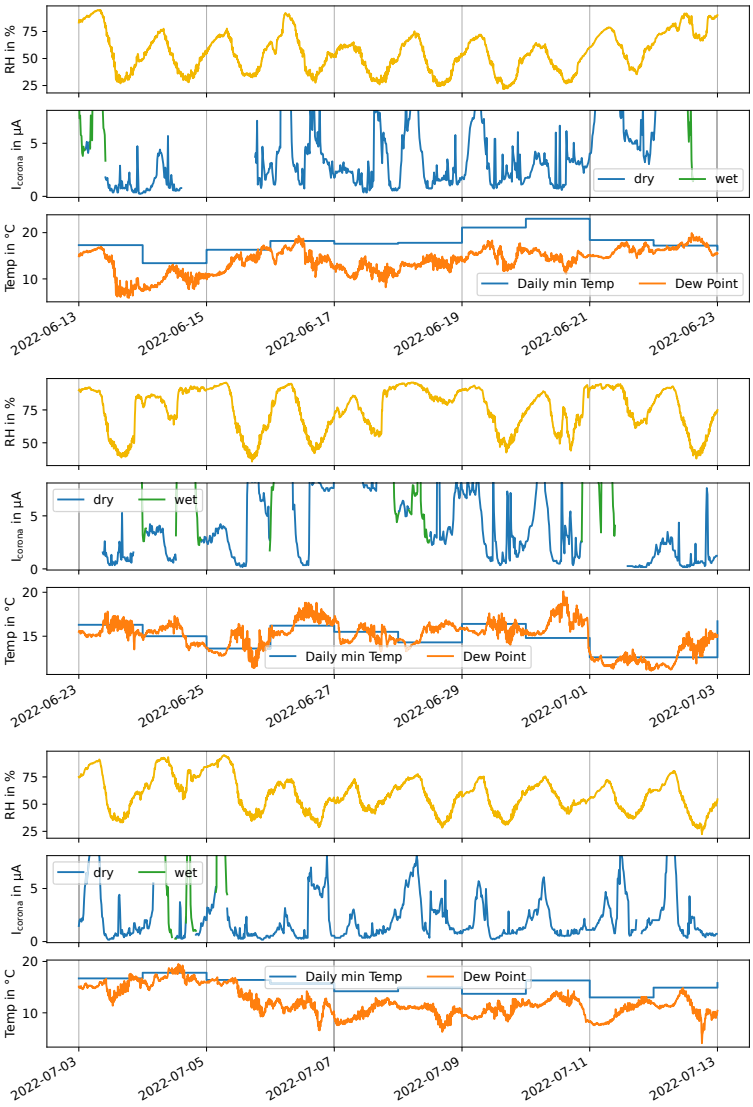
RH in %
75
50
25
I_{corona} in µA
5
0
dry
wet
Temp in °C
20
10
Daily min Temp
Dew Point
2022-06-13
2022-06-15
2022-06-17
2022-06-19
2022-06-21
2022-06-23
RH in %
75
50
I_{corona} in µA
dry
wet
5
0
Temp in °C
20
15
Daily min Temp
Dew Point
2022-06-23
2022-06-25
2022-06-27
2022-06-29
2022-07-01
2022-07-03
RH in %
75
50
25
I_{corona} in µA
dry
wet
5
0
Temp in °C
20
10
Daily min Temp
Dew Point
2022-07-03
2022-07-05
2022-07-07
2022-07-09
2022-07-11
2022-07-13

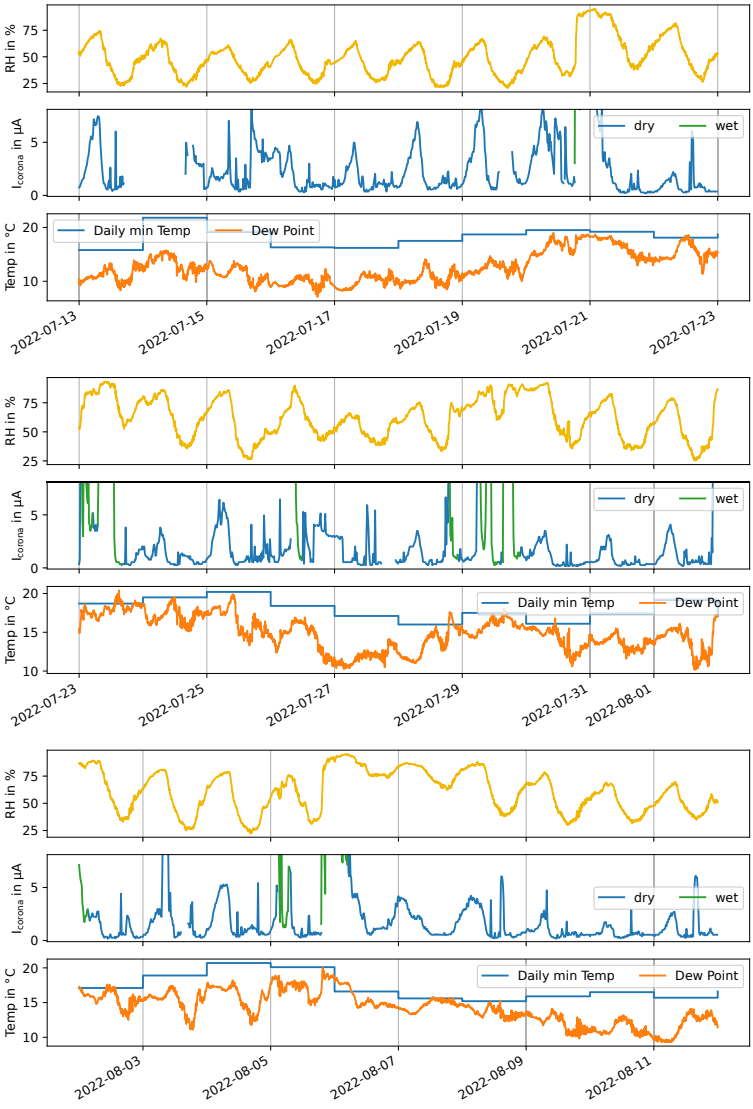
RH in %
75
50
25
I_{corona} in µA
5
0
dry
wet
Temp in °C
20
10
Daily min Temp
Dew Point
2022-07-13
2022-07-15
2022-07-17
2022-07-19
2022-07-21
2022-07-23
RH in %
75
50
25
I_{corona} in µA
5
0
dry
wet
Temp in °C
20
15
10
Daily min Temp
Dew Point
2022-07-23
2022-07-25
2022-07-27
2022-07-29
2022-07-31
2022-08-01
RH in %
75
50
25
I_{corona} in µA
5
0
dry
wet
Temp in °C
20
15
10
Daily min Temp
Dew Point
2022-08-03
2022-08-05
2022-08-07
2022-08-09
2022-08-11

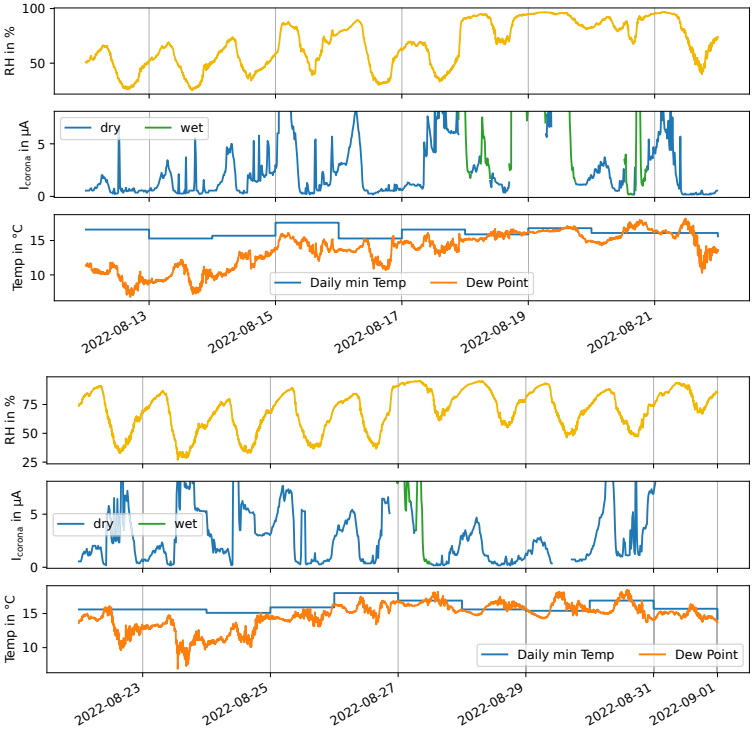
RH in %
100
50
dry
wet
I_{corona} in µA
5
0
Temp in °C
15
10
Daily min Temp
Dew Point
2022-08-13
2022-08-15
2022-08-17
2022-08-19
2022-08-21
RH in %
75
50
25
dry
wet
I_{corona} in µA
5
0
Temp in °C
15
10
Daily min Temp
Dew Point
2022-08-23
2022-08-25
2022-08-27
2022-08-29
2022-08-31
2022-09-01

Bibliography

Alassi, A. et al. (Sept. 2019). “HVDC Transmission: Technology Review, Market Trends and Future Outlook”. In: *Renewable and Sustainable Energy Reviews* 112, pp. 530–554. DOI: 10.1016/J.RSER.2019.04.062.

Allard, S. et al. (Mar. 2020). “European transmission grid expansion as a flexibility option in a scenario of large scale variable renewable energies integration”. In: *Energy Economics* 87, p. 104733. DOI: 10.1016/j.eneco.2020.104733.

Amano, Y. and Sunaga, Y. (Apr. 1989). “Study on reduction in electric field, charged voltage, ion current and ion density under HVDC transmission lines by parallel shield wires”. In: *IEEE Transactions on Power Delivery* 4 (2), pp. 1351–1359.

Anderson, J. G., Baretsky, M., and MacCarthy, D. D. (Dec. 1966). “Corona-Loss Characteristics of EHV Transmission Lines Based on Project EHV Research”. In: *IEEE Transactions on Power Apparatus and Systems* PAS-85 (12), pp. 1196–1212. DOI: 10.1109/TPAS.1966.291639.

Anderson, J. and Zaffanella, L. (Jan. 1972). “Project UHV Test Line Research on the Corona Performance of a Bundle Conductor at 1000 kV”. In: *IEEE Transactions on Power Apparatus and Systems* PAS-91 (1), pp. 223–232. DOI: 10.1109/TPAS.1972.293334.

Bailey, B. (Oct. 1967). “Progress Report on BPA HV DC Test Line Radio Noise and Corona Loss”. In: *IEEE Transactions on Power Appara-*

tus and Systems PAS-86 (10), pp. 1141–1145. DOI: 10.1109/TPAS.1967.291865.

Bailey, B. (Sept. 1970). "Test Line Experience with HVDC Overhead Transmission". In: *IEEE Transactions on Power Apparatus and Systems* PAS-89 (7), pp. 1625–1634. DOI: 10.1109/TPAS.1970.292810.

Ballerini, M. et al. (2019). "Experimental evaluation on NB-IoT and LoRaWAN for industrial and IoT applications". In: *2019 IEEE 17th International Conference on Industrial Informatics (INDIN)*. Vol. 1. IEEE, pp. 1729–1732.

Bansal, G. et al. (2019). "SmartChain: a smart and scalable blockchain consortium for smart grid systems". In: *2019 IEEE International Conference on Communications Workshops (ICC Workshops)*. IEEE, pp. 1–6.

Basaran, O. A. and Scriven, L. E. (May 1989). "Axisymmetric shapes and stability of isolated charged drops". In: *Physics of Fluids A: Fluid Dynamics* 1.5, pp. 795–798. DOI: 10.1063/1.857551.

Basaran, O. A. and Scriven, L. (Nov. 1990). "Axisymmetric shapes and stability of pendant and sessile drops in an electric field". In: *Journal of Colloid and Interface Science* 140.1, pp. 10–30. DOI: 10.1016/0021-9797(90)90316-G.

Berendsen, H. J. C. (Apr. 2011). *A Student's Guide to Data and Error Analysis*. Cambridge University Press. DOI: 10.1017/CBO9780511921247.

Betts, A. (2015). *Diurnal Cycle*. Vol. Encyclopedia of Atmospheric Sciences. Elsevier. DOI: 10.1016/B978-0-12-382225-3.00135-3.

Beyer, M. et al. (1986). *Hochspannungstechnik*. Springer Berlin Heidelberg. DOI: 10.1007/978-3-642-61633-4.

Bleuler, P. and Franck, C. M. (in preparation). "Rain Event and Metric Dependency of Wet Weather Corona in HVDC Overhead Lines". In: *IEEE Transactions on Power Delivery*.

Bleuler, P., Hedtke, S., and Franck, C. M. (2020). "Corona Performance of DC Overhead Lines in Outdoor Experiments During Wet Weather Transitions and under Varying Humidity". In: *CIGRE Session, Paris*.

Bleuler, P., Xiao, Y., et al. (submitted). “A Unified Sensor Platform for Investigating Corona Effects on Overhead Lines”. In: *IEEE Transactions on Instrumentation and Measurement*.

Bracken, T. D., Capon, A. S., and Montgomery, D. V. (Mar. 1978). “Ground Level Electric Fields and Ion Currents on the Celilo-Sylmar 400 kV DC Intertie During Fair Weather”. In: *IEEE Transactions on Power Apparatus and Systems* PAS-97 (2), pp. 370–378.

Cao, Y., Liu, Z., and Wu, L. (Nov. 2021). “Bluetooth Low Energy Error Correction Based on Convolutional Coding”. In: *Journal of Physics: Conference Series* 2093.1, p. 012033. DOI: 10.1088/1742-6596/2093/1/012033.

Carbone, M. et al. (Dec. 2014). “Minimum Inter-Event Time to Identify Independent Rainfall Events in Urban Catchment Scale”. In: *Advanced Materials Research* 1073-1076, pp. 1630–1633. DOI: 10.4028/www.scientific.net/AMR.1073-1076.1630.

Cecelja, F., Bordovsky, M., and Balachandran, W. (Apr. 2002). “Electro-optic sensor for measurement of DC fields in the presence of space charge”. In: *IEEE Transactions on Instrumentation and Measurement* 51 (2), pp. 282–286. DOI: 10.1109/19.997825.

Chalmers, J. A. (1962). “The measurement of the vertical electric current in the atmosphere”. In: *Journal of Atmospheric and Terrestrial Physics* 24 (4), pp. 297–302.

Chang, J.-S., Lawless, P., and Yamamoto, T. (1991). “Corona discharge processes”. In: *IEEE Transactions on Plasma Science* 19 (6), pp. 1152–1166. DOI: 10.1109/27.125038.

Chartier, V. L., Lee, L. Y., et al. (1987). “Effect of High Altitude on High Voltage AC Transmission Line Corona Phenomena”. In: *IEEE Transactions on Power Delivery* 2 (1), pp. 225–237.

Chartier, V. L., Shankie, D., and Kolcio, N. (1970). “The Apple Grove 750-kV Project: Statistical Analysis of Radio Influence and Corona-Loss Performance of Conductors at 775 kV”. In: *IEEE Transactions on Power Apparatus and Systems* PAS-89 (5), pp. 867–881.

Chartier, V. L. and Stearns, R. (Jan. 1981). “Formulas for Predicting Audible Noise from Overhead High Voltage AC and DC Lines”. In: *IEEE*

Transactions on Power Apparatus and Systems PAS-100 (1), pp. 121–130. DOI: 10.1109/TPAS.1981.316894.

Chen, B., Bleuler, P., et al. (in preparation). "The Influence of Dielectric Film with Different Resistivities on the Ion Flow Field Under HVDC Overhead Lines". In: *IEEE Transactions on Dielectrics and Electrical Insulation*.

Chen, B., Lu, T., and Wang, D. (Jan. 2020). "Analysis of Ion Flow Field Considering Dielectric Film Under HVDC Overhead Transmission Lines". In: *IEEE Transactions on Magnetics* 56 (1), pp. 1–4. DOI: 10.1109/TMAG.2019.2951155.

Christakou, N. et al. (2022). *Renewable-energy development in a net-zero world: Land, permits, and grids*. Tech. rep. McKinsey & Company.

CIGRE SC B2 (2017). *Overhead Lines, CIGRE Green Books*. Ed. by K. O. Papailiou. Springer International Publishing. DOI: 10.1007/978-3-319-31747-2.

CIGRE WG 36.01 (1974). *Addendum to Technical Brochure 61: Interferences Produced by Corona Effects of Electric Systems*.

CIGRE Working Group B2.41 (2014). *Technical Brochure 583: Guide to the Conversion of Existing AC Lines to DC Operation*. CIGRE.

Comber, M. and Zaffanella, L. (Jan. 1974). "The Use of Single-Phase Overhead Test Lines and Test Cages to Evaluate the Corona Effects of EHV and UHV Transmission Lines". In: *IEEE Transactions on Power Apparatus and Systems* PAS-93 (1), pp. 81–90. DOI: 10.1109/TPAS.1974.293918.

Comber, M. and Johnson, G. (July 1982). "HVDC Field and Ion Effects Research at Project UHV: Results of Electric Field and Ion Current Measurements". In: *IEEE Transactions on Power Apparatus and Systems* PAS-101 (7), pp. 1998–2006. DOI: 10.1109/TPAS.1982.317447.

Comber, M. G. and Humphreys, D. R. (1979). "HVDC Testing at Project UHV". In: *7 IEEE/PES Transmission and Distribution Conference and Exposition, 1979*. IEEE, pp. 80–88.

Comber, M. G., Kotter, F., and McKnight, R. (1983). "Experimental Evaluation of Instruments for Measuring DC Transmission

Line Electric Fields and ION Currents". In: *IEEE Transactions on Power Apparatus and Systems* PAS-102 (11), pp. 3549–3557. DOI: 10.1109/TPAS.1983.317700.

Comber, M. G. and Nigbor, R. (1976). "Audible noise performance of the first three-phase ultra-high voltage transmission test line at EPRI's Project UHV". In: *IEEE Transactions on Power Apparatus and Systems* 95 (4), pp. 1105–1114.

Corbellini, U. and Pelacchi, P. (July 1996). "Corona losses in HVDC bipolar lines". In: *IEEE Transactions on Power Delivery* 11 (3), pp. 1475–1481. DOI: 10.1109/61.517506.

Cortina, R. et al. (1980). "Results of measurements of corona effects (loss, radio-interference, audible noise) on large conductor bundles and large diameter tubes". In: *CIGRE Session* (36-03).

Cui, Y. et al. (Jan. 2018). "Model, Design, and Testing of Field Mill Sensors for Measuring Electric Fields Under High-Voltage Direct-Current Power Lines". In: *IEEE Transactions on Industrial Electronics* 65 (1), pp. 608–615.

Dekking, F. M. et al. (2005). *A Modern Introduction to Probability and Statistics*. Springer London. DOI: 10.1007/1-84628-168-7.

Doyu, H., Morabito, R., Höller, J., et al. (2020). "Bringing machine learning to the deepest IoT edge with TinyML as-a-service". In: *IEEE IoT Newsletter* 11.

Duft, D. et al. (2003). "Coulomb fission: Rayleigh jets from levitated microdroplets". In: *Nature* 421.6919, p. 128. DOI: 10.1038/421128a.

Dunkerley, D. (Dec. 2008). "Identifying individual rain events from pluviograph records: a review with analysis of data from an Australian dryland site". In: *Hydrological Processes* 22 (26), pp. 5024–5036. DOI: 10.1002/hyp.7122.

Egli, F., Steffen, B., and Schmidt, T. S. (Dec. 2018). "A dynamic analysis of financing conditions for renewable energy technologies". In: *Nature Energy* 3 (12), pp. 1084–1092. DOI: 10.1038/s41560-018-0277-y.

Elahi, H. et al. (2020). "Energy harvesting towards self-powered IoT devices". In: *Energies* 13.21, p. 5528.

Engelen, J. et al. (2012). “Ermittlung und Beurteilung von Koronageräuschen an Höchstspannungsfreileitungen”. In: *Lärmbekämpfung* 6 (4), pp. 1–16.

EPRI (1993). *HVDC Transmission Line Reference Book*. EPRI.

EPRI (2005). *EPRI AC Transmission Line Reference Book - 200 kV and Above, Third Edition*. 3rd, pp. 1–1074.

Fang, C. et al. (July 2013). “Impact Factors in Measurements of Ion-Current Density Produced by High-Voltage DC Wire’s Corona”. In: *IEEE Transactions on Power Delivery* 28 (3), pp. 1414–1422.

Färber, R. et al. (in preparation). “Breakdown inception modelling of quasi-uniform gas gaps with metallic or dielectric boundaries under transient voltages”. In: *Journal of Physics D: Applied Physics*.

Farhan, L. et al. (2018). “A concise review on Internet of Things (IoT)-problems, challenges and opportunities”. In: *2018 11th International Symposium on Communication Systems, Networks & Digital Signal Processing (CSNDSP)*, pp. 1–6.

Franck, C. M. et al. (2023). “Intelligent Maintenance of T&D Equipment”. In: *IEEE Power & Energy Magazine* 21.2, pp. 18–29. DOI: 10.1109/MPE.2022.3230968.

Fukushima, M., Tanabe, K., and Nakano, Y. (1987). “Prediction Method and Subjective Evaluation of Audible Noise Based on Results at the Shiobara HVDC Test Line”. In: *IEEE Transactions on Power Delivery* 2 (4), pp. 1170–1176. DOI: 10.1109/TPWRD.1987.4308239.

Galliker, P. et al. (Jan. 2012). “Direct printing of nanostructures by electrostatic autofocussing of ink nanodroplets.” In: *Nature communications* 3.May, p. 890. DOI: 10.1038/ncomms1891.

Gallina, L. (2022a). “A Practical Smart Sensor Used for the Long-Term Monitoring of Corona Currents on Overhead Lines”. Master’s Thesis. ETH Zürich.

Gallina, L. (2022b). “Optimizations and Applications of an IoT Smart Sensor to Monitor Corona Currents on Overhead Lines”. Semester Project. ETH Zürich.

Gallo, C. F., Germanos, J. E., and Courtney, J. E. (Jan. 1969). “The Effect of Humidity and Temperature Variations on the Behavior of Wire-

to-Plane Coronas". In: *Applied Optics* 8 (S1), p. 111. DOI: 10.1364/AO.8.S1.000111.

Gañán-Calvo, A. M., Rebollo-Muñoz, N., and Montanero, J. M. (2013). "The minimum or natural rate of flow and droplet size ejected by Taylor cone-jets: Physical symmetries and scaling laws". In: *New Journal of Physics* 15. DOI: 10.1088/1367-2630/15/3/033035.

Gary, C. and Moreau, M. (1976). *L'Effet de couronne en tension alternative : pertes et perturbations radioélectriques engendrées par les lignes de transport d'énergie électrique*. Collection de la Direction des Etudes et Recherches d'Electricité de France no. 24. Paris: Eyrolles.

Gehrig, E. H. et al. (Mar. 1967). "Bonneville Power Administration's 1100-kV Direct Current Test Project: II - Radio Interference and Corona Loss". In: *IEEE Transactions on Power Apparatus and Systems* PAS-86 (3), pp. 278–290. DOI: 10.1109/TPAS.1967.291954.

Glière, A., Roux, J. M., and Achard, J. L. (2013). "Lift-off of a conducting sessile drop in an electric field". In: *Microfluidics and Nanofluidics* 15.2, pp. 207–218. DOI: 10.1007/s10404-013-1144-6.

Grams, C. M. et al. (Aug. 2017). "Balancing Europe's wind-power output through spatial deployment informed by weather regimes". In: *Nature Climate Change* 7 (8), pp. 557–562. DOI: 10.1038/nclimate3338.

Guillod, T., Pfeiffer, M., and Franck, C. M. (Dec. 2014). "Improved Coupled Ion-Flow Field Calculation Method for AC/DC Hybrid Overhead Power Lines". In: *IEEE Transactions on Power Delivery* 29 (6), pp. 2493–2501. DOI: 10.1109/TPWRD.2014.2322052.

Hagelaar, G. J. M. and Pitchford, L. C. (Nov. 2005). "Solving the Boltzmann equation to obtain electron transport coefficients and rate coefficients for fluid models". In: *Plasma Sources Science and Technology* 14 (4), pp. 722–733. DOI: 10.1088/0963-0252/14/4/011.

He, W. et al. (July 2017). "Effect of Altitude on the Audible Noise Level of AC Power lines". In: *Energies* 10 (7), p. 1055. DOI: 10.3390/en10071055.

Hedtke, S., Bleuler, P., and Franck, C. M. (Dec. 2021). "Outdoor Investigation of the Corona Characteristics and Audible Noise of a Hybrid

AC/DC Overhead Line". In: *IEEE Transactions on Power Delivery* 36 (6), pp. 3309–3317. DOI: 10.1109/TPWRD.2020.3038414.

Hedtke, S., Pfeiffer, M., Franck, C. M., Zaffanella, L., et al. (2015). "Audible noise of hybrid AC / DC overhead lines : Comparison of different prediction methods and conductor arrangements". In: *EPRI HVDC & FACTS Conference*.

Hedtke, S., Pfeiffer, M., Franck, C. M., Dermont, C., et al. (2018). "HVDC & hybrid HVAC/HVDC overhead line conversion: An acceptance case study". In: *CIGRE Session*.

Hedtke, S., Pfeiffer, M., Gobeli, M., et al. (2018). "Setup of an Outdoor Hybrid AC / DC Test Line for Corona Measurements". In: *VDE-Hochspannungstechnik, ETG-Fachberichte*.

Hedtke, S., Xu, P., et al. (Apr. 2020). "HVDC Corona Current Characteristics and Audible Noise During Wet Weather Transitions". In: *IEEE Transactions on Power Delivery* 35 (2), pp. 1038–1047. DOI: 10.1109/TPWRD.2019.2936285.

Heller, A. (2016). "Outdoor Measurement Concept for HVAC / HVDC Corona Effects". Master's Thesis. ETH Zürich.

Higashiyama, Y., Yanase, S., and Sugimoto, T. (July 2002). "DC corona discharge from water droplets on a hydrophobic surface". In: *Journal of Electrostatics* 55.3-4, pp. 351–360. DOI: 10.1016/S0304-3886(01)00217-0.

Hirsch, F. and Schafer, E. (July 1969). "Progress Report on the HVDC Test Line of the 400 kV-Forschungsgemeinschaft: Corona Losses and Radio Interference". In: *IEEE Transactions on Power Apparatus and Systems* PAS-88 (7), pp. 1061–1069. DOI: 10.1109/TPAS.1969.292506.

Hoek, S. (2017). *Application Note 17011: Using the Matlab file Export of the MPD 600*. Tech. rep. Omicron.

Hofmann, H., Kafadar, K., and Wickham, H. (2011). *Letter-value plots: Boxplots for large data*. Tech. rep. had.co.nz.

Hu, Q. et al. (May 2014). "Influence of air pressure and humidity on positive direct current corona discharge performances of the conductor in a corona cage". In: *International Transactions on Electrical Energy Systems* 24 (5), pp. 723–735. DOI: 10.1002/etep.1732.

HVLBuzz (2017). https://gitlab.com/ethz_hvl/hvlbuzz.

Hylten-Cavallius, N. and Train, D. (1974). "The IREQ Ultra High Voltage Laboratory and Test Facilities". In: *IEEE Transactions on Power Apparatus and Systems* PAS-93.1, pp. 176–186. DOI: 10.1109/TPAS.1974.293930.

IEC (2000). *International Standard 60270 High-Voltage Test Techniques – Partial Discharge Measurements Techniques*. Tech. rep. IEC.

IEEE (1990). *IEEE Guide for the Measurement of DC Electric-Field Strength and Ion Related Quantities*.

IPCC (2021). "IPCC, 2021: Summary for Policymakers". In: *Climate Change 2021: The Physical Science Basis. Contribution of Working Group I to the Sixth Assessment Report of the Intergovernmental Panel on Climate Change*.

IPCC (2022). "IPCC, 2022: Summary for Policymakers". In: *Climate Change 2022: Impacts, Adaptation, and Vulnerability. Contribution of Working Group II to the Sixth Assessment Report of the Intergovernmental Panel on Climate Change*. DOI: doi : 10 . 1017 / 9781009325844.001.

Jaworek, A. and Krupa, A. (1999). "Classification of the modes of EHD spraying". In: *Journal of Aerosol Science* 30.7, pp. 873–893. DOI: 10.1016/S0021-8502(98)00787-3.

Keller, M., Kundert, L., and Tettamanti, K. (2020). "Effect of Surface Wetting Behaviour on Discharges from Water Drops in Non- homogeneous Electric Fields Group Project". Group Project. ETH Zürich.

Khalifa, M. and Morris, R. (Mar. 1967). "A Laboratory Study of the Effects of Wind on DC Corona". In: *IEEE Transactions on Power Apparatus and Systems* PAS-86 (3), pp. 290–298. DOI: 10.1109/TPAS.1967.291955.

Kirchner, H. and Franck, C. M. (2022). "B2 PS3 11145 Correlation of the Surface Wettability and the Audible Noise Emission of Overhead Line Conductors". In: *CIGRE Session*.

Knudsen, N. and Iliceto, F. (1974). "Contribution to the Electrical Design of EHVDC Overhead Lines". In: *IEEE Transactions on Power Ap-*

paratus and Systems PAS-93.1, pp. 233–239. DOI: 10.1109/TPAS.1974.293937.

Korhonen, J. T. et al. (2013). "Reliable measurement of the receding contact angle". In: *Langmuir* 29.12, pp. 3858–3863. DOI: 10.1021/la400009m.

Kudyan, H. and H-Shih, C. (Mar. 1981). "A Nonlinear Circuit Model for Transmission Lines in Corona". In: *IEEE Transactions on Power Apparatus and Systems* PAS-100 (3), pp. 1420–1430. DOI: 10.1109/TPAS.1981.316617.

LaForest, J. et al. (Oct. 1963). "Radio Noise and Corona Loss Results from Project EHV". In: *IEEE Transactions on Power Apparatus and Systems* 82 (68), pp. 735–750. DOI: 10.1109/TPAS.1963.291403.

Larsen, M. L. and Teves, J. B. (2015). "Identifying Individual Rain Events with a Dense Disdrometer Network". In: *Advances in Meteorology* 2015, pp. 1–12. DOI: 10.1155/2015/582782.

Law, V. J. and Dowling, D. P. (2021). *The St Elmo's Fire: Its Formation and Measurement on Both Natural and Artificial Structures*. Springer, Cham. DOI: https://doi.org/10.1007/978-3-030-70795-8_34.

Lebedev, N. and Skal'skaya, I. P. (1962). "Forces and charges on an undeformable droplet in the DC field of a plate condenser". In: *Soviet Phys-Tech. Phys* 7, pp. 268–270.

Lekganyane, M., Ijumba, N., and Britten, A. (Oct. 2006). "Corona Audible Noise Measurements in a Small Indoor Corona Cage under HVDC Voltages". In: *2006 International Conference on Power System Technology*. IEEE, pp. 1–5. DOI: 10.1109/ICPST.2006.321753.

Li, B., Li, X., et al. (Sept. 2018). "Effect of humidity on dielectric breakdown properties of air considering ion kinetics". In: *Journal of Physics D: Applied Physics* 51 (37), p. 375201. DOI: 10.1088/1361-6463/aad5b9.

Li, D. and Xia, Y. (2004). "Electrospinning of nanofibers: Reinventing the wheel?" In: *Advanced Materials* 16.14, pp. 1151–1170. DOI: 10.1002/adma.200400719.

Li, X., Cui, X., et al. (Oct. 2014). "Analysis of positive DC corona inception voltage of stranded conductor at different altitudes". In: *2014*

IEEE Conference on Electrical Insulation and Dielectric Phenomena (CEIDP), pp. 538–541.

Li, X., Wang, J., et al. (June 2018). "Correlation between audible noise and corona current generated by AC corona discharge in time and frequency domains". In: *Physics of Plasmas* 25 (6), p. 063512. DOI: 10.1063/1.5020221.

Li, Z., Yuan, H., et al. (June 2017). "Distributed Measurement System of Ion Current Density under UHVDC Transmission Line". In: *2017 12th IEEE Conference on Industrial Electronics and Applications (ICIEA)*. IEEE, pp. 1332–1336.

Liu, H., Zhang, Q., et al. (2011). "Feasibility study of metalized membrane method applied to monitoring corona loss of AC/ DC transmission line". In: *2011 1st International Conference on Electric Power Equipment - Switching Technology*, pp. 253–257.

Liu, Y. Y., Zhou, L., et al. (Dec. 2016). "Analysis on the spectrum characteristic of corona Current and its relationship with Radio Interference on UHVDC transmission line". In: *IEEE Transactions on Dielectrics and Electrical Insulation* 23 (6), pp. 3336–3345.

Lopez Raichs, J. (2021). "Measurement Campaign on a 400 kV Outdoor Hybrid AC/DC Test Line". Semester Project. ETH Zürich.

Lu, T. et al. (May 2011). "Analysis of Corona Onset Electric Field Considering the Effect of Space Charges". In: *IEEE Transactions on Magnetics* 47 (5), pp. 1390–1393. DOI: 10.1109/TMAG.2010.2081972.

Lubachevsky, B. D. and Graham, R. L. (1995). "Dense packings of 3k (k+ 1)+ 1 equal disks in a circle for k= 1, 2, 3, 4, and 5". In: *International Computing and Combinatorics Conference*, pp. 303–312.

Lundquist, J. (Feb. 1984). "Methods for Predicting ac Transmission Line Audible Noise by Short-term Single-Pahse Tests". In: *IEEE Transactions on Power Apparatus and Systems* PAS-103 (2), pp. 283–293. DOI: 10.1109/TPAS.1984.318227.

Lundquist, J. (1990). "Results from AC transmission line audible noise studies at the Anneberg EHV test station". In: *IEEE Transactions on Power Delivery* 5 (1), pp. 317–323. DOI: 10.1109/61.107291.

Ma, M., Zhao, Y., et al. (2007). "The influence of contaminations on HVDC conductor corona characteristics". In: *2007 Annual Report*

- *Conference on Electrical Insulation and Dielectric Phenomena*, pp. 537–541. DOI: 10.1109/CEIDP.2007.4451584.

Ma, Q., Huang, K., et al. (Dec. 2017). "A MEMS-Based Electric Field Sensor for Measurement of High-Voltage DC Synthetic Fields in Air". In: *IEEE Sensors Journal* 17 (23), pp. 7866–7876. DOI: 10.1109/JSEN.2017.2762327.

Maruvada, P. S. (2000). *Corona Performance of High-Voltage Transmission Lines*. Research Studies Press Ltd.

Maruvada, P. S., Bacha, R., et al. (1979). "A Survey of Methods for Calculating Transmission Line Conductor Surface Voltage Gradients". In: *IEEE Transactions on Power Apparatus and Systems* PAS-98.6, pp. 1996–2014. DOI: 10.1109/TPAS.1979.319379.

Maruvada, P. S., Dallaire, R. D., and Pedneault, R. (1983). "Development of field-mill instruments for ground-level and above-ground electric field measurement under HVDC transmission lines". In: *IEEE Transactions on Power Apparatus and Systems* PAS-102 (3), pp. 738–744. DOI: 10.1109/TPAS.1983.318035.

Maruvada, P. S., Dallaire, R. D., and Rivest, N. (Jan. 1984). "Long-Term Statistical Study of the Corona Electric Field and Ion-Current Performance of a ±900-kV Bipolar HVDC Transmission Line Configuration". In: *IEEE Transactions on Power Apparatus and Systems* PAS-103 (1), pp. 76–83. DOI: 10.1109/TPAS.1984.318580.

Maruvada, P. S., Trinh, N. G., et al. (Nov. 1977). "Corona performance of a conductor bundle for bipolar HDVC transmission at ±750 kV". In: *IEEE Transactions on Power Apparatus and Systems* 96 (6), pp. 1872–1881. DOI: 10.1109/T-PAS.1977.32521.

Maruvada, P. S., Trinh, N. G., et al. (Mar. 1981). "Corona Studies for Biploar HVDC Transmission at Voltages Between ±600 kV and ±1200 kV Part 1: Long-Term Bipolar Line Studies". In: *IEEE Transactions on Power Apparatus and Systems* PAS-100 (3), pp. 1453–1461. DOI: 10.1109/TPAS.1981.316620.

Mather, R. and Bailey, B. (Oct. 1963). "Radio Interference from High-Voltage Lines Part II — Distribution and Correlation". In: *IEEE Transactions on Power Apparatus and Systems* 82 (68), pp. 775–782. DOI: 10.1109/TPAS.1963.291407.

Mather, R. J. and Bailey, B. M. (Apr. 1961). “Radio Interference from High-Voltage Lines Part I — Statistical Approach”. In: *Transactions of the American Institute of Electrical Engineers. Part III: Power Apparatus and Systems* 80 (3), pp. 890–894. DOI: 10.1109/AIEEPAS.1961.4501167.

Medina-Cobo, M. T. et al. (Sept. 2016). “The identification of an appropriate Minimum Inter-event Time (MIT) based on multifractal characterization of rainfall data series”. In: *Hydrological Processes* 30 (19), pp. 3507–3517. DOI: 10.1002/hyp.10875.

Meek, J. M. and Craggs, J. D. (1978). *Electrical Breakdown of Gases*. John Wiley and Sons, Ltd., New York, NY.

Meyer, S. (2021). “Smart Sensors for Monitoring the Electric Power Network”. Bachelor’s Thesis. ETH Zürich.

Mezzanotte, P. et al. (2021). “Innovative RFID sensors for Internet of Things applications”. In: *IEEE Journal of Microwaves* 1.1, pp. 55–65.

Michielsen, S. et al. (2011). “Gibbs free energy of liquid drops on conical fibers”. In: *Langmuir* 27.19, pp. 11867–11872. DOI: 10.1021/la202952e.

Morris, R. M. and Rakoshdas, B. (Jan. 1964). “An Investigation of Corona Loss and Radio Interference from Transmission Line Conductors at High Direct Voltages”. In: *IEEE Transactions on Power Apparatus and Systems* 83 (1), pp. 5–16. DOI: 10.1109/TPAS.1964.4765917.

Morris, R., Morse, A., et al. (1979). “The Corona and Radio Interference Performance of the Nelson River HVDC Transmission Lines”. In: *IEEE Transactions on Power Apparatus and Systems* PAS-98.6, pp. 1924–1936. DOI: 10.1109/TPAS.1979.319372.

Morris, R. M., Staniforth, A., and Morse, A. R. (Nov. 1971). “A Data System for High-Voltage DC Test Lines”. In: *IEEE Transactions on Instrumentation and Measurement* IM-20 (4), pp. 285–291. DOI: 10.1109/TIM.1971.5570655.

Myshkis, A. D. et al. (1987). *Low-Gravity Fluid Mechanics*. Translated. Springer-Verlag.

Nakano, Y. and Sunaga, Y. (Apr. 1989). “Availability of corona cage for predicting audible noise generated from HVDC transmission line”.

In: *IEEE Transactions on Power Delivery* 4.2, pp. 1422–1431. DOI: 10.1109/61.25629.

Neumann, C. et al. (2013). "Design and layout of AC-DC hybrid lines". In: *CIGRE Auckland Symposium*.

Newell, H. H. and Warburton, F. W. (Jan. 1956). "Variations in Radio and Television Interference from Transmission Lines". In: *Transactions of the American Institute of Electrical Engineers. Part III: Power Apparatus and Systems* 75 (3). DOI: 10.1109/AIEEPAS.1956.4499321.

Nojumuddin, N., Yusof, F., and Yusop, Z. (Feb. 2018). "Determination of minimum inter-event time for storm characterisation in Johor, Malaysia". In: *Journal of Flood Risk Management* 11, S687–S699. DOI: 10.1111/jfr3.12242.

Olsen, R., Schennum, S., and Chartier, V. (Apr. 1992). "Comparison of several methods for calculating power line electromagnetic interference levels and calibration with long term data". In: *IEEE Transactions on Power Delivery* 7 (2), pp. 903–913. DOI: 10.1109/61.127097.

Parus, N. et al. (2017). "The effect of altitude, temperature and humidity on conductor corona and audible noise under HVDC voltage stress". In: *ISH 2017*, pp. 2–6.

Paul, C. R. (2006). *Introduction to electromagnetic compatibility*. John Wiley & Sons.

Peek, F. W. (1920). *Dielectric Phenomena In High Voltage Engineering*. McGraw-Hill Book Company, Incorporated.

Perry, D. E., Chartier, V. L., and Reiner, G. L. (Sept. 1979). "BPA 1100 kV Transmission System Development Corona and Electric Field Studies". In: *IEEE Transactions on Power Apparatus and Systems* PAS-98 (5), pp. 1728–1738. DOI: 10.1109/TPAS.1979.319491.

Pfeiffer, M. (2017). "Ion-Flow Environment of HVDC and Hybrid AC/DC overhead lines". Doctoral Thesis. ETH Zürich, p. 279. DOI: 10.13039/501100001711.

Pfeiffer, M. and Franck, C. M. (Oct. 2015). "Impact of Conductor Surface Type and Rain Intensity on HVDC Corona Losses". In:

IEEE Transactions on Power Delivery 30 (5), pp. 2284–2292. DOI: 10.1109/TPWRD.2015.2424315.

Pfeiffer, M., Schultz, T., et al. (Feb. 2016). "Explaining the impact of conductor surface type on wet weather HVDC corona characteristics". In: *Journal of Electrostatics* 79, pp. 45–55. DOI: 10.1016/j.elstat.2015.12.003.

Pischler, O. and Schichler, U. (2018). "Influence of hydrophilic conductor surface treatments on OHL audible noise". In: *2018 12th International Conference on the Properties and Applications of Dielectric Materials (ICPADM)*, pp. 78–81. DOI: 10.1109/ICPADM.2018.8401081.

Pischler, O., Hedtke, S., et al. (2019). "Corona Effects of Overhead Lines under Mixed AC/DC Stresses". In: *CIGRE Symposium Chengdu*.

Prommetta, J. et al. (Oct. 2019). "AC-Protection in the Context of AC/DC-Hybrid Lines". In: *APAP 2019 - 8th IEEE International Conference on Advanced Power System Automation and Protection*, pp. 1854–1858. DOI: 10.1109/APAP47170.2019.9224645.

Rabie, M. and Franck, C. M. (May 2016). "A study of the avalanche-to-streamer transition in arbitrary gases by particle simulation". In: *Journal of Physics D: Applied Physics* 49 (17), p. 175202. DOI: 10.1088/0022-3727/49/17/175202.

Reidy, S. (2021). "Behavior of Hanging Water Droplets in Non-Uniform Electric Fields". Bachelor's Thesis. ETH Zürich.

Reznik, S. N. et al. (2004). "Transient and steady shapes of droplets attached to a surface in a strong electric field". In: *Journal of Fluid Mechanics* 516, pp. 349–377. DOI: 10.1017/S0022112004000679.

Rodriguez, J. C., Nico, V., and Punch, J. (2019). "Powering wireless sensor nodes for industrial IoT applications using vibration energy harvesting". In: *2019 IEEE 5th World Forum on Internet of Things (WF-IoT)*, pp. 392–397.

Roux, J. M. and Achard, J. L. (Sept. 2009). "Forces and charges on a slightly deformed droplet in the DC field of a plate condenser". In: *Journal of Electrostatics* 67.5, pp. 789–798. DOI: 10.1016/j.elstat.2009.06.001.

Roux, J. M., Achard, J. L., and Fouillet, Y. (May 2008). "Forces and charges on an undeformable droplet in the DC field of a plate condenser". In: *Journal of Electrostatics* 66.5-6, pp. 283–293. DOI: 10.1016/j.elstat.2008.01.008.

Sawada, Y. et al. (Nov. 1977). "The radio interference characteristics of four-and three-conductor bundles of HVDC line: Shiobara 600-kV laboratory". In: *IEEE Transactions on Power Apparatus and Systems* 96 (6), pp. 1901–1907. DOI: 10.1109/T-PAS.1977.32524.

Schlatter, I. (2020). "Artificial Corona Sources for a 400 kV Outdoor Test Line". Semester Project. ETH Zürich.

Schlecht, I. and Weigt, H. (Apr. 2015). "Linking Europe: The Role of the Swiss Electricity Transmission Grid until 2050". In: *Swiss Journal of Economics and Statistics* 151 (2), pp. 125–165. DOI: 10.1007/BF03399415.

Schultz, T., Pfeiffer, M., and Franck, C. M. (Oct. 2015). "Optical investigation methods for determining the impact of rain drops on HVDC corona". In: *Journal of Electrostatics* 77, pp. 13–20. DOI: 10.1016/j.elstat.2015.06.007.

Schutzius, T. M. et al. (Nov. 2015). "Spontaneous droplet trampolining on rigid superhydrophobic surfaces". In: *Nature* 527.7576, pp. 82–85. DOI: 10.1038/nature15738.

Shin, K. Y. et al. (Sept. 2019). "Long-term evaluation of HVDC transmission line audible noise and its correlation with background noise". In: *AIP Advances* 9 (9), p. 095014. DOI: 10.1063/1.5111434.

Singh, J., Kaur, R., and Singh, D. (2021). "Energy harvesting in wireless sensor networks: A taxonomic survey". In: *International Journal of Energy Research* 45.1, pp. 118–140.

Stadler, B. (2021). "Ground Level Ion Current Density Smart Sensor for use under HVDC Test Lines". Bachelor's Thesis. ETH Zürich.

Stamatopoulos, C., Bleuler, P., et al. (Apr. 2019). "Influence of Surface Wettability on Discharges from Water Drops in Electric Fields". In: *Langmuir* 35 (14), pp. 4876–4885. DOI: 10.1021/acs.langmuir.9b00374.

Stamatopoulos, C., Suter, R., and Franck, C. M. (Mar. 2022). "Electric Field Mediated Contact Time Reduction of Impacting Drops

on Cu(OH) ₂ Nanoneedle Clusters: Limitations and Implications for Anti-Icing and Pathogen-Containment Applications". In: *ACS Applied Nano Materials* 5 (3), pp. 3303–3311. DOI: 10.1021/acsanm.1c03820.

Steffen, B. et al. (Feb. 2020). "Experience Curves for Operations and Maintenance Costs of Renewable Energy Technologies". In: *Joule* 4 (2), pp. 359–375. DOI: 10.1016/j.joule.2019.11.012.

Straumann, U. and Fan, J. (2009). "Audible Noise from AC-UHV Transmission Lines — Theoretical Comparison of Broadband and Tonal Components". In: *International Conference on UHV Transmission, Beijing*.

Straumann, U. and Weber, H. J. (2010). "Potential reduction of audible noise from new and aged overhead transmission line conductors by increasing their hydrophilicity". In: *CIGRE Session, Paris*.

Task Force of the Corona and Field Effects Subcommittee (1982). "A Comparison of Methods for Calculating Audible Noise of High Voltage Transmission Lines". In: *IEEE Transactions on Power Apparatus and Systems* PAS-101 (10), pp. 4090–4099.

Taylor, E., Chartier, V. L., and Rice, D. (1969). "Audible Noise and Visual Corona from HV and EHV Transmission Lines and Substation Conductors - Laboratory Tests". In: *IEEE Transactions on Power Apparatus and Systems* PAS-88 (5), pp. 666–679. DOI: 10.1109/TPAS.1969.292356.

Taylor, G. (July 1964). "Disintegration of Water Drops in an Electric Field". In: *Proceedings of the Royal Society A: Mathematical, Physical and Engineering Sciences* 280.1382, pp. 383–397. DOI: 10.1098/rspa.1964.0151.

Tian, F., Yu, Z., and Zeng, R. (May 2012). "Radio Interference and Audible Noise of the UHVDC test line under high altitude condition". In: *2012 Asia-Pacific Symposium on Electromagnetic Compatibility*, pp. 449–452. DOI: 10.1109/APEMC.2012.6238006.

Townsend, J. S. E. (1915). *Electricity in Gases*. eng. Oxford: Clarendon Press.

Traipattanakul, B., Tso, C., and Chao, C. Y. (2017). "Study of jumping water droplets on superhydrophobic surfaces with electric fields".

In: *International Journal of Heat and Mass Transfer* 115, pp. 672–681. DOI: 10.1016/j.ijheatmasstransfer.2017.07.096.

Trichel, G. W. (Dec. 1938). "The Mechanism of the Negative Point to Plane Corona Near Onset". In: *Physical Review* 54 (12), pp. 1078–1084. DOI: 10.1103/PhysRev.54.1078.

Trichel, G. W. (Feb. 1939). "The Mechanism of the Positive Point-to-Plane Corona in Air at Atmospheric Pressure". In: *Physical Review* 55 (4), pp. 382–390. DOI: 10.1103/PhysRev.55.382.

Trinh, N. (May 1995). "Partial discharge XX. Partial discharges in air. II. Selection of line conductors". In: *IEEE Electrical Insulation Magazine* 11 (3), pp. 5–11. DOI: 10.1109/57.387828.

Tsimbalo, E., Fafoutis, X., and Piechocki, R. (2015). "Fix it, don't bin it! - CRC error correction in Bluetooth Low Energy". In: *IEEE World Forum on Internet of Things, WF-IoT 2015 - Proceedings*, pp. 286–290. DOI: 10.1109/WF-IOT.2015.7389067.

Tuoi, T. T. K., Van Toan, N., and Ono, T. (2022). "Self-powered wireless sensing system driven by daily ambient temperature energy harvesting". In: *Applied Energy* 311, p. 118679.

Übertragungsnetzbetreiber (2021). *Netzentwicklungsplan Strom 2035*. Tech. rep.

Ulmer, F. (2021). "Smart Sensors for Monitoring the Electric Power Network". Semester Project. ETH Zürich.

Vorwerk, J. (2018). "Effect of Electric Field on Droplets Impacting Surfaces with Different Wettabilities". Master's Thesis. ETH Zürich.

Wang, P. and Zhang, G. (Aug. 2008). "The Measurement Method for Corona Discharge Current Under High-Voltage Environment". In: *IEEE Transactions on Instrumentation and Measurement* 57 (8), pp. 1786–1790.

Wang, Q., Suo, Z., and Zhao, X. (2012). "Bursting drops in solid dielectrics caused by high voltages." In: *Nature communications* 3.May, p. 1157. DOI: 10.1038/ncomms2178.

Waskom, M. L. (2021). "seaborn: statistical data visualization". In: *Journal of Open Source Software* 6.60, p. 3021. DOI: 10.21105/joss.03021.

Wilson, C. T. R. (June 1908). “On the measurement of the atmospheric electric potential gradient and the earth-air current”. In: *Proceedings of the Royal Society of London. Series A, Containing Papers of a Mathematical and Physical Character* 80 (542), pp. 537–547. DOI: 10.1098/rspa.1908.0048.

Xiao, Y., Bleuler, P., and Franck, C. M. (in preparation). “An IoT-based Digital Osciloscope for MCCB Predictive Maintenance”. In: *IEEE Transactions on Instrumentation and Measurement*.

Xie, H. et al. (Sept. 2020). “Statistical analysis of audible noise of 1000kV UHV AC double-circuit transmission line during rain over one-year test”. In: *2020 IEEE International Conference on High Voltage Engineering and Application (ICHVE)*, pp. 1–4. DOI: 10.1109/ICHVE49031.2020.9280090.

Xu, P., Zhang, B., Chen, S., et al. (June 2016). “Influence of humidity on the characteristics of positive corona discharge in air”. In: *Physics of Plasmas* 23 (6), p. 063511. DOI: 10.1063/1.4953890.

Xu, P., Zhang, B., He, J., et al. (Sept. 2015). “Influence of humidity on the characteristics of negative corona discharge in air”. In: *Physics of Plasmas* 22 (9), p. 093514. DOI: 10.1063/1.4931744.

Xu, P., Zhang, B., Wang, Z., et al. (2017). “Dynamic corona characteristics of water droplets on charged conductor surface”. In: *Journal of Physics D: Applied Physics* 50.8, p. 085201. DOI: 10.1088/1361-6463/aa5760.

Ya, M. et al. (Mar. 2019). “Ion flow characteristic under UHVDC transmission line at high altitude”. In: *The Journal of Engineering* 2019 (16), pp. 1185–1188. DOI: 10.1049/joe.2018.8595.

Yamazaki, K. and Olsen, R. (Aug. 2004). “Application of a corona onset criterion to calculation of corona onset voltage of stranded conductors”. In: *IEEE Transactions on Dielectrics and Electrical Insulation* 11 (4), pp. 674–680. DOI: 10.1109/TDEI.2004.1324356.

Yanashima, R. et al. (Sept. 2012). “Cutting a Drop of Water Pinned by Wire Loops Using a Superhydrophobic Surface and Knife”. In: *PLoS ONE* 7.9. Ed. by A. Docoslis, e45893. DOI: 10.1371/journal.pone.0045893.

Yang, Q. et al. (May 2020). “AC/DC hybrid electric field measurement method based on Pockels effect and electric field modulation”. In: *Review of Scientific Instruments* 91 (5), p. 055004. DOI: 10.1063/1.5143767.

Yi, Y., Chen, Z. Y., and Wang, L. M. (Sept. 2017). “Surface aging effects of long-term energized conductors on spectrum characteristics of audible noise”. In: *AIP Advances* 7 (9), p. 095020.

Yu, Z. et al. (Mar. 2019). “Long-term statistics of corona loss of HVDC transmission line”. In: *The Journal of Engineering* 2019 (16), pp. 3169–3174. DOI: 10.1049/joe.2018.8417.

Yuan, H. et al. (Apr. 2012). “Development and Application of High-Frequency Sensor for Corona Current Measurement under Ultra High-Voltage Direct-Current Environment”. In: *IEEE Transactions on Instrumentation and Measurement* 61 (4), pp. 1064–1071.

Zeleny, J. (1917). “Instability of electrified liquid surfaces”. In: *Physical Review* 10.

Zhang, B. et al. (Apr. 2013). “Analysis of Ion Flow Field of UHV / EHV AC Transmission Lines”. In: *IEEE Transactions on Dielectrics and Electrical Insulation* 20 (2), pp. 496–504. DOI: 10.1109/TDEI.2013.6508752.

Zhao, L. et al. (Aug. 2017). “The Altitude Effect and Correction of Audible Noise for HVdc Transmission Lines”. In: *IEEE Transactions on Power Delivery* 32 (4), pp. 1954–1963. DOI: 10.1109/TPWRD.2016.2601642.

Zhou, P.-b. (1993). *Numerical Analysis of Electromagnetic Fields*. Springer Berlin Heidelberg. DOI: 10.1007/978-3-642-50319-1.

Zhou, X. et al. (July 2012). “Simulation of Ion-Flow Field Using Fully Coupled Upwind Finite-Element Method”. In: *IEEE Transactions on Power Delivery* 27 (3), pp. 1574–1582. DOI: 10.1109/TPWRD.2012.2197226.

Curriculum Vitæ

Pascal Toma BLEULER

born	on 20 December 1991 in Tokyo, Japan
citizenship	Swiss and Japanese
place of origin	Zollikon, ZH

Languages spoken

French	native speaker
Swiss German	father tongue
Japanese	mother tongue
German	full professional proficiency
English	full professional proficiency

Education

2017 – 2022	**ETH Zürich** Doctor of Sciences
2010 – 2016	**EPFL** Bachelor of Science and Master of Science in Electrical and Electronic Engineering Master project at the **University of Bologna**

Work experience and extra-curricular activities

2023 – ongoing	**ABB Traction**, System engineer
2016 – 2022	**High Voltage Laboratory** **ETH Zürich**, Scientific assistant
2016	**Power Electronics Laboratory** **EPFL**, Trainee
2015	**Duagon**, Internship
2020 – 2022	**University Assembly** (ETH Zürich), Vice-president (2022), committee member (2020 – 2021)
2012 – 2016	**Satellite** (EPFL), Vice-president (2013 – 2014), graphic designer (2014 – 2016) and other roles
Other activities	• Stage manager and lighting designer at various international music festivals (2014 – 2022) • Teaching assistant in physics and electrical engineering at EPFL and ETH Zürich (2012 – 2022) • Class representative at EPFL and Gymnase de Morges (2007 – 2015) • *Diversity+Inclusion* group at the Department Association, ETH Zürich (2019) • Film Critic for the *TRIBUne des Jeunes Cinéphiles* (2007 – 2010) • Member of the School Choir at Gymnase de Morges (2007 – 2014)

Invited speaker

2020, Online	A New Perspective on Teaching Video Educational Development and Technology ETH Zürich
2022, Hamburg	Forum Netzbau und Netzbetrieb Leitungsbautagung MVV Regioplan GmbH